Scholars' Mine

Fall 2018

Direct numerical simulation of pressure fluctuations induced by supersonic turbulent boundary layers

Chao Zhang

Follow this and additional works at: https://scholarsmine.mst.edu/doctoral_dissertations

Part of the Aerospace Engineering Commons

Department: Mechanical and Aerospace Engineering

Recommended Citation

DIRECT NUMERICAL SIMULATION OF PRESSURE FLUCTUATIONS INDUCED

BY SUPERSONIC TURBULENT BOUNDARY LAYERS

by

CHAO ZHANG

A DISSERTATION

Presented to the Graduate Faculty of the

MISSOURI UNIVERSITY OF SCIENCE AND TECHNOLOGY

In Partial Fulfillment of the Requirements for the Degree

DOCTOR OF PHILOSOPHY

in

AEROSPACE ENGINEERING

2018

Approved by

Dr. Lian Duan, Advisor
Dr. Kakkattukuzhy M. Isaac
Dr. David Riggins
Dr. Serhat Hosder
Dr. Xiaoming He

PUBLICATION DISSERTATION OPTION

This dissertation consists of the following three articles which have been published as follows:

Paper I: Pages 10-56 have been published in Journal of Fluid Mechanics.

Paper II: Pages 57-95 have been published in Journal of Fluid Mechanics.

Paper III: Pages 96-134 have been published in AIAA Journal.

ABSTRACT

Direct Numerical Simulations are used to generate a database of high-speed zero-pressure-gradient turbulent boundary layers developing spatially over a flat plate with nominal freestream Mach number ranging from 2.5 to 14 and wall-to-recovery temperature ranging from 0.18 to 1.0. The flow conditions of the DNS are representative of the operational conditions of the Purdue Mach 6 quiet tunnel, the Sandia Hypersonic Wind Tunnel at Mach 8, and the AEDC Hypervelocity Tunnel No. 9 at Mach 14. The DNS database is used to gauge the performance of compressibility transformations, including the classical Morkovin's scaling and strong Reynolds analogy as well as the newly proposed mean velocity and temperature scalings that explicitly account for wall heat flux, examine the pressure fluctuations generated by the turbulent boundary layers. The unsteady pressure field is analyzed at multiple wall-normal locations, including those at the wall, within the boundary layer (including inner layer, the log layer, and the outer), and in the free stream. The statistical and structural variations of pressure fluctuations as a function of wall-normal distance are highlighted. The simulations show that the dominant frequency of boundary-layer-induced pressure fluctuations shifts to lower frequencies as the location of interest moves away from the wall. The pressure structures within the boundary layer and in the free stream evolve less rapidly as the wall temperature decreases, resulting in an increase in the decorrelation length of coherent pressure structures for the colder wall case. The pressure structures propagate with similar speeds for both wall temperatures. Acoustic sources are largely concentrated in the near-wall region; wall cooling most significantly influences the nonlinear (slow) component of the acoustic source term by enhancing dilatational fluctuations in the viscous sublayer while damping vortical fluctuations in the buffer and log layers. Precomputed flow statistics, including Reynolds stresses and their budgets, are available at the website of the NASA Langley Turbulence Modeling Resource.

ACKNOWLEDGMENTS

First and foremost, I would like to express my sincere gratitude to my advisor, Dr. Lian Duan, for his encouragement, insightful guidance, and support during my Ph.D. study at Missouri University of Science and Technology. His diligence and rigorous attitude to research and work will have a significant influence on my life. It has been a privilege and a great honor to have worked with him.

I would also like to extend my appreciation to all my dissertation committee members, Dr. Kakkattukuzhy M. Isaac, Dr. David Riggins, Dr. Serhat Hosder, and Dr. Xiaoming He, and our collaborator, Dr. Meelan Choudhari, at NASA Langley Research Center. Without their guidance and valuable comments it would have been impossible for me to complete my dissertation.

I would like to express my deep thanks to my lab-mates and friends, Mr. Junji Huang, Mr. Yuchen Liu, Mr. Gary Nicholson, for their support during my study in Rolla.

Lastly, and most certainly not least, I express my appreciation and sincere thanks to my parents, brother, and sister-in-law, for their everlasting love and support.

TABLE OF CONTENTS

LIST OF ILLUSTRATIONS

LIST OF TABLES

SECTION

1. INTRODUCTION

1.1. BACKGROUND

Despite being a canonical flow, the flat plate turbulent boundary layer remains the subject of interest. An essential part of the study of compressible turbulent boundary layers is to check the validity of Morkovin's hypothesis, which postulates that high speed turbulence structure in zero pressure-gradient turbulent boundary layers remains largely the same as its incompressible counterpart (Smits and Dussauge, 2006a). An important consequence of Morkovin's hypothesis is the so-called 'compressibility transformations' that transform the mean velocity and Reynolds stress profiles in a compressible boundary layer to equivalent incompressible profiles by accounting for mean property variations across the thickness of the boundary layer. A classical example of such transformations is the density-weighted velocity scaling of Van Driest van Driest (1956). Another consequence of Morkovin's hypothesis is the analogy between the temperature and velocity fields that leads to velocity-temperature relations such as the classical Walz formula (Walz, 1969) and the strong Reynolds numbers analogy (SRA) (Gaviglio, 1987; Huang *et al.*, 1995; Morkovin, 1962). In addition to the classical Van Driest transformation and the SRA, which have been verified largely for supersonic turbulent boundary layers ($M_\infty < 5$) with an adiabatic wall, new mean velocity and velocity-temperature scaling relations have recently been proposed to explicitly account for a finite wall heat flux (Patel *et al.*, 2016; Trettel and Larsson, 2016; Zhang *et al.*, 2014). For example, Patel *et al.* (2015) proposed a semilocal Reynolds number Re_τ^* for comparing wall turbulence statistics among cases with substantially different mean density and viscosity profiles. Trettel and Larsson (2016) recently provided an exten-

sion to the Van Driest transformation for compressible wall turbulence with heat transfer by deriving a novel velocity transformation based on arguments about log-layer scaling and near-wall momentum conservation. Zhang *et al.* (2014) generalized the temperature-velocity relation of Walz and Huang's SRA to explicitly account for a finite wall heat flux. These new scaling relations have been shown to yield much improved collapse of the supersonic data to the incompressible case when there is a strong heat transfer at the surface (Modesti and Pirozzoli, 2016a). The success of the compressibility transformations and the SRA may suggest that there exist few, if any, dynamic differences due to Mach number, as postulated by Morkovin, at least for wall turbulence at moderate Mach numbers ($M_\infty < 5$).

At hypersonic speeds ($M_\infty > 5$), the validity of Morkovin's hypothesis may come into question because of the increasing density and pressure fluctuations at high Mach numbers. Turbulent fluctuations can even become locally supersonic relative to the surrounding flow, creating the so-called eddy shocklets that could significantly modify the dynamics of the flow. However, the Mach number at which Morkovin's hypothesis would lose significant accuracy remains largely undetermined. There are still limited measurements at hypersonic speeds that are detailed and accurate enough for testing the validity of Morkovin's hypothesis. Experimental investigations of hypersonic turbulent boundary layers have been conducted historically with hot-wire anemometry (see, for example, the review by Roy and Blottner (2006)). A recent investigation by Williams *et al.* (2018) showed that much of the historical hot-wire measurements of turbulence statistics suffered from poor frequency response and/or spatial resolution. Hot-wire anemometry may also suffer from uncertainties associated with the mixed-mode sensitivity of the hot wires, given that the hot wire measures a combination of the fluctuating mass flux and the fluctuating total temperature (Kovasznay, 1953). In addition to hot-wire anemometry, direct measurements of spatially varying velocity fields of high-speed turbulent boundary layers have been attempted using Particle Image Velocimetry (PIV) Ekoto *et al.* (2008); Peltier *et al.* (2016a);

Tichenor *et al.* (2013); Williams *et al.* (2018). Among the existing PIV measurements, the measurement by Williams et al. Williams *et al.* (2018) in a Mach 7.5 flat-plate turbulent boundary layer is the only PIV measurement conducted at a Mach number above five. Although the existing PIV results provided direct experimental evidence for the validity of Morkovin scaling for the streamwise velocity at Mach numbers as high as 7.5, accurate measurements were not yet acquired for the wall-normal component of the velocity or the Reynolds stress. The existing PIV data exhibited reduced levels of the wall-normal component of the velocity in comparison with the predictions based on the Morkovin scaling, and the deviation became larger with increasing Mach number. As noticed by Williams *et al.* (2018), the loss in accuracy is largely due to particle response limitations that result in significantly reduced levels of wall-normal velocity fluctuations.

Complementary to experiments, direct numerical simulations (DNS) of high-speed turbulent boundary layers have been conducted to overcome the experimental difficulties and provide access to three-dimensional turbulence statistics. Although several DNS have been conducted for studying Morkovin's scaling in turbulent boundary layers with moderate freestream Mach number ($M < 5$) (Hadjadj *et al.*, 2015; Maeder, 2000; Modesti and Pirozzoli, 2016a; Pirozzoli and Bernardini, 2011; Poggie, 2015; Shahab *et al.*, 2011; Trettel and Larsson, 2016; Zhang *et al.*, 2014), there is little DNS data for turbulent boundary layers in the high Mach number regime (Roy and Blottner, 2006). Martin (2004); Martín (2007) made a pioneering effort toward characterizing boundary-layer turbulence in the hypersonic regime by developing a temporal DNS database of canonical zero-pressure-gradient, flat-plate turbulent boundary layers up to Mach 8 with varying wall temperatures. (Duan *et al.*, 2010, 2011; Duan and Martín, 2011) extended the datasets of Martin (2004) to even higher Mach numbers (up to Mach 12) with cold wall and high enthalpy and conducted a systematic study of wall turbulence and its dependence on freestream Mach number, wall cooling, and high enthalpy. Additional DNS studies of hypersonic turbulent boundary layers in the literature include that by Lagha et al. (Lagha *et al.*, 2011) up to Mach 20 with an

adiabatic wall ($T_w/T_r = 1.0$) and that by Priebe and Martín at Mach 7.2 (Priebe and Martín, June 2011) with $T_w/T_r = 0.53$. Except for the work by Duan et al. (Duan *et al.*, 2010), who systematically studied the effect of wall cooling on boundary-layer turbulence at Mach 5, most of the previous DNS at high Mach number simulated a turbulent boundary layer over a hypothetically adiabatic wall. The new scaling relations of Refs. (Patel *et al.*, 2016; Trettel and Larsson, 2016; Zhang *et al.*, 2014) that explicitly account for finite wall heat flux have not yet been systematically assessed under high Mach number, cold-wall conditions.

The knowledge of turbulent boundary layers at high Mach numbers is important to the design of high speed vehicles, as turbulent boundary layers determine the aerodynamic drag and heat transfer. So understanding the physics of the pressure fluctuations induced by high-speed turbulent boundary layers is of major theoretical and practical importance. From a practical point of view, the fluctuating pressure on aerodynamic surfaces of flight vehicles plays an important role in vibrational loading and often leads to damaging effects as fatigue and flutter (Blake, 1986; Bull, 1996; Willmarth, 1975). The freestream pressure fluctuations radiated from the turbulent boundary layer on the nozzle wall in a conventional hypersonic wind tunnel are largely responsible for the genesis of tunnel background disturbances (commonly referred to as tunnel noise) (Laufer, 1964; Pate, 1978; Stainback, 1971). Such facility disturbances significantly impact the laminar-turbulent transition behavior of the test article, leading to an earlier onset of transition relative to that in a flight environment or in a quiet tunnel (Schneider, 2001). Given that the surface temperatures of hypersonic flight vehicles are typically significantly lower than the adiabatic wall temperature and that practical hypersonic facilities for testing and evaluating hypersonic vehicles are designed to have a non-adiabatic turbulent boundary layer on the nozzle wall, it is of practical importance to investigate wall-temperature effects on hypersonic turbulent boundary layers and their induced pressure fluctuations. An in-depth knowledge of the nature of pressure fluctuations in the high-speed regime is essential to the structural design of launch vehicles and to enabling a better use of transition data from the noisy hypersonic facili-

ties. From a theoretical point of view, a better understanding of the pressure fluctuations could lead to a better understanding of the vorticity dynamics in the boundary layer since high-vorticity regions are strongly correlated with low-pressure regions (Cadot *et al.*, 1995; Kida and Miura, 1998; Kim, 1989). Moreover, pressure fluctuations are an important ingredient in turbulence as they appear in statistical correlations such as the pressure-strain correlation terms which redistribute turbulence among different components of fluctuating velocity. The modeling of the pressure-strain terms in the transport equations for the Reynolds stresses and the dissipation tensor is regarded as one of the major issues in the Reynolds stress closure.

A considerable amount of work has been devoted to the understanding of the boundary layer induced pressure fluctuations. The analysis of the pressure fluctuations in the context of incompressible boundary layers is based on the Poisson equation. The source term in the Poisson equation is composed of two parts that generate, respectively, what are commonly referred to as the rapid (linear) and slow (nonlinear) parts of the pressure fluctuation field. Examples of existing studies of the global pressure field induced by incompressible boundary layers include those by Kat and Oudheusden (2012); Kim (1989); Tsuji *et al.* (2007, 2012) and Naka *et al.* (2015) among many others. The pressure fluctuations induced by a high-speed turbulent boundary layer are, however, fundamentally more complicated than their low-speed counterparts. At high speeds, pressure fluctuations of the acoustic mode emerge in the form of eddy Mach waves. The pressure fluctuations in a turbulent boundary layer thus include contributions from both vorticity and acoustic modes. The former component is typically dominant within the boundary layer while the latter is dominant in the free stream. The relative importance of the two modes in different regions of the boundary layer at high speeds is largely unknown and a detailed analysis of the turbulent correlations containing pressure fluctuations is lacking. Although there is a significant amount of literature on the behavior, distribution, and scaling of velocity fluctuations in high-speed turbulent boundary layers (Smits and Dussauge, 2006b), the corresponding be-

havior of pressure fluctuations is much less known. No measurement technique so far has been able to globally measure the pressure fluctuations inside the boundary layer. Thus existing measurements of pressure fluctuations due to high-speed turbulent boundary layers consist largely of those at the surface using surface-mounted pressure transducers. The few existing measurements of fluctuating wall pressure signals beneath supersonic turbulent boundary layers include early measurements by Kistler and Chen (1963) and by Maestrello (1969) for boundary layers with freestream Mach number M_∞ ranging from 1.33 to 5, and more recently by Beresh *et al.* (2011) for boundary layers with M_∞ up to 3. These measurements exhibit a considerable degree of scatter. For example, the measurements by Kistler and Chen (1963) and by Maestrello (1969) found discrepancies in the magnitude of wall pressure fluctuations as large as 30%. The recent data acquired by Beresh *et al.* (2011) showed similar large scatter across a broad compilation of high-speed measurements. As pointed out by several authors (Beresh *et al.*, 2011; Dolling and Dussauge, 1989), there are few (if any) reliable measurements of the variance of the wall pressure fluctuations and its frequency spectra, due to the poor spatial resolution of pressure transducers or limitations in the frequency response of pressure sensors. Previous DNS studies of pressure fluctuations induced by high-speed boundary layers focused on the wall pressure and were limited to moderate freestream Mach numbers (up to Mach 4) (Bernardini and Pirozzoli, 2011; Marco *et al.*, 2013). To the knowledge of the authors, no data exist for turbulent boundary layers in the hypersonic regime that provide global access to the fluctuating pressure field.

As far as the freestream acoustic pressure fluctuations are concerned, the body of available data is even more scarce. Although a number of investigators have reported measurements of freestream disturbance intensity in high-speed facilities at both supersonic and hypersonic Mach numbers (Bounitch *et al.*, 2011; Donaldson and Coulter, 1995; Masutti *et al.*, 2012), the measurements by Laufer (1964) still provide one of the few datasets that are detailed enough to be suitable for comparison or model development. Similar to the wall-pressure measurements, Laufer's measurements of the acoustic fluctuations in the

freestream region (Laufer, 1964) are subject to analogous sources of experimental error. Moreover, as noted by Laufer, the interpretation of disturbance measurements in a wind tunnel is further complicated by the fact that the measurements reflect the combined outcome of acoustic radiation from all sides of the tunnel wall. As a result, highly accurate measurements of the absolute amplitudes of the radiated acoustic energy were not pursued during his experiments and only the statistical quantities that were least likely to be influenced by the presence of multiple tunnel walls were investigated.

1.2. OBJECTIVES

Motivated by characterizing freestream acoustic disturbances in conventional (i.e., 'noisy') high-speed wind tunnels, the main objective of this dissertation is to conduct Direct Numerical Simulations to investigate the global pressure field and its dependence on boundary-layer parameters (e.g., freestream Mach number, wall temperature, and Reynolds number). Direct Numerical Simulation is a valuable tool that can overcome some of the aforementioned difficulties with both experimental measurements and theory and, hence, provide access to both flow and acoustic quantities that are difficult to obtain otherwise. The DNS can also isolate the acoustic radiation due to individual physical mechanisms, thereby avoiding any contamination due to secondary sources such as vortial and entropy fluctuations in the incoming stream.

In this dissertation, we developed a new DNS database of spatially developing, flat-plate turbulent boundary layers that was developed using a large computational domain with low-dissipative spatial discretization, and that covers a wide range of freestream Mach number ($M_\infty = 2.5 - 14$) and wall-to-recovery temperature ratio ($T_w/T_r = 0.18 - 1.0$). Unlike the temporal DNS of Martín (Martin, 2004) and Duan et al. (Duan *et al.*, 2010, 2011) that used a small streamwise domain ($\approx 8\delta$) with a periodic boundary condition in the streamwise direction, these DNS simulate spatially developing turbulent boundary layers with a long streamwise domain length ($> 50\delta_i$) to minimize any artificial effects of inflow

turbulence generation and to guarantee the convergence of high-order turbulence statistics. Moreover, the new DNS database mimics realistic flow conditions such as those in hypersonic wind tunnel facilities with a cooled wall rather than simulating hypersonic turbulent boundary layers over a hypothetically adiabatic wall (Duan *et al.*, 2011; Lagha *et al.*, 2011; Martín, 2007). The combination of high freestream Mach number (with nominal freestream Mach number as high as $M_\infty = 14$) and cold wall temperature (with wall-to-recovery temperature as low as $T_w/T_r = 0.18$) covered in the database extends the available database to more extreme, yet practical, cases that serve as a reference for modeling wall-bounded turbulence in the high-Mach-number, cold-wall regime as well as for developing novel compressibility transformations that collapse compressible boundary-layer profiles to incompressible results (Duan *et al.*, 2016; Zhang *et al.*, 2015; Zhang and Duan, 2016; Zhang *et al.*, 2017, 2018, Jan. 2016). For that purpose, both statistical quantities and subsets of raw flow samples are made publicly available on a web site, which will allow other investigators to access any property of interest.

1.3. ORGANIZATION OF DISSERTATION

In this dissertation, three journal papers are presented. Paper I (Duan *et al.*, 2016) conducts direct numerical simulation of a zero-pressure-gradient turbulent boundary layer with a nominal freestream Mach number of 5.86 and a wall-to-recovery temperature ratio of $T_w/T_r = 0.76$ to investigate the wall-normal variation of the fluctuating pressure field and highlight the differences between the primarily vortical pressure signal within the boundary layer and the acoustic pressure signal in the free stream. Paper II (Zhang *et al.*, 2017) conducts direct numerical simulations of Mach 5.86 turbulent boundary layers with two wall temperatures (T_w/T_r=0.25, 0.76) to investigate the effect of wall cooling on the pressure fluctuations generated by hypersonic turbulent boundary layers. Paper III (Zhang *et al.*, 2018) presents a direct numerical simulation database of high-speed zero-pressure-gradient

turbulent boundary layers developing spatially over a flat plate with nominal freestream Mach number ranging from 2.5 to 14 and wall-to-recovery temperature ratio ranging from 0.18 to 1.0.

PAPER

I. PRESSURE FLUCTUATIONS INDUCED BY A HYPERSONIC TURBULENT BOUNDARY LAYER

LIAN DUAN[1], MEELAN M. CHOUDHARI[2] and CHAO ZHANG[1]

[1]Missouri University of Science and Technology, Rolla, MO 65401, USA

[2]NASA Langley Research Center, Hampton, VA 23681, USA

ABSTRACT

Direct numerical simulations (DNS) are used to examine the pressure fluctuations generated by a spatially-developed Mach 5.86 turbulent boundary layer. The unsteady pressure field is analyzed at multiple wall-normal locations, including those at the wall, within the boundary layer (including inner layer, the log layer, and the outer layer), and in the free stream. The statistical and structural variations of pressure fluctuations as a function of wall-normal distance are highlighted. Computational predictions for mean velocity profiles and surface pressure spectrum are in good agreement with experimental measurements, providing a first ever comparison of this type at hypersonic Mach numbers. The simulation shows that the dominant frequency of boundary-layer-induced pressure fluctuations shifts to lower frequencies as the location of interest moves away from the wall. The pressure wave propagates with a speed nearly equal to the local mean velocity within the boundary layer (except in the immediate vicinity of the wall) while the propagation speed deviates from Taylor's hypothesis in the free stream. Compared with the surface pressure fluctuations, which are primarily vortical, the acoustic pressure fluctuations in the free stream exhibit a significantly lower dominant frequency, a greater spatial extent, and a

smaller bulk propagation speed. The free-stream pressure structures are found to have similar Lagrangian time and spatial scales as the acoustic sources near the wall. As the Mach number increases, the free-stream acoustic fluctuations exhibit increased radiation intensity, enhanced energy content at high frequencies, shallower orientation of wave fronts with respect to the flow direction, and larger propagation velocity.

Keywords: high-speed flow, turbulence simulation, turbulent boundary layers

1. INTRODUCTION

Understanding the physics of the pressure fluctuations induced by high-speed turbulent boundary layers is of major theoretical and practical importance. From a practical point of view, the fluctuating pressure on aerodynamic surfaces of flight vehicles plays an important role in vibrational loading and often leads to damaging effects as fatigue and flutter (Blake, 1986; Bull, 1996; Willmarth, 1975). The free-stream pressure fluctuations radiated from the turbulent boundary layer on the nozzle wall in a conventional hypersonic wind tunnel are largely responsible for the genesis of tunnel background disturbances (commonly referred to as tunnel noise) (Laufer, 1964; Pate, 1978; Stainback, 1971). Such facility disturbances significantly impact the laminar-turbulent transition behavior of the test article, leading to an earlier onset of transition relative to that in a flight environment or in a quiet tunnel (Schneider, 2001). An in-depth knowledge of the nature of pressure fluctuations in the high-speed regime is essential to the structural design of launch vehicles and to enabling a better use of transition data from the noisy hypersonic facilities. From a theoretical point of view, a better understanding of the pressure fluctuations could lead to a better understanding of the vorticity dynamics in the boundary layer since high-vorticity regions are strongly correlated with low-pressure regions (Cadot *et al.*, 1995; Kida and Miura, 1998; Kim, 1989). Moreover, pressure fluctuations are an important ingredient in turbulence as they appear in statistical correlations such as the pressure-strain correlation terms which redistribute turbulence among different components of fluctuating veloc-

ity. The modeling of the pressure-strain terms in the transport equations for the Reynolds stresses and the dissipation tensor is regarded as one of the major issues in the Reynolds stress closure.

The analysis of the pressure fluctuations in the context of incompressible boundary layers is based on the Poisson equation. The source term in the Poisson equation is composed of two parts that generate, respectively, what are commonly referred to as the rapid (linear) and slow (nonlinear) parts of the pressure fluctuation field. Examples of existing studies of the global pressure field induced by incompressible boundary layers include those by Kat and Oudheusden (2012); Kim (1989); Tsuji *et al.* (2007, 2012) and Naka *et al.* (2015) among many others. The pressure fluctuations induced by a high-speed turbulent boundary layer are, however, fundamentally more complicated than their low-speed counterparts. At high speeds, pressure fluctuations of the acoustic mode emerge in the form of eddy Mach waves. The pressure fluctuations in a turbulent boundary layer thus include contributions from both vorticity and acoustic modes. The former component is typically dominant within the boundary layer while the latter is dominant in the free stream. The relative importance of the two modes in different regions of the boundary layer at high speeds is largely unknown and a detailed analysis of the turbulent correlations containing pressure fluctuations is lacking.

Although there is a significant amount of literature on the behavior, distribution, and scaling of velocity fluctuations in high-speed turbulent boundary layers (Smits and Dussauge, 2006), the corresponding behavior of pressure fluctuations is much less known. No measurement technique so far has been able to globally measure the pressure fluctuations inside the boundary layer. Thus existing measurements of pressure fluctuations due to high-speed turbulent boundary layers consist largely of those at the surface using surface-mounted pressure transducers. The few existing measurements of fluctuating wall pressure signals beneath supersonic turbulent boundary layers include early measurements by Kistler and Chen (1963) and by Maestrello (1969) for boundary layers with free-stream

Mach number M_∞ ranging from 1.33 to 5, and more recently by Beresh *et al.* (2011) for boundary layers with M_∞ up to 3. These measurements exhibit a considerable degree of scatter. For example, the measurements by Kistler and Chen (1963) and by Maestrello (1969) found discrepancies in the magnitude of wall pressure fluctuations as large as 30%. The recent data acquired by Beresh *et al.* (2011) showed similar large scatter across a broad compilation of high-speed measurements. As pointed out by several authors (Beresh *et al.*, 2011; Dolling and Dussauge, 1989), there are few (if any) reliable measurements of the variance of the wall pressure fluctuations and its frequency spectra, due to the poor spatial resolution of pressure transducers or limitations in the frequency response of pressure sensors. Previous DNS studies of pressure fluctuations induced by high-speed boundary layers focused on the wall pressure and were limited to moderate free-stream Mach numbers (up to Mach 4) (Bernardini and Pirozzoli, 2011; Marco *et al.*, 2013). To the knowledge of the authors, no data exist for turbulent boundary layers in the hypersonic regime that provide global access to the fluctuating pressure field.

As far as the free-stream acoustic pressure fluctuations are concerned, the body of available data is even more scarce. Although a number of investigators have reported measurements of free-stream disturbance intensity in high-speed facilities at both supersonic and hypersonic Mach numbers (Bounitch *et al.*, 2011; Donaldson and Coulter, 1995; Masutti *et al.*, 2012), the measurements by Laufer (1964) still provide one of the few datasets that are detailed enough to be suitable for comparison or model development. Similar to the wall-pressure measurements, Laufer's measurements of the acoustic fluctuations in the free-stream region (Laufer, 1964) are subject to analogous sources of experimental error. Moreover, as noted by Laufer, the interpretation of disturbance measurements in a wind tunnel is further complicated by the fact that the measurements reflect the combined outcome of acoustic radiation from all sides of the tunnel wall. As a result, highly accurate

measurements of the absolute amplitudes of the radiated acoustic energy were not pursued during his experiments and only the statistical quantities that were least likely to be influenced by the presence of multiple tunnel walls were investigated.

Direct numerical simulation (DNS) is a valuable tool that can overcome some of the aforementioned difficulties with experimental measurements and, hence, provide access to the global fluctuating pressure field that is difficult to obtain otherwise. For the study of the free-stream pressure field, in particular, DNS has the additional benefit of easily isolating the acoustic radiation from a single surface as against the typical case of multiple tunnel walls in an experiment. Successful applications of DNS for studying acoustic radiation from turbulent boundary layers at subsonic and supersonic Mach numbers have been reported by Gloerfelt and Berland (2013) (Mach 0.5) and by Duan *et al.* (2014) (Mach 2.5), respectively.

The objective of the current paper is to document the statistical and structural variation of boundary-layer-induced pressure fluctuations as a function of wall-normal distance. The database to be used is obtained from a direct numerical simulation of a spatially-developing, flat-plate, nominally Mach 6 turbulent boundary layer, with the free-stream and wall-temperature conditions representative of those at the nozzle exit of the Purdue Mach 6 Quiet Tunnel under noisy operations (Schneider, 2008; Steen, 2010). The physical realism and accuracy of the computed flow fields are first established by comparing with existing experimental results. Given that the DNS grids are designed to adequately capture both the the boundary layer and the near field of acoustic fluctuations radiated by the boundary layer, the present study is the first attempt, as far as we know, to investigate the detailed pressure statistics induced by a hypersonic turbulent boundary layer that includes the radiated pressure fluctuations in the near field, in addition to those generated within the boundary layer. To our knowledge, except the study by Duan *et al.* (2014), all previous DNS studies of supersonic turbulent boundary layers have focused exclusively on flow fea-

Table 1. Freestream conditions for Mach 6 DNS of turbulent boundary layers.

M_∞	U_∞(m/s)	ρ_∞(kg/m^3)	T_∞(K)
5.86	870.4	0.0427	54.97

tures within the boundary layer. The characteristics associated with the primarily vortical pressure signal within the boundary layer and the acoustic pressure signal in the free stream are compared.

The remaining part of this paper is structured as follows. The flow conditions selected for numerical simulation and the numerical method used are outlined in Section 2. Section 3 is focused on the analysis of statistical and structural variations of pressure fluctuations as a function of wall-normal distance. The various statistics examined include pressure fluctuation intensities, power spectral densities, two-point pressure correlations, and propagation speeds. Section 4 discusses the characteristics of free-stream acoustic radiation, including modal analysis, wave-front orientation, and acoustic sources contributing to the acoustic radiation in the free stream. Conclusions from the study are presented in Section 5.

2. SIMULATION DETAILS

Table 1 outlines the free-stream flow condition for the present simulations including the free-stream Mach number M_∞, density ρ_∞ and temperature T_∞. The mean surface temperature T_w is assumed to be equal to $T_w/T_r = 0.76$, with the recovery temperature T_r estimated based on a recovery factor of 0.89. Throughout this paper, subscripts ∞ and w will be used to denote quantities at the boundary layer edge and at the wall, respectively. The free-stream condition is selected to be similar to the conditions of the Boeing/AFOSR

Mach-6 Quiet Tunnel (Schneider, 2001; Steen, 2010) (BAM6QT) under noisy operations, so that one-to-one comparison between DNS and experimental results can be conducted to establish the physical realism and accuracy of the computed flow fields.

2.1. GOVERNING EQUATIONS AND NUMERICAL METHODS

The details of the DNS methodology, including numerical methods, initial and boundary conditions, have been documented in our previous paper (Duan *et al.*, 2014). Therefore, only a cursory description is given here.

The full three-dimensional compressible Navier-Stokes equations in conservation form are solved in generalized curvilinear coordinates. The working fluid is assumed to be a perfect gas and the usual constitutive relations for a Newtonian fluid are used: the viscous stress tensor is linearly related to the rate-of-strain tensor, and the heat flux vector is linearly related to the temperature gradient through Fourier's law. The coefficient of viscosity μ is computed from Sutherlands's law, and the coefficient of thermal conductivity κ is computed from $\kappa = \mu C_p / Pr$, with the molecular Prandtl number $Pr = 0.71$ and C_p the heat capacity at constant pressure.

A seventh-order weighted essentially non-oscillatory (WENO) scheme is used to compute the convective flux terms. Compared with the original finite-difference WENO introduced by Jiang and Shu (1996), the present WENO scheme is optimized by means of limiters (Taylor *et al.*, 2006; Wu and Martín, 2007) to reduce the numerical dissipation. For the viscous flux terms, a fourth-order central difference scheme is used. The third-order low-storage Runge-Kutta scheme by Williamson (1980) is used for time integration.

The DNS code has been extensively validated in previous work for simulating supersonic and hypersonic turbulent boundary layers (Duan *et al.*, 2010, 2011; Duan and Martín, 2011; Martín, 2007; Priebe and Martín, 2012; Wu and Martín, 2007, 2008). The optimized WENO has been shown to be adequate for time-accurate simulations of compressible turbulence (Duan *et al.*, 2010, 2011; Duan and Martín, 2011; Martín, 2007; Priebe

and Martín, 2012; Wu and Martín, 2007, 2008). The shock-capturing capability of the algorithm guarantees numerical stability and robustness under the present high-Mach-number condition.

2.2. COMPUTATIONAL DOMAIN AND SIMULATION SETUP

Figure 1 shows a general computational set-up for the DNS in the present work, which parallels the setup in Duan *et al.* (2014) for the Mach 2.5 simulation, wherein the effects of domain size and grid resolution were also assessed. The reference length δ_i is the thickness of the boundary layer (based on 99% of the free-stream velocity) at the inlet plane. An instantaneous flow is shown in the domain, visualized by iso-surface of the magnitude of density gradient, $|\nabla\rho|\delta_i/\rho_\infty = 0.9825$, colored by the streamwise velocity component (with levels from 0 to U_∞, blue to red). x, y, and z are, respectively, the streamwise, spanwise, and wall-normal coordinates. The choice of grid parameters for the present study is based on lessons learned from Duan *et al.* (2014) as summarized in Table 2. L_x, L_y, and L_z are the domain size in the streamwise, spanwise, and wall-normal directions, respectively. Δx^+ and Δy^+ are the uniform grid spacing in the streamwise and spanwise directions, respectively. Δz^+_{min} and Δz^+_{max} are the minimum and maximum wall-normal grid spacing for $0 \leq z/\delta_i \leq 5.5$. The grid spacings are reported in terms of the viscous length scale z_τ evaluated at the station selected for statistical analysis $x_a/\delta_i = 54.1$. $\delta_i = 13.8$ mm. The streamwise domain length (L_x) is selected to be larger than the eddy decorrelation distance to guarantee minimal spurious correlation being introduced due to the inflow turbulence generation. The spanwise domain (L_y) is chosen based on monitoring the decay in cross-correlation of pressure fluctuation as a function of spanwise separation. Uniform grid spacings are used in the streamwise and spanwise directions with grid spacings. The grids in the wall-normal direction are clustered in the boundary layer with $\Delta z^+ \approx 0.5$ at the wall, and kept uniform with $\Delta z^+ \approx 5$ in the free stream until up to approximately $5.5\delta_i$ or 3.2δ (Figure 2), where δ_i and δ represent the mean boundary layer thickness based on
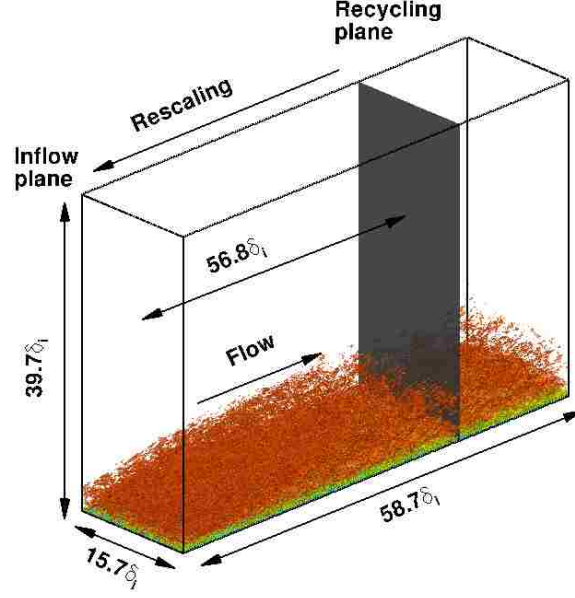
Figure 1. Computational domain and simulation setup for baseline DNS case.

Table 2. Grid resolution and domain size for the direct numerical simulation.

$N_x \times N_y \times N_z$	L_x/δ_i	L_y/δ_i	L_z/δ_i	Δx^+	Δy^+	Δz^+_{min}	Δz^+_{max}
$1600 \times 800 \times 500$	58.7	15.7	39.7	9.63	5.14	0.51	5.33

$u/U_\infty = 0.99$ at the inflow boundary and at the downstream location selected for statistical analysis ($x_a = 54.1\delta_i$), respectively. Such wall-normal grids are designed to adequately resolve both the boundary layer and the near field of acoustic fluctuations radiated by the boundary layer. The '+' superscript denotes non-dimensionalization by the viscous length scale $z_\tau = \nu_w/u_\tau$, where ν_w is the kinematic viscosity at the wall and $u_\tau = \sqrt{\tau_w/\rho_w}$ is the friction velocity (τ_w is the wall-shear stress and ρ_w is the density at the wall). Unless otherwise stated, the grid resolutions given in this section are normalized by the viscous length scale z_τ at the selected downstream location x_a. Analysis of the simulation database has also shown that the Kolmogorov length scale at x_a is comparable to the local viscous length.
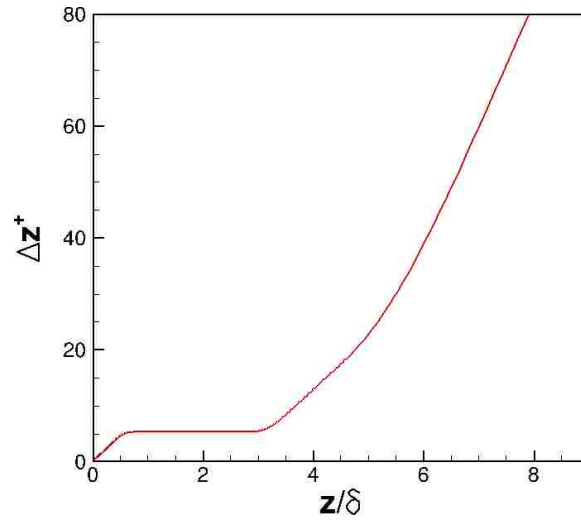
Figure 2. The wall-normal grid distribution.

(a) δ/δ_i

(b) δ^*/δ_i

(c) Re_τ

(d) p'_{rms}/τ_w at $z/\delta_i = 0$ and 4.5
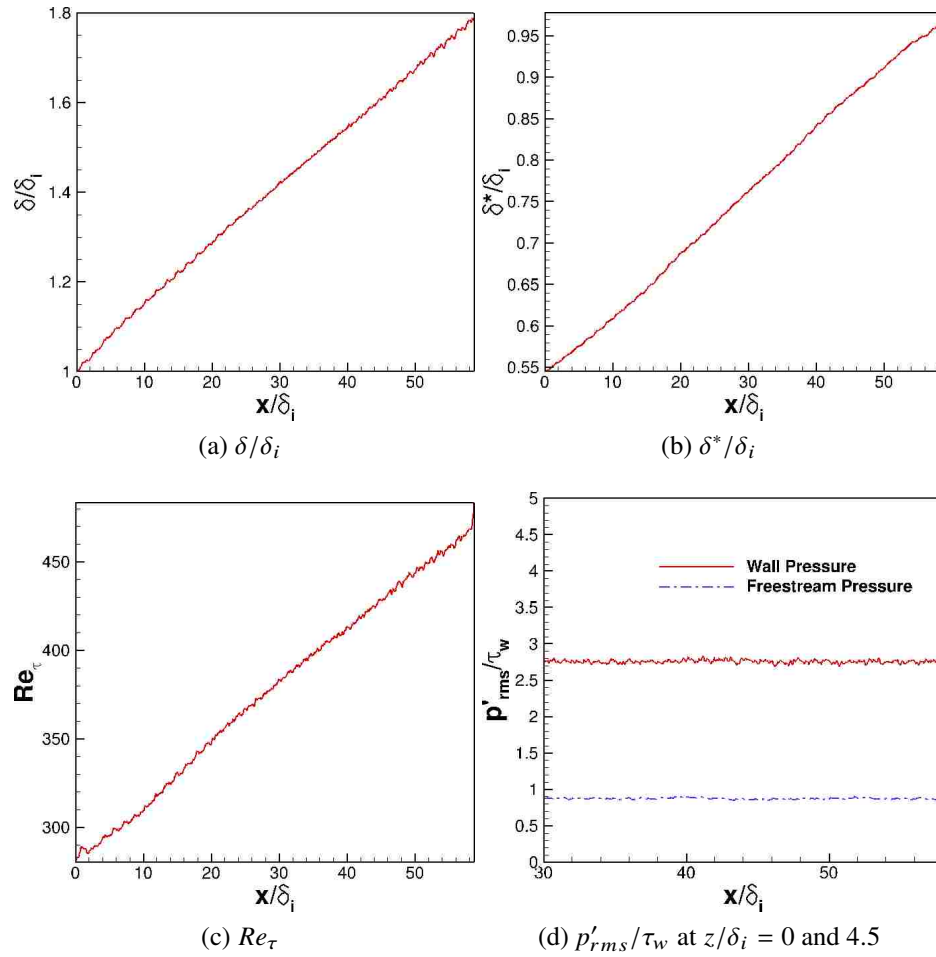
Figure 3. Evolution of boundary-layer parameters with streamwise distance.

The turbulent inflow is generated using the recycling/rescaling method developed by Xu and Martín (2004) with the recycling station set at $56.7\delta_i$ downstream of the inlet. The selected rescaling length is similar to the range of the optimum recycling length of approximately $30\delta_i$ to $99\delta_i$ as suggested by Simens *et al.* (2009) to accommodate the eddy decorrelation length and to minimize inlet transients as a result of the recycling process. The original rescaling method is modified by adding the dynamic translation operations (Morgan *et al.*, 2011) to improve low-frequency characteristics of the generated inflow turbulence and by including a free-stream filter to remove artificial free-stream acoustics at the inlet of the computational domain introduced due to the coupling between the recycling and inflow plane (Duan *et al.*, 2014). This removal of recycled fluctuations in the free stream ensures that the free-stream acoustic disturbances within the domain are radiated entirely from the boundary-layer turbulence rather than convected downstream from the artificial inflow. In addition, numerical experiments have been conducted with varying filter type and filtering location to ensure that the free-stream filtering has negligible effects on the pressure statistics at the selected downstream location for statistical analysis ($x_a = 54.1\delta_i$).

On the wall, no-slip conditions are applied for the three velocity components and an isothermal condition is used for the temperature with $T_w \approx 0.76T_r$. The density is computed from the continuity equation. At the top and outlet boundaries, unsteady non-reflecting boundary conditions based on Thompson (1987) are imposed. Periodic boundary conditions are used in the spanwise direction.

For the current spatial simulations, the boundary layer grows slowly in the streamwise direction, with both the boundary-layer thickness δ and the displacement thickness δ^* increasing by a factor of approximately two across the length of the simulation domain (Figure 3). Correspondingly, the Karman number Re_τ increases from approximately 200 at the inlet to 500 at the outlet, with a useful range of $Re_\tau = 350 - 460$ where the boundary layer has recovered from the initial transient due to the recycling method. The stremwise

computational domain is large enough for the memory of the inflow generation to fade out and a nearly uniform acoustic radiation field to be established. In particular, Figure 3d shows that the pressure fluctuations at the wall and in the free stream have become nearly homogeneous in the streamwise direction after $x/\delta_i \approx 30$. In the following section, averages are first calculated over a streamwise window of $[x_a - 0.9\delta_i, x_a + 0.9\delta_i]$ ($x_a = 54.1\delta_i$) and spanwise locations for each instantaneous flow field; then, an ensemble average over 153 flow field snapshots spanning a time interval of approximately $240\delta_i/U_\infty$ (corresponding to $12.5\delta_i/u_\tau$) is calculated. To monitor the statistical convergence, flow statistics are computed by averaging over the whole or half the number of the flow-field snapshots, and a negligible difference ($< 1\%$) is observed between the two.

Power spectra are calculated using the Welch method (Welch, 1967) with eight segments and 50% overlap. A Hamming window is used for weighting the data prior to the fast Fourier transform (FFT) processing. The sampling frequency is approximately $63U_\infty/\delta_i$, or 4 MHz, and the length of an individual segment is approximately $53.2\delta_i/U_\infty$.

2.3. VALIDATION OF DNS DATA

The velocity statistics (including the mean and root mean square (r.m.s.) values) are reported in this section at a selected downstream location for statistical analysis ($x_a = 54.1\delta_i$), which are also used in the analysis of fluctuating pressure field in Section 3. Table 2 lists the values of the mean boundary layer parameters at the selected location, including the momentum thickness θ and shape factor $H = \delta^*/\theta$ (where δ^* denotes the local displacement thickness). The local boundary layer thickness δ is approximately $\delta \approx 1.7\delta_i$. The outer and inner length scales (boundary layer thickness δ and viscous length scale z_τ, respectively) and the velocity scales u_τ and $u_\tau \sqrt{\rho_w/\rho_\infty}$ are also shown along with the representative Reynolds number parameters, $Re_\theta \equiv \rho_\infty U_\infty \theta/\mu_\infty$, $Re_\tau \equiv \rho_w u_\tau \delta/\mu_w$, and $Re_{\delta 2} \equiv \rho_\infty U_\infty \theta/\mu_w$. Throughout this paper, the subscripts ∞ and w are used to denote quantities at the boundary layer edge and at the wall, respectively.

Table 3. Boundary layer properties at the station selected for the analysis ($x_a = 54.1\delta_i$) of the acoustic field for the present DNS.

$T_w(k)$	T_w/T_r	Re_θ	Re_τ	$Re_{\delta 2}$	θ(mm)	H	δ(mm)	$z_\tau(\mu$m)	u_τ(m/s)
300	0.76	9455.4	453.1	1745.7	0.948	13.6	23.77	52.6	45.07
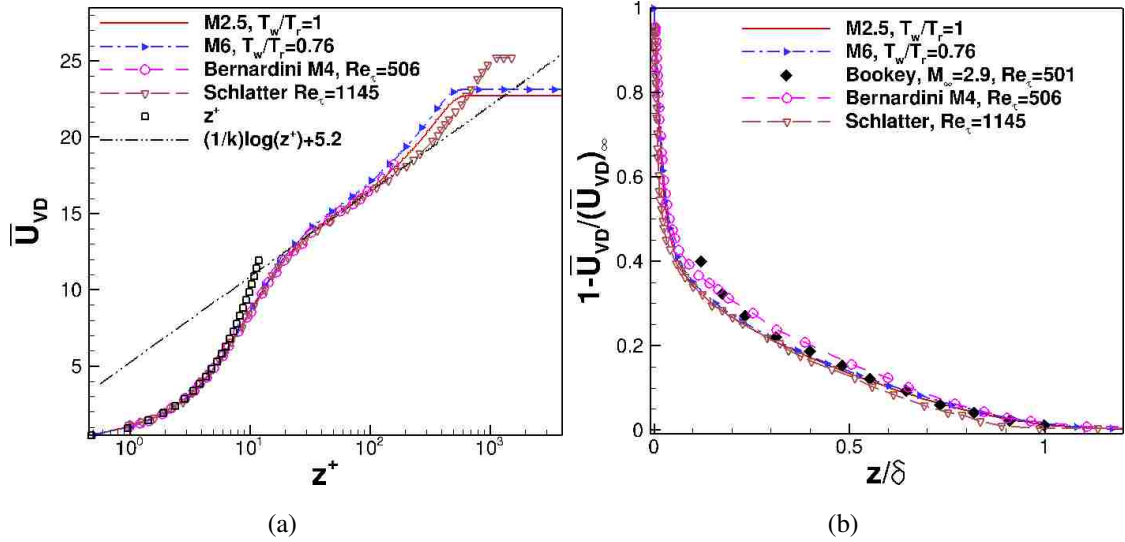
Figure 4. (a) van Driest transformed mean velocity profile (k=0.41, C = 5.2) and (b) van Driest transformed mean deficit velocity.

The van Driest transformed mean velocity profile based on the DNS is shown in Figure 4. Symbols denote the DNS by Bernardini and Pirozzoli (2011) at Mach 4, Re_τ = 506 (circles), the experiment by Bookey *et al.* (2005) at Mach 2.9, Re_τ = 501 (diamonds), and the experiment by Schlatter and Örlü (2010) for an incompressible boundary layer at Re_τ = 1145 (inverted triangles). $\bar{U}_{VD}$ is defined as

$$\bar{U}_{VD} = \frac{1}{u_\tau} \int_0^U (\overline{T_w}/\overline{T})^{1/2} dU. \tag{1}$$

The mean velocity conforms well to the incompressible law-of-the-wall upon van Driest transformation and shows a (narrow) logarithmic region that is comparable in extent to Mach 4 simulations by Bernardini and Pirozzoli (2011) at similar Re_τ. In addition,

the transformed mean-velocity profile compares well with the experimental results by Schlatter and Örlü (2010) for an incompressible boundary layer at $Re_\tau = 1145$ and by Bookey *et al.* (2005) at Mach 2.9, $Re_\tau = 501$. Figures 5(*a–f*) plot turbulence intensities and density weighted turbulence intensities in streamwise, spanwise and wall-normal directions across the boundary layer. —— (red): Mach 5.86, $M_\infty = 5.86$, $Re_\tau = 453.1$, $T_w/T_r = 0.76$. –·–·– (blue): Mach 2.5, $M_\infty = 2.5$, $Re_\tau = 509.9$, $T_w/T_r = 1$. −−−: M5T4 (Duan *et al.*, 2010), $M_\infty = 5$, $Re_\tau = 433.8$, $T_w/T_r = 0.68$. $\diamond$: M5T5 (Duan *et al.*, 2010), $M_\infty = 5$, $Re_\tau = 385.9$, $T_w/T_r = 1$. $\square$ (red), (Spalart, 1988), $M_\infty \approx 0$, $Re_\theta = 1410$. $\triangle$ (blue), (Spalart, 1988), $M_\infty \approx 0$, $Re_\theta = 670$. $\triangledown$, (Pirozzoli and Bernardini, 2011), $M_\infty = 2$, $Re_\tau = 497$. • (green), (Bernardini and Pirozzoli, 2011), $M_\infty = 4$, $Re_\tau = 506$. $\triangleleft$ (violetred), (Peltier *et al.*, 2012), $M_\infty = 4.9$, $Re_\theta \approx 40 \times 10^3$, $T_w/T_r = 0.9$. ■ (red), (Piponniau *et al.*, 2009), $M_\infty = 2.28$, $Re_\theta = 5100$. ♦, (Eléna and Lacharme, 1988), $M_\infty = 2.32$, $Re_\theta = 4700$. ◀ (blue), (Schlatter and Örlü, 2010), $M_\infty \approx 0$, $Re_\tau = 1145$. A significantly improved collapse of data is achieved by Morkovin's scaling, which takes into account the variation in mean flow properties. Morkovin's scaling brings the magnitudes of the extrema in the compressible cases closer to the incompressible results of Spalart (1988) and Schlatter and Örlü (2010), allowing the present DNS to compare well with existing data at similar conditions.

The physical realism and accuracy of the computed flow fields have been further established by comparing with existing experimental results at similar flow conditions. Figure 6 shows the comparison of DNS results (Case M6Tw076) with the wind-tunnel measurement and the calculation using Harris Boundary-layer code (Harris and Blanchard, 1982) for a Mach 5.8 turbulent boundary layer on the nozzle wall of BAM6QT under noisy-flow conditions ($Re = 9.69 \times 10^6$/m, $P_{t,\infty} = 965$ kPa, $T_{t,\infty} = 429$ K) (Casper, 2011; Steen, 2010).

The Pitot-probe measurement of the boudnary-layer profiles was conducted by Steen (2010); the calculation of the boundary-layer profiles using Harris boundary-layer Code (Harris and Blanchard, 1982) and the measurement of the wall pressure spectrum were con-
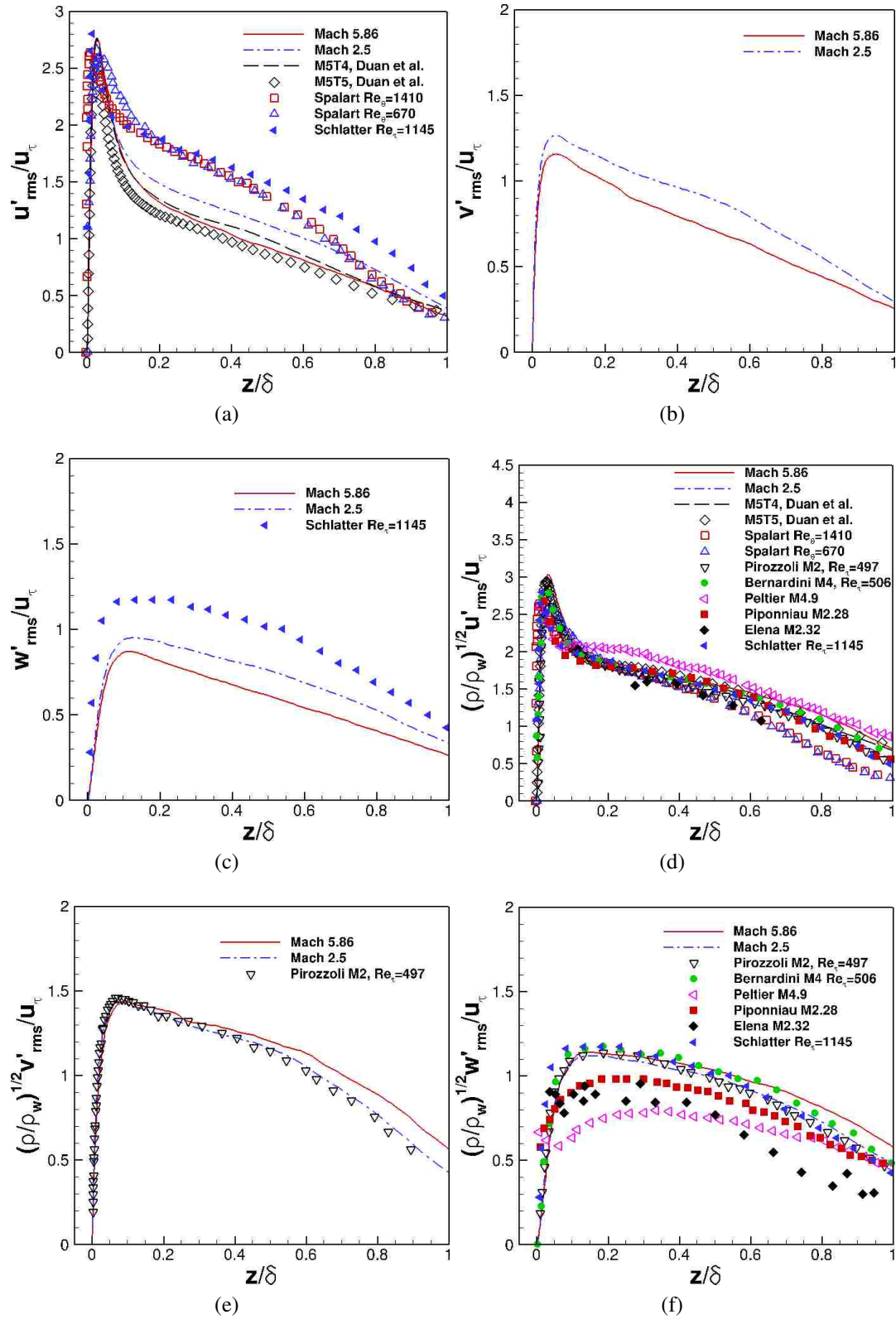
Figure 5. Turbulence intensities and density-weighted turbulence intensities of the (a,d) streamwise, (b,e) spanwise and (c,f) wall-normal fluctuating velocity components.

(a) Mean velocity profile

(b) Mach number profile
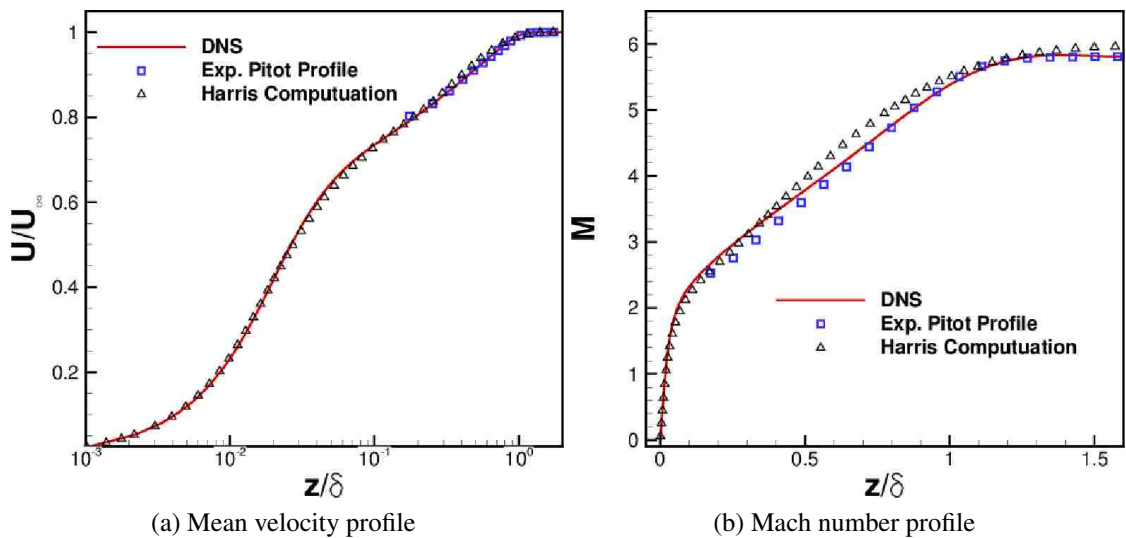
Figure 6. Comparison of DNS results with those of a Mach-5.8 turbulent boundary layer on the nozzle wall of the Boeing/AFOSR Mach-6 Quiet Tunnel under noisy-flow conditions. (Mean value)

ducted by Casper (2011). The experimental curve of wall pressure spectrum is normalized with DNS-computed parameters and includes the Corcos correction for finite probe size (Beresh *et al.*, 2011). The DNS and experiments agree well with each other in terms of both boundary-layer profile and wall-pressure spectrum. In comparison, the Mach number profile based on the boundary layer code exhibits larger differences from the measurement and the DNS in the outer part of the boundary layer. Moreover, Figure 7a and Figure 7b show that DNS extends the measured spectra to higher frequencies. The resolution of the high-frequency region as well as the acoustic radiation due to these high-frequency fluctuations are especially important for studying the receptivity process associated with second-mode waves in hypersonic wind tunnels.

Additional comparisons of DNS results with both experiments and other high-quality simulations are presented in the following sections, including pressure statistics, frequency spectra, two-point correlations, propagation speed and free-stream acoustic radiation.

(a) Frequency spectrum in outer scale   (b) Frequency spectrum in inner scale
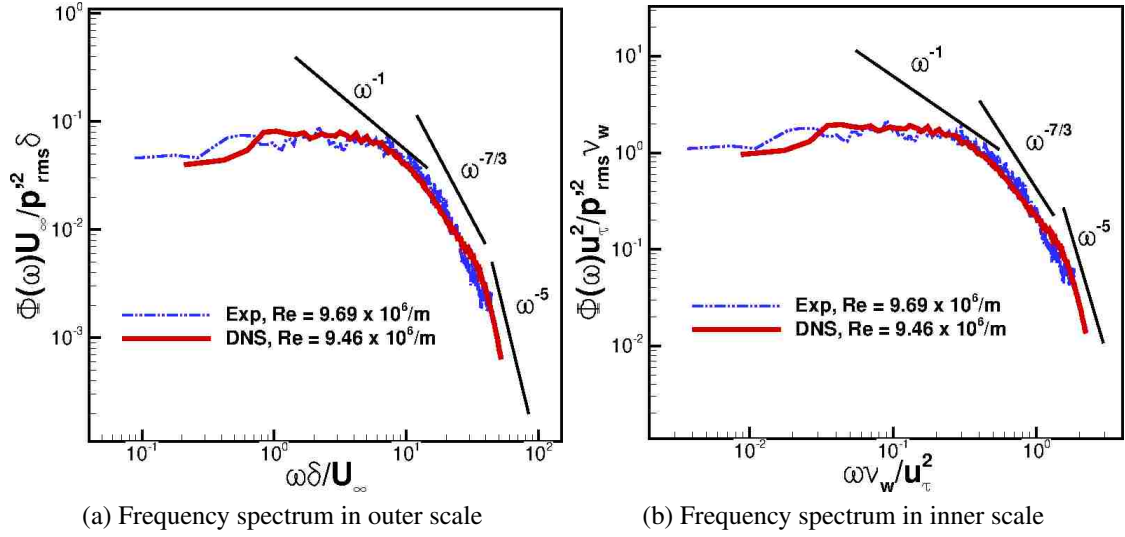
Figure 7. Comparison of DNS results with those of a Mach-5.8 turbulent boundary layer on the nozzle wall of the Boeing/AFOSR Mach-6 Quiet Tunnel under noisy-flow conditions. (Frequency spectrum)

3. RESULTS

3.1. PRESSURE STATISTICS

Figures 8a shows the r.m.s. of pressure fluctuations normalized by the local wall shear for the present DNS and some of previous DNS results at lower Mach numbers with similar Reynolds numbers (Bernardini and Pirozzoli, 2011; Duan *et al.*, 2014). At the wall, the value of p'_{rms}/τ_w at Mach 5.86 is approximately 2.8, which is close to 3 based on the model by Bies (1966) and those given by the DNS of Bernardini and Pirozzoli (2011); Guarini *et al.* (2000); Spalart (1988) at lower Mach numbers. p'_{rms}/τ_w is insensitive to Mach number variation within most of the boundary layer and collapses with lower Mach-number data. Outside the boundary layer, however, p'_{rms}/τ_w approaches a constant value of approximately 0.9 for the Mach 5.86 case, which is significantly larger than the value of 0.4 for the Mach 2.5 turbulent boundary layer. The variation of free-stream pressure fluctuations with Mach number is consistent with the trend predicted by the experimental
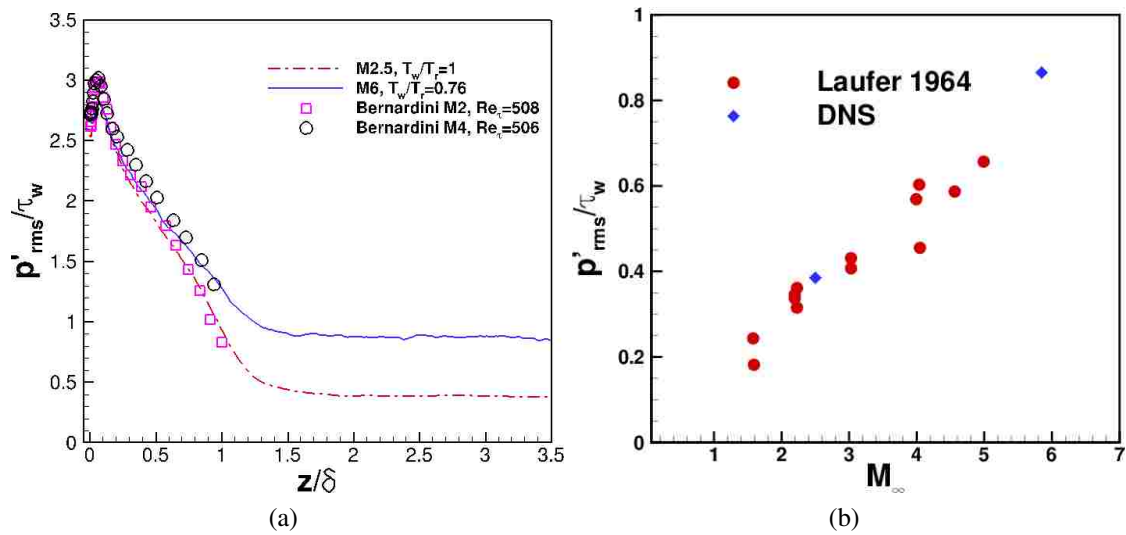
Figure 8. (a) Pressure fluctuation rms profile p'_{rms}/τ_w as a function of wall-normal distance. (b) Comparison of p'_{rms}/τ_w in the free stream with the experiments by Laufer (1964)

data reported by Laufer (1964) (Figure 8b). Whenever all four walls of the rectangular test section were radiating to the measurement location, Laufer obtained the contribution to the acoustic fluctuations from a single wall by assuming equal contributions from each wall. This assumption was validated by comparing the measured fluctuations with those in the case where only one wall had a turbulent boundary layer and the rest had laminar boundary layers. The increase in radiation intensity with free-stream Mach number in Figure 8b is consistent with the 'eddy Mach wave' hypothesis (Phillips, 1960), which states that the 'Mach wave type' radiation is produced by eddies that convect supersonically with respect to the free stream. At low supersonic free-stream Mach numbers, sources that contribute primarily to the radiation field are slowly moving ones, the convection velocities of which are supersonic relative to the free stream (see Figure 21). As the Mach number increases, additional faster moving turbulent eddies acquire supersonic relative speeds and start to take part in the radiation process, accounting for the larger acoustic amplitudes in the free stream.

3.2. FREQUENCY SPECTRA

The frequency spectrum of the pressure fluctuations is defined as

$$\Phi_p(\omega) = \frac{1}{2\pi} \int_{-\infty}^{\infty} \overline{p'(x,y,z,t)p'(x,y,z,t+\tau)}e^{-i\omega\tau}d\tau \qquad (2)$$

The pressure spectrum can be divided into several segments with different power-law scalings. According to Bull (1996), the pressure spectrum can be broken into regions of low, mid, mid-to-high overlap, and high frequencies, with corresponding spectrum slopes of ω^2, ω^{-1}, $\omega^{-7/3}$, and ω^{-5}, respectively. The ω^2 dependence of the pressure spectrum at the lowest frequencies ($\omega\delta^*/U_\infty < 0.03$) is induced by passive structures in the outer layer of the boundary layer. The ω^{-1} dependence of the pressure spectrum at mid frequencies is typically attributed to convected turbulence in the logarithmic region where the pressure-inducing eddies has a length scale proportional to the distance from the wall (Bradshaw, 1967) . The $\omega^{-7/3}$ scaling of the pressure spectrum lies in the overlap region between mid and high frequencies and is attributed to eddies in the highest part of the buffer region ($20 < z^+ < 30$). Such a region is analogous to the inertial subrange in the velocity spectra that is described by Kolmogorov's $-5/3$ law. The typical frequency range for this region is $0.3 < \omega\nu/u_\tau^2 < 1$. The ω^{-5} dependence of the pressure spectrum at high frequencies is attributed to sources in the boundary layer below $z^+ = 20$; and this region is referred to as the sublayer dominance by Blake (1986).

Figure 9a shows the pressure spectrum as a function of the wall-normal distance for the present DNS. The free stream are taken at $z/\delta = 2.63$ for the Mach 5.86 DNS and $z/\delta = 2.8$ for the Mach 2.5. The pressure spectrum is normalized so that the area under each curve is equal to unity. For reference, straight lines with slopes of 2, -1, $-7/3$, and -5 are also included to gauge the rate of spectral roll-off across relatively low, mid, overlap, and high frequencies, respectively. The vertical lines in the plots ($\omega\nu_w/u_\tau^2 = 0.3$ and

$\omega \nu_w / u_\tau^2 = 1.0$) demarcate the overlap regions between mid and high frequencies and show the estimated locations where a slope change in pressure spectrum is predicted according to the theory by Bull (1996).

The pressure spectrum shows a rather weak frequency dependence up to the lowest frequencies covered by the DNS ($\omega \delta^* / U_\infty \approx 0.08$). The absence of the more rapid and incompressible ω^2 scaling as $\omega \to 0$ at low frequencies in the wall-pressure spectrum is consistent with the measurements by Beresh *et al.* (2011); Casper (2011) and the DNS by Bernardini and Pirozzoli (2011) at supersonic Mach numbers. At all wall-normal locations, there is little evidence of the ω^{-1} region at mid-frequencies. Given that ω^{-1} dependence of the pressure spectrum is attributed to sources within the logarithmic region of the boundary layer, the absence of the ω^{-1} region is consistent with the relatively low Reynolds number ($Re_\tau \approx 500$) as well as the small logarithmic region of the current DNS. In the overlap region between the mid and high frequencies, the pressure spectrum deviates from Kolmogorov's $-7/3$ scaling and shows a slope of $\omega^{-1.6}$ at the wall. As the location of interest moves away from the wall, the deviation from the Kolmogorov scaling becomes smaller. The deviation from the Kolmogorov scaling is expected given the non-zero shear rate within the boundary layer. As a result, local isotropy cannot be realized for the current Reynolds number (Tsuji *et al.*, 2007).

The reduced deviation from the Kolmogorov's $-7/3$ scaling away from the surface can be attributed to the progressive reduction in the local shear rate. The relation between the $\omega^{-7/3}$ scaling of the pressure spectrum and the shear rate has previously been explained by Bernardini *et al.* (2011), who observed the $\omega^{-7/3}$ behavior of wall-pressure spectrum in a supersonic turbulent boundary layer with adverse pressure gradient and showed that such a scaling is related to a reduction of the shear rate induced by an adverse pressure gradient. At high frequencies, the spectrum exhibits a slightly more rapid decay than the ω^{-5} scaling predicted theoretically by Blake (1986), and the energy content becomes progressively lower as the location of interest moves away from the wall.

Figures 9b and 9c show a comparison of the pressure spectrum at the wall and in the free stream, respectively, for the present DNS at Mach 5.86 and that of a Mach 2.5 turbulent boundary layer (Duan *et al.*, 2014). The higher Mach-number case exhibits significantly higher energy than the lower Mach number case at high frequencies. A similar dependence of pressure spectrum on Mach number was shown in the experiments by Laufer (1964). While an observable region of slope close to $-7/3$ is absent in the free-stream pressure spectrum of the Mach 5.86 DNS, the free-stream spectrum for the Mach 2.5 case has an observable region of slope close to $-7/3$, indicating a possible influence of Mach number on the overlap region of the pressure spectrum. A similar Mach-number dependence of the free-stream pressure spectrum has been observed by Masutti *et al.* (2012).

To illustrate the distribution of energy among various frequencies, Figure 10a shows the pre-multiplied pressure spectra at selected heights above the surface. It is shown that the pressure spectra in the inner layer have a dominant hump centered on $\omega\delta/U_\infty \approx 8$ (or $f\delta/U_\infty \approx 1$), which is the characteristic frequency of the energetic vortical structures within the boundary layer.

As one moves away from the wall into the outer layer, the peak gradually shifts to lower frequencies as spatial intermittency becomes more important. In the free stream, where the pressure signal is predominantly acoustic, the peak of the spectrum is centered at a frequency of $\omega\delta/U_\infty \approx 3$ (i.e. $f \approx 10.8$ kHz), indicating that characteristic frequency of the acoustic fluctuations is significantly lower than that of the vorticity mode. Similar variation in pre-multiplied pressure spectrum with wall-normal distance is observed for the Mach 2.5 case.

Figure 10b further compares the pre-multiplied spectra for the two Mach number cases at the wall and in the free stream. While the wall spectrum is centered on nearly the same frequency $\omega\delta/U_\infty \approx 8$ at both Mach numbers, the free-stream spectrum for the Mach 5.86 case peaks at a significantly higher frequency than the Mach 2.5 case. The pressure spectrum is normalized so that the area under each curve is equal to unity. The free stream
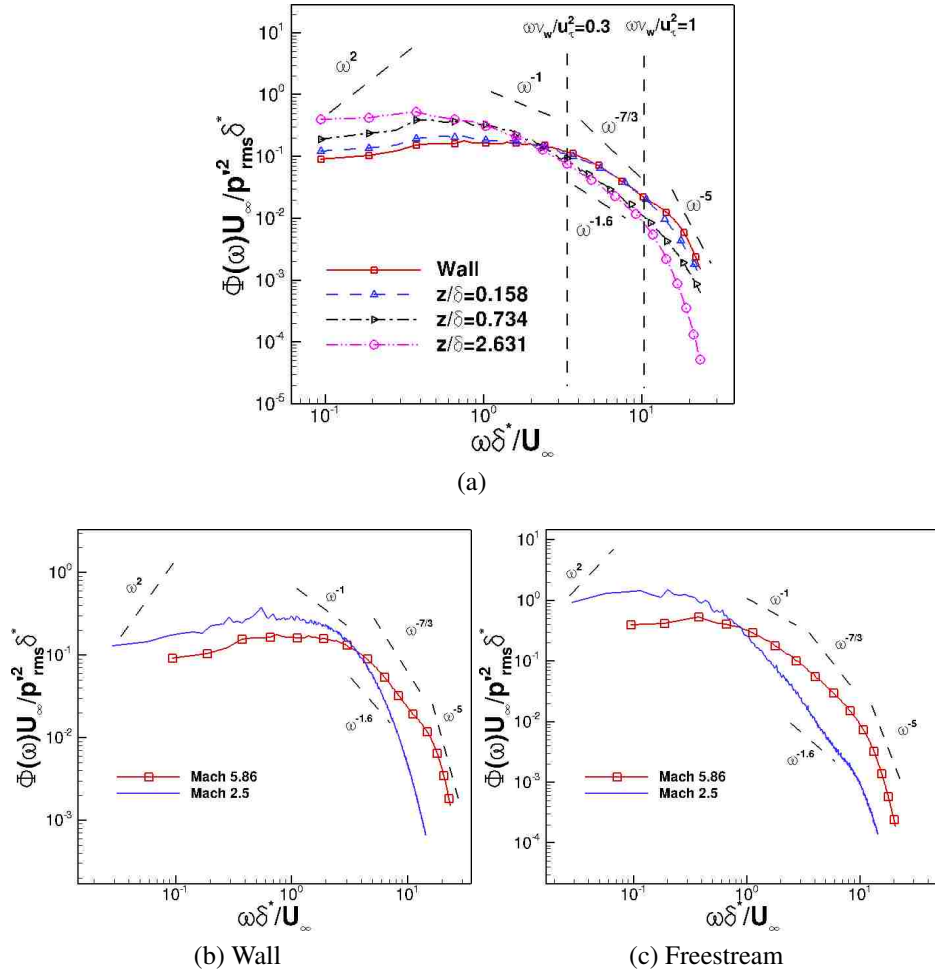
Figure 9. (a) Normalized frequency spectrum of computed pressure signal at selected heights for the Mach 5.86; (b), (c) Comparison of pressure spectrum at the wall and in the free stream between the Mach 5.86 DNS and the Mach 2.5 DNS Duan *et al.* (2014).
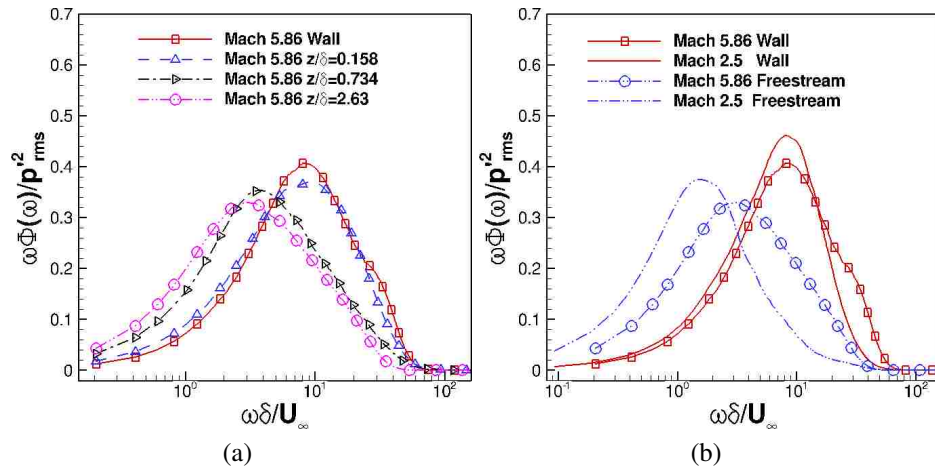
Figure 10. Pre-multiplied power spectrum of pressure signals.

are taken at $z/\delta = 2.63$ for the Mach 5.86 DNS and $z/\delta = 2.8$ for the Mach 2.5. The reduced gap in the dominant frequency between pressure signals at the wall and in the free stream can be explained by the 'eddy Mach wave radiation' concept (Ffowcs-Williams and Maidanik, 1965; Phillips, 1960).

As the Mach number increases, additional faster-moving turbulent eddies acquire supersonic relative speeds and start in the radiation process. The increased fraction of the inner layer that can radiate to the free stream contributes to a reduced gap between the peak frequency of fluctuations near the surface and in the free stream.

3.3. TWO-POINT CORRELATIONS

3.3.1. Two-Point Correlations in Streamwise-Spanwise Planes. The two-point correlation coefficient of the pressure field in a streamwise-spanwise plane is defined as

$$C_{pp}(\Delta x, \Delta y, z) = \frac{\overline{p'(x,y,z,t)p'(x+\Delta x, y+\Delta y, z, t)}}{\left(\overline{p'^2(x,y,z,t)}\right)^{1/2}\left(\overline{p'^2(x+\Delta x, y+\Delta y, z, t)}\right)^{1/2}} \tag{3}$$

where Δx and Δy are spatial separations in the streamwise and spanwise directions, respectively.

Figure 11 displays the contours of streamwise-spanwise correlation $C_{pp}(\Delta x, \Delta y, z)$ of the pressure fluctuations across a range of wall-normal heights for the present DNS and the Mach 2.5 case of Duan *et al.* (2014). Contour levels vary from 0.1 to 0.9 with increments of 0.1. The contours of C_{pp} are approximately circular for small spatial separations but become elongated in the spanwise direction for large separation distances, indicating that the small-scale pressure-carrying eddies or wavepackets are nearly isotropic while the large-scale eddies become more coherent in the spanwise direction. The extent of the pressure contours increases in both in-plane directions as the wall-normal height increases. The two-point correlations of the pressure fluctuations in the free stream show similar patterns to those within the boundary layer, except for a variation in spatial length scales. Within

the boundary layer, the pressure contours exhibit a minor Mach number dependence when nondimensionalized by the boundary layer thickness. In the free stream, however, the large-scale pressure wavepackets for the Mach 5.86 case become less elongated in the spanwise direction compared with the lower Mach number case.

Figures 12a and 12b show the variation of streamwise and spanwise length scales of the pressure field ($(\Lambda_x)_p$ and $(\Lambda_y)_p$), respectively, as a function of wall-normal distance.

The streamwise and spanwise length scales of the pressure field display an approximate increase with wall-normal coordinate within most of the boundary layer, reaching a peak just outside the boundary-layer edge. For approximately $z/\delta > 2$, both scales again relax to approximately constant values that are nearly twenty-five percent lower than the respective peaks. Such a dependence of length scales on the wall-normal coordinate is consistent with wall-normal variation of the extent of pressure correlation contours shown in Figure 11. The nearly linear increase of pressure length scales with wall-normal location in the outer region of the boundary layer is consistent with the conceptual model of very large-scale motion (VLSM) proposed by Kim and Adrian (1999). Similar wall-normal variation of large-scale coherence has been revealed by particle image velocimetry (PIV) experiments of turbulent boundary layers at low and supersonic speeds (Ganapathisubramani *et al.*, 2005, 2006; Tomkins and Adrian, 2003) based on two-point correlations of streamwise velocity fluctuations.

3.3.2. Two-Point Correlations in Streamwise Wall-Normal Planes. The two-point correlation coefficient of the pressure field in a streamwise wall-normal plane is defined as

$$C_{pp}(\Delta x, z, z_{ref}) = \frac{\overline{p'(x,y,z_{ref},t)p'(x+\Delta x,y,z,t)}}{\left(\overline{p'^2(x,y,z_{ref},t)}\right)^{1/2}\left(\overline{p'^2(x+\Delta x,y,z,t)}\right)^{1/2}} \qquad (4)$$

where Δx is spatial separations in the streamwise direction and z_{ref} is the reference wall-normal location at which the correlation is computed.
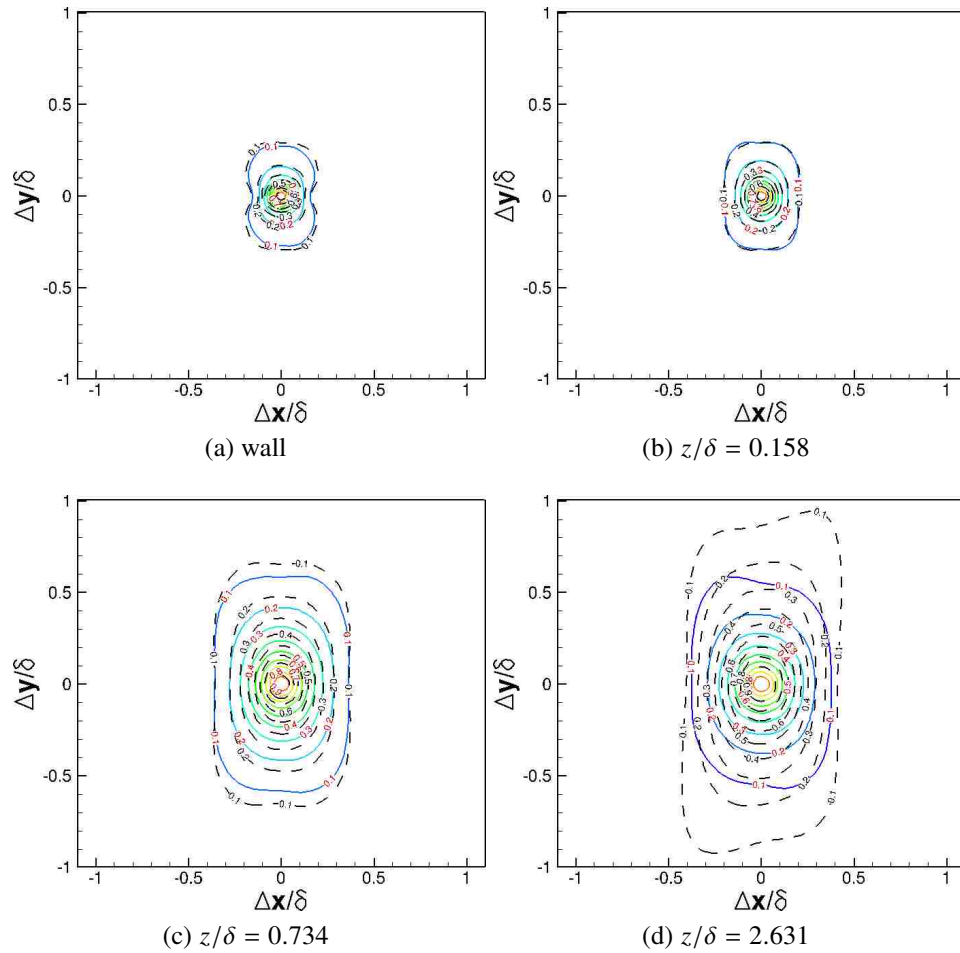
Figure 11. Contours of constant streamwise-spanwise correlation coefficient of the pressure signal $C_{pp}(\Delta x, \Delta y)$ at selected heights for Mach 5.86 (Colored solid line) and Mach 2.5 (Black dashed line).
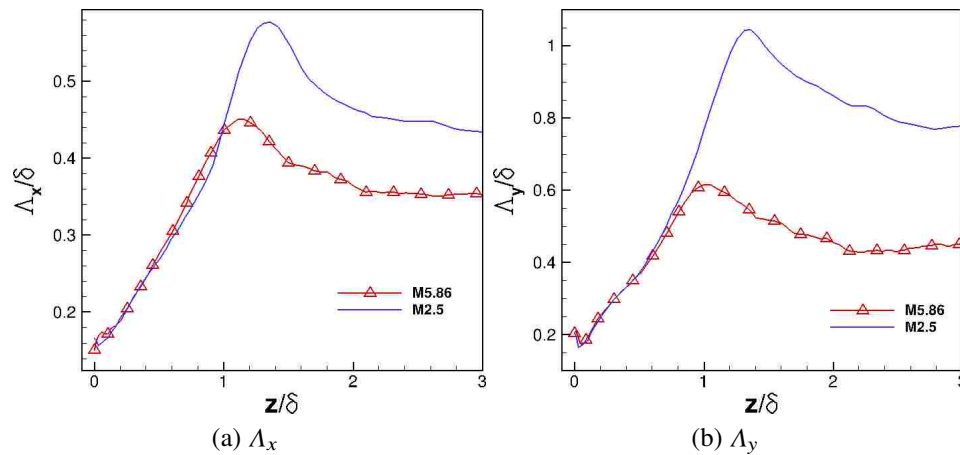
Figure 12. (a) Streamwise Λ_x and (b) spanwise Λ_y integral length scales as a function of the wall-normal location.

(a) $z_{ref}/\delta = 0$

(b) $z_{ref}/\delta = 0.158$

(c) $z_{ref}/\delta = 0.734$

(d) $z_{ref}/\delta = 2.631$
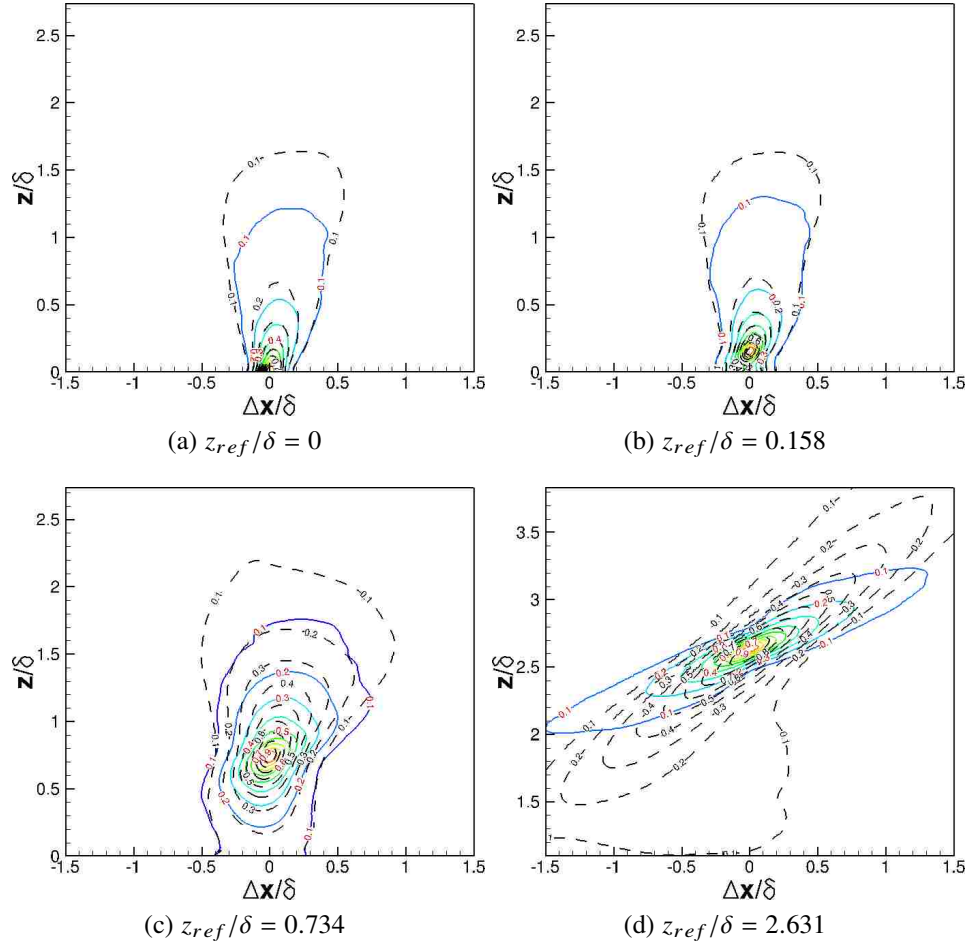
Figure 13. Streamwise wall-normal correlation coefficient of the pressure signal C_{pp} at selected heights for Mach 5.86 (Colored solid line) and Mach 2.5 (Black dashed line).

Contours of constant $C_{pp}(\Delta x, z, z_{ref})$ for the present Mach 5.86 DNS at multiple reference heights z_{ref} are shown in Figure 13. Contour levels vary from 0.1 to 0.9 with increments of 0.1. The same contours for the Mach 2.5 DNS (Duan *et al.*, 2014) are also included to highlight the differences from the lower Mach number case. For each reference height z_{ref}, the maximum correlation of pressure fluctuations is approximately aligned along a line, indicating the presence of downward-leaning structures. At the wall, the structure of pressure fluctuations is inclined approximately $\theta_{xz} \approx 80°$ to the wall. The inclination angle decreases gradually in the inner and outer regions of the boundary layer. In the free stream, the inclination angle of the pressure structure plateaus to $\theta_{xz} \approx 21°$. The

variation in θ_{xz} with wall-normal distance indicates that pressure disturbances generated within the boundary layer will undergo significant refraction before they are radiated to the free stream. The free-stream pressure wave-front inclination θ_{xz} closely matches the wave-front orientation of the instantaneous acoustic radiation visualized by numerical Schlieren imaging as shown in Figure 20a.

The pressure-structure angle exhibits minor Mach number dependence within the boundary layer. In the free stream, however, the pressure wave front is significantly shallower for the higher Mach number case. The shallower wave front of the free-stream radiation for the higher Mach number case is consistent with the decrease in the zone of influence of a flow disturbance as Mach number increases.

3.3.3. Space-Time Correlation.

The space-time of the pressure field is defined as

$$C_{pp}(\Delta x, \Delta t) = \frac{\overline{p'(x,y,z,t)p'(x+\Delta x,y,z,t+\Delta t)}}{\left(\overline{p'^2(x,y,z,t)}\right)^{1/2}\left(\overline{p'^2(x+\Delta x,y,z,t+\Delta t)}\right)^{1/2}} \tag{5}$$

where Δx and Δt are spatial separation in the streamwise direction and the time delay, respectively.

The space-time correlation contours of $C_{pp}(\Delta x, \Delta t)$ are plotted at multiple wall-normal locations as shown in Figure 14. Contour levels vary from 0.1 to 0.9 with increments of 0.1. For comparison, the same contours for the Mach 2.5 DNS (Duan *et al.*, 2014) are also included.

At all wall-normal locations, the pressure contours are skewed with the maximum correlation aligned along the first or third quadrant in the $(\Delta x, \Delta t)$-plane. The concentration of contours of $C_{pp}(\Delta x, \Delta t)$ into a narrow band indicates strong downstream propagation of pressure fluctuations. In addition, there is a change in the overall slope of $d\Delta x/d\Delta t$ at different wall-normal locations, indicating a variation of bulk propagation speed of pressure fluctuations as a function of wall-normal distance. The overall larger inclination of the space-time correlation contours in the free stream for the Mach 5.86 case indicates that

the free-stream pressure structures propagate with a larger speed relative to the Mach 2.5 case. A further discussion of the propagation speed of pressure fluctuations, including its dependence on different definitions, will be given in Section 3.4.

Figures 15a and 15b plot the maximum space-time correlation of pressure fluctuations, $(C_{pp})_{max}$, as a function of time delay Δt and streamwise separation Δx, respectively, at multiple wall-normal locations. The scales of temporal and spatial decays in $(C_{pp})_{max}$ are measures of the lifetime and Lagrangian decorrelation length of the coherent pressure structures or wavepackets. Within the boundary layer, the temporal and spatial Lagrangian scales of the pressure structures increase with wall-normal distance and are at least five times larger than the large-eddy turnover time and the boundary layer thickness, respectively. In the free stream, the acoustic pressure fluctuations show similar temporal and spatial decay rates as those near the wall ($z^+ \approx 20$). Given that acoustic sources are concentrated in the near-wall region according to the concept of 'eddy Mach-wave radiation' (Section 4.3), the apparent match in the Lagrangian time and spatial scales between the free-stream pressure structures and the structures near the wall indicates that the free-stream acoustic radiation mainly originates from the near-wall region, a finding that is consistent with the concept of 'eddy Mach waves'.

3.4. PROPAGATION SPEED

The space-time correlation data based on the DNS was used to estimate the speed of propagation of pressure fluctuations. First, for a given time delay Δt, the propagation speed U_c is defined as the ratio $\Delta x / \Delta t$ at the value of Δx where

$$\left. \frac{\partial C_{pp}(r_x, 0, \Delta t)}{\partial r_x} \right|_{r_x = \Delta x} = 0 \tag{6}$$

(a) wall

(b) $z/\delta = 0.158$

(c) $z/\delta = 0.734$

(d) $z/\delta = 2.631$
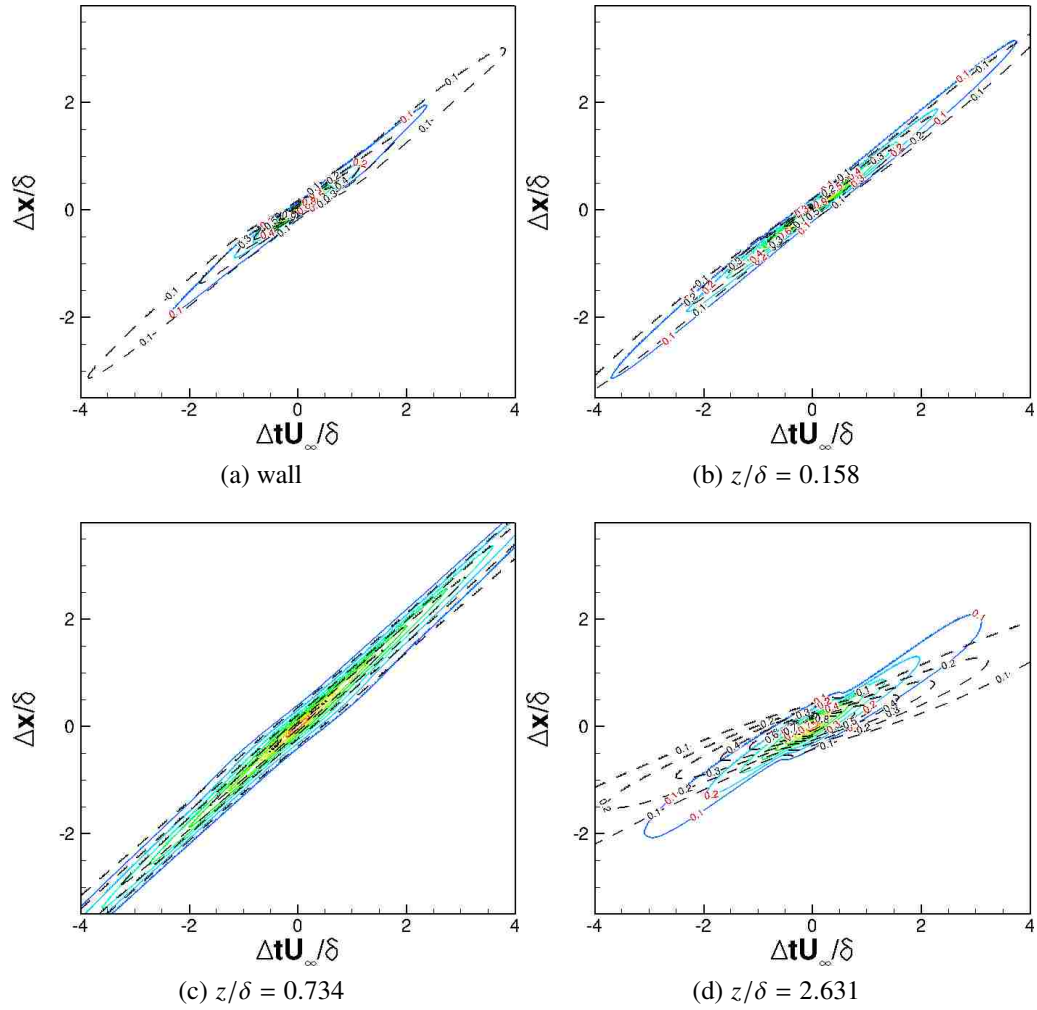
Figure 14. Contours of constant space-time correlation coefficient of pressure fluctuations $C_{pp}(\Delta x, \Delta t)$ at selected heights for Mach 5.86 (Colored solid line) and Mach 2.5 (Black dashed line).

A similar procedure has been used by multiple researchers (Bernardini and Pirozzoli, 2011; Choi and Moin, 1990; Kim, 1989) to define the convection speed of wall-pressure fluctuations. Figure 16a plots the propagation speed as a function of time delay Δt at several selected heights across the boundary layer for the present DNS. As expected, the propagation speed shows a Δt dependence, and there is an increase in U_c at large time separations in the inner and outer layers of the boundary layer ($z/\delta < 1$). Given that only large eddies retain their coherence at large time separations, such an increase in U_c at large Δt may suggest that
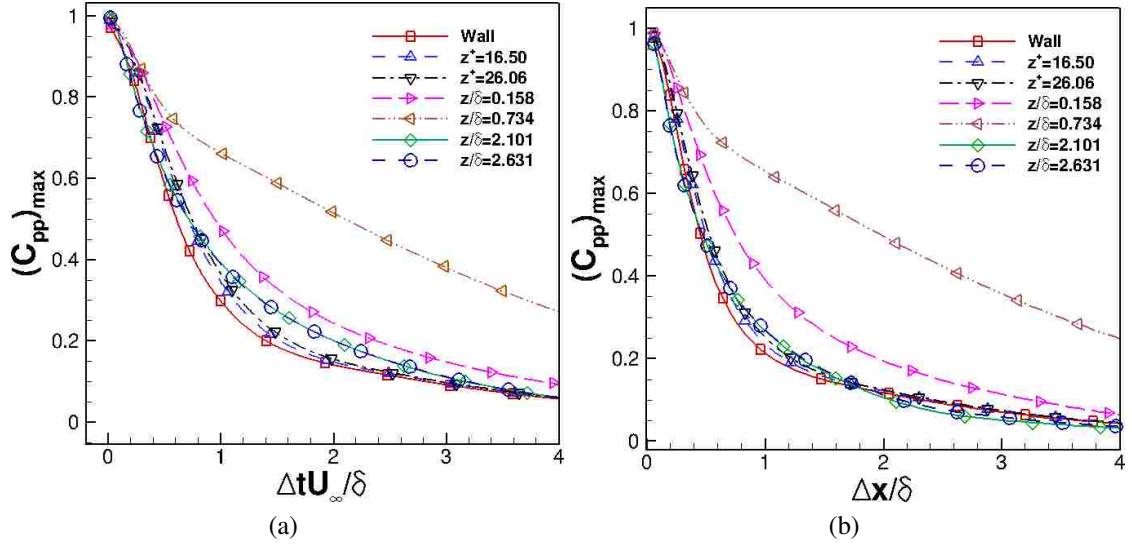
Figure 15. Decay of the maximum spatial-time correlation coefficient of pressure fluctuations, $(C_{pp})_{max}$, as a function of (a) time delay Δt and (b) streamwise separation Δx.

large pressure-carrying eddies/wavepackets propagate with higher speeds than small ones. The propagation speed at the wall is $U_c \approx 0.8U_\infty$ for the large-scale disturbances (associated with large time delay) and $U_c \approx 0.72U_\infty$ for the small-scale disturbances (associated with small time delay). The magnitude of the propagation speed near the surface as well as its scale dependence is in close agreement with both measured and computed values for low-speed and supersonic turbulent boundary-layer flows (Bernardini and Pirozzoli, 2011; Choi and Moin, 1990; Tsuji *et al.*, 2007; Willmarth, 1975). The propagation velocity becomes less scale dependent in the log layer ($z/\delta = 0.16$) and the outer layer ($z/\delta = 0.73$) and the overall range is very close to the local mean velocity. Outside the boundary layer, the propagation speed is again insensitive to Δt and the pressure wavepackets propagate at a significantly smaller speed of $U_c \approx 0.63U_\infty$. Similar findings were reported by Duan *et al.* (2014) for a Mach 2.5 turbulent boundary layer. The significantly smaller propagation speed of the free-stream pressure wavepackets indicates that the acoustic sources that radiate noise into the free-stream convect with a speed much smaller than the free-stream velocity.

As suggested by Laufer (1964), the propagation speed $U_c \equiv \Delta x / \Delta t$ can also be defined for a given Δx and at the value of Δt where

$$\left. \frac{\partial C_{pp}(\Delta x, 0, r_t)}{\partial r_t} \right|_{r_t = \Delta t} = 0 \qquad (7)$$

This definition is consistent with Laufer's experiments (Laufer, 1964) in which two probes with fixed streamwise separation are used to determine the propagation speed. Figure 16b shows a plot of the propagation speed U_c as a function of streamwise separation Δx at selected wall-normal locations. Similar to Figure 16a, the propagation speed in the inner layer increases at large streamwise separations and such an increase becomes less significant as the location of interest moves to the outer layer. In the free stream, U_c / U_∞ is approximately 0.68 for $\Delta x / \delta \approx 0.23$ (corresponding to the probe separation $\Delta x_{Laufer} = 0.71$ centimeters in Laufer's experiment by assuming $\delta_{Laufer} = 3.15$ centimeters).

A third way to quantify the overall propagation speed of pressure-carrying eddies or wavepackets is to find the value of U_b which minimizes the difference between the real time evolution of $p(x, t)$ and a frozen wave $p(x - U_b t)$. Following this definition, the following expression can be obtained

$$U_b \equiv - \frac{\overline{(\partial p / \partial t)(\partial p / \partial x)}}{\overline{(\partial p / \partial x)^2}} \qquad (8)$$

The same definition of bulk propagation speed was introduced by Del Alamo and Jimenez (2009) for the streamwise velocity fluctuations. Similar to the streamwise velocity (Del Alamo and Jimenez, 2009), a figure of merit for the frozen-wave approximation can be introduced for the pressure fluctuations as

$$\gamma_p \equiv \frac{\left| \overline{(\partial p / \partial x)(\partial p / \partial t)} \right|}{\left[\overline{(\partial p / \partial t)^2} \; \overline{(\partial p / \partial x)^2} \right]^{1/2}} \qquad (9)$$

γ_p equals unity for a perfect frozen wave, and zero for fast decaying or deforming waves as they convect downstream. Figure 17 plots the bulk propagation speed of the pressure fluctuation as a function of wall-normal distance. U_b is defined based on 'frozen-wave' approximation as Equation 8 (Del Alamo and Jimenez, 2009) for the Mach 5.86 and Mach 2.5 DNS, and is calculated using Equation 6 with $\Delta t^+ = 18$ for the incompressible DNS by Kim and Hussain (1993).
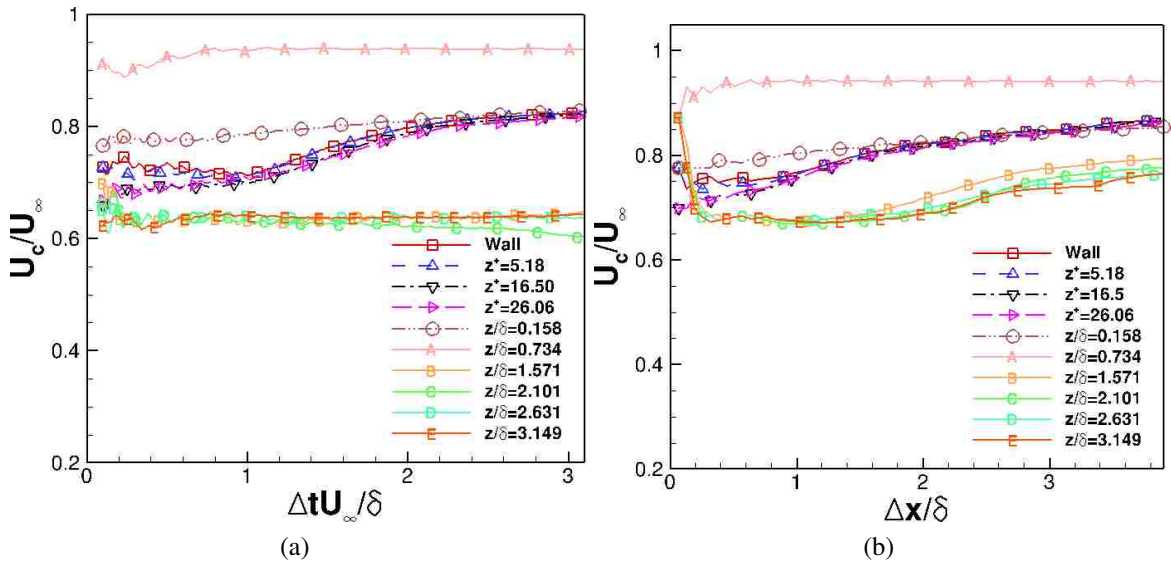
Figure 16. Propagation speed of pressure fluctuations as a function of (a) time delay Δt and (b) streamwise separation Δx for the DNS of Mach 5.86 turbulent boundary layer.

The bulk propagation speed of the pressure fluctuation is significantly larger than the local mean velocity in the viscous sublayer and the buffer layer. The bulk propagation speed of the pressure fluctuation becomes approximately equal to the local mean velocity in the upper buffer layer and remains so over a significant portion of the boundary layer (up to $z/\delta \approx 0.65$). Such a variation of U_b within the boundary layer is consistent with the findings for incompressible and lower-Mach-number supersonic flows (Duan *et al.*, 2014; Kim and Hussain, 1993). In the free stream, the propagation speed departs from Taylor's hypothesis and is significantly lower than the local mean velocity.

Figure 18 shows the wall-normal distribution of the correlation coefficient γ_p that provides a figure of merit for the frozen-wave approximation. The pressure wave is nearly frozen with $\gamma \approx 1$ within the boundary layer and becomes less so outside the boundary layer at both Mach numbers. As the Mach number increases, propagation effects become significantly more dominant over evolution effects for the free-stream pressure wave.

Figure 19 compares the bulk propagation speed at the wall and in the free stream with some existing experiments and simulations. Symbols: *squares*: Kistler and Chen (1963); *deltas*: Bernardini and Pirozzoli (2011); *left triangles*: Laufer (1964); *diamonds*: Kendall (1970); *D*: Kim (1989); *filled circles*: DNS Mach 5.86; *right triangles*: DNS Mach 5.86; *circles*: DNS Mach 5.86; *A*: DNS Mach 2.5 (Duan *et al.*, 2014); *B*: DNS Mach 2.5; *C*: DNS Mach 2.5; *Lines*: $M_r = 1$. $U_{b1} : \frac{\partial C_{pp}(r_x,0,\Delta t)}{\partial r_x}|_{r_x=\Delta x} = 0$, $U_{b2} : \frac{\partial C_{pp}(\Delta x,0,r_t)}{\partial r_t}|_{r_t=\Delta t} = 0$. $U_{b3} : -\frac{\overline{(\partial p/\partial t)(\partial p/\partial x)}}{\overline{(\partial p/\partial x)^2}}$. In Figure 19, U_{b1} is defined based on the space-time correlation coefficient with Equation 6 for the time delay Δt or frequency ($\omega = 2\pi/\Delta t$) where the pre-multiplied frequency spectrum (Figure 10a) attains its maximum. In analogy, U_{b2} is derived based on Equation 7 for the streamwise separation Δx or wavenumber ($k_1 = 2\pi/\Delta x$) where the pre-multiplied one-dimensional wavenumber spectrum attains its maximum. U_{b3} is computed using Equation 8 by assuming 'frozen wave/eddy'. The values of bulk propagation speed U_b varies depending on specific definitions. Similar findings were reported for the convection speed of the wall pressure (Choi and Moin, 1990). The value of U_b at the wall gradually increases with the free-stream Mach number and is slightly higher than those widely quoted for low-speed flows (Choi and Moin, 1990; Tsuji *et al.*, 2007; Willmarth, 1975). The gradual increase in propagation speeds with Mach number is consistent with the values reported by Bernardini and Pirozzoli (2011) for turbulent boundary layers at Mach 2, 3 and 4 (Figure 19a). In the free stream, the bulk propagation speed is approximately equal to $0.7U_\infty$. Such a free-stream propagation speed falls within the region where $M_r > 1$, with $M_r \equiv (U_\infty - U_b)/a_\infty$, consistent with the concept of 'eddy Mach wave' ra-
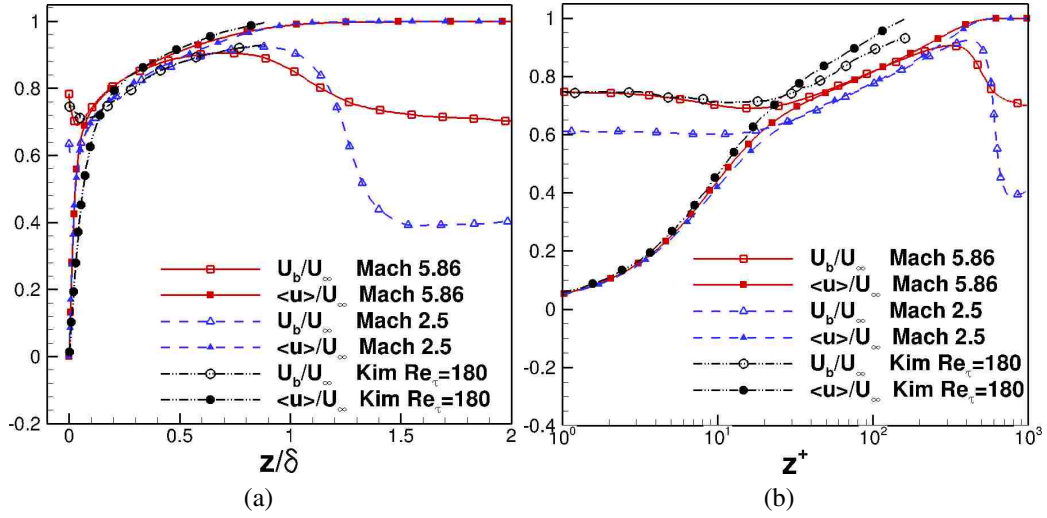
Figure 17. Wall-normal distribution of bulk propagation speed of pressure fluctuations in (a) outer and (b) inner units.

diation (Ffowcs-Williams and Maidanik, 1965; Phillips, 1960). Figure 19b further shows that the DNS-computed propagation speed compares well with existing experiments and simulations (Duan *et al.*, 2014; Laufer, 1964).

4. FREE-STREAM ACOUSTIC RADIATION

4.1. CHARACTERISTICS OF FREESTREAM FLUCTUATIONS

In this section, the nature of free-stream acoustic fluctuations is analyzed using the present DNS data at Mach 5.86 and compared with previous results at Mach 2.5 Duan *et al.* (2014).

Table 4 lists the free-stream values of several fluctuating flow variables for the present DNS at Mach 5.86 and the Mach 2.5 DNS (Duan *et al.*, 2014). R is the gas constant in the ideal-gas equation of state $p = \rho RT$. Similar to the Mach 2.5 case, the free-stream thermodynamic fluctuations for the present Mach 5.86 case satisfy isentropic relations, indicating the acoustic nature of free-stream fluctuations. Moreover, the level of dilata-
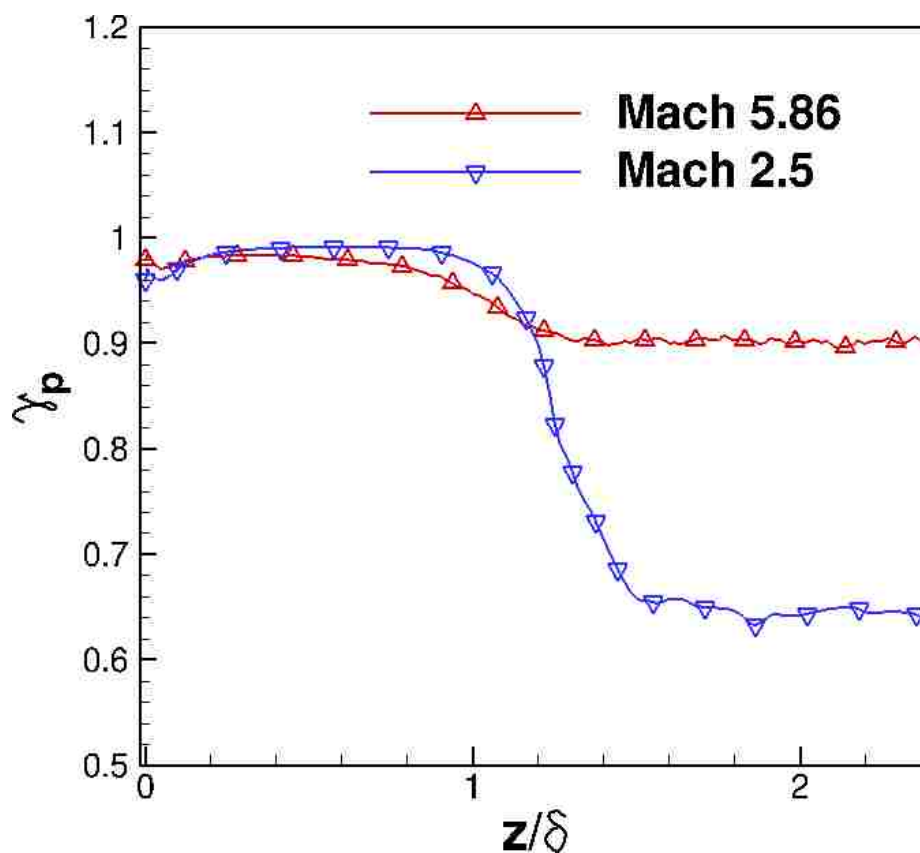
Figure 18. The distribution of correlation coefficient $\gamma_p = \dfrac{|\overline{(\partial p/\partial x)(\partial p/\partial t)}|}{\left[\overline{(\partial p/\partial t)^2}\ \overline{(\partial p/\partial x)^2}\right]^{1/2}}$ that provides a figure of merit for the frozen-wave approximation.

(a) Wall
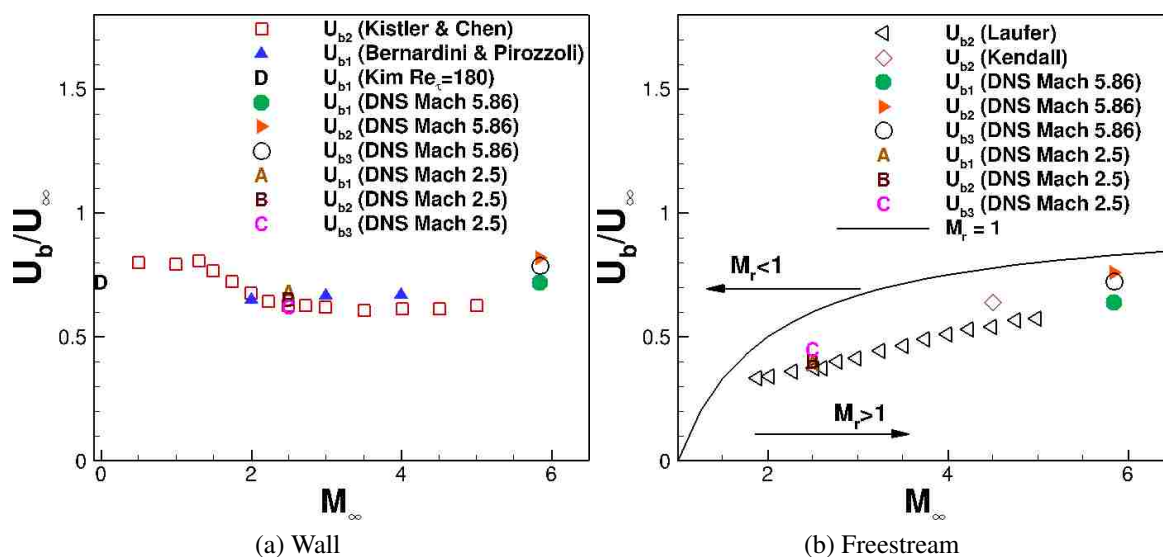
(b) Freestream

Figure 19. Bulk convection speed of pressure fluctuations as a function of free-stream Mach number.

tional fluctuations $\overline{(\partial u_i/\partial x_i)'^2}$, which is representative of the acoustic mode, is compared with the magnitude of vortical fluctuations $\overline{\Omega_i'\Omega_i'}$, which is representative of vorticity mode. The large values of $\overline{(\partial u_i/\partial x_i)'^2}/\overline{\Omega_i'\Omega_i'}$ as well as the small values of entropy fluctuations s'_{rms}/R relative to $p'_{rms}/\bar{p}$ imply that the acoustic mode is dominant over the vorticity and entropy modes in the free stream in terms of modal compositions (Kovasznay, 1953). The dominance of the acoustic mode over the other two modes confirms that a purely acoustic field in the free stream is successfully isolated by the present DNS. Thus, the present simulation provides a unique opportunity for studying the similarities and differences in the characteristics of the primarily vortical fluctuations within the boundary layer and acoustic fluctuations in the free stream.

The normalized velocity fluctuations at Mach 5.86 are significantly larger than those at Mach 2.5. Yet, the r.m.s. fluctuations in either velocity component are less than approximately 0.25%. The fluctuations in thermodynamic variables are stronger than the velocity fluctuations and also increase from Mach 2.5 to Mach 5.86. At Mach 5.86, the r.m.s. pressure fluctuations are approximately 2% of the mean pressure value, compared with $\overline{p'_{rms}}/\bar{p} \approx 0.4\%$ at Mach 2.5. The increase in fluctuating intensity with the Mach number is consistent with the theory of 'Mach wave radiation' and the experimental findings by Laufer (1964). For both Mach number cases, the pressure fluctuations are strongly correlated with the streamwise velocity (u) and the wall-normal velocity (w), but almost uncorrelated with the spanwise velocity (v). The large negative value of $\overline{u'p'}$ and positive value of $\overline{w'p'}$ indicate that the free-stream radiation may be approximated by two-dimensional, backward-facing waves. The changes in values of $\overline{w'p'}/w'_{rms}p'_{rms}$ and $\overline{u'p'}/u'_{rms}p'_{rms}$ between the Mach 2.5 and Mach 5.86 cases indicate a variation of the directionality of the free-stream radiation with the Mach number (see Section 4.2).

Table 4. The disturbance field at $z/\delta = 2.63$ for Case Mach 5.86 and $z/\delta = 2.8$ for Case Mach 2.5.

	Mach 5.86	Mach 2.5
$u'_{rms}/\overline{u}$	1.3633×10^{-3}	8.3217×10^{-4}
$v'_{rms}/\overline{u}$	1.0514×10^{-3}	4.9146×10^{-4}
$w'_{rms}/\overline{u}$	2.0526×10^{-3}	9.1447×10^{-4}
$p'_{rms}/\overline{p}$	2.0498×10^{-2}	3.9143×10^{-3}
$\rho'_{rms}/\overline{\rho}$	1.4621×10^{-2}	2.7967×10^{-3}
$T'_{rms}/\overline{T}$	5.8908×10^{-3}	1.1180×10^{-3}
$(\rho u)'_{rms}/\overline{\rho u}$	1.3754×10^{-2}	2.2742×10^{-3}
$T'_{t,rms}/\overline{T}_t$	1.9813×10^{-3}	6.5962×10^{-4}
$p'_{t,rms}/\overline{p}_t$	6.6867×10^{-3}	2.3330×10^{-3}
$\overline{(\partial u_i/\partial x_i)'^2}/\overline{\Omega'_i \Omega'_i}$	31580	6099
s'_{rms}/R	2.1149×10^{-3}	1.1765×10^{-4}
$\overline{u'p'}/u'_{rms}p'_{rms}$	-0.6528	-0.7197
$\overline{v'p'}/v'_{rms}p'_{rms}$	-0.00639	-0.0059
$\overline{w'p'}/w'_{rms}p'_{rms}$	0.9250	0.7765
$\overline{\rho'p'}/\rho'_{rms}p'_{rms}$	1	1
$\overline{T'p'}/T'_{rms}p'_{rms}$	1	1

4.2. WAVE-FRONT ORIENTATION

In this section, the directionality of the stochastic acoustic field in the free stream is discussed given its importance to hypersonic transition testing in conventional wind tunnels. Figure 20a shows that the instantaneous pressure field in the free stream consists of randomly spaced wavefronts, each with a limited spatial coherence. The wave fronts exhibit a preferred orientation within the streamwise-wall normal (x-z) plane. The orientation of the instantaneous free-stream pressure field is similar to that of the free-stream pressure structures that are defined in the statistical sense based on $C_{pp}(\Delta x, z, z_{ref})$ (Figure 13d) with $\theta \approx \theta_{xz} = 21°$.

An alternative way of defining the free-stream wave-front orientation is to assume that the two-dimensional free-stream acoustic field consists of planar acoustic waves. The wave-front orientation can therefore be derived using the following plane-acoustic-wave
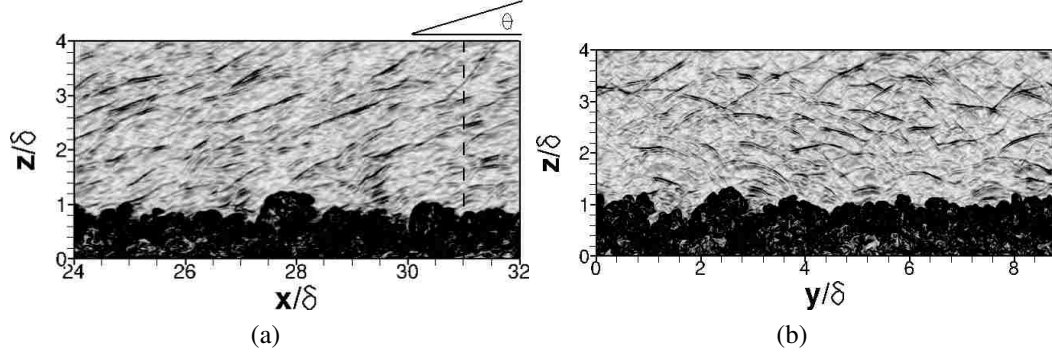
Figure 20. Numerical Schlieren image based on instantaneous flow field for the present DNS of a Mach 5.86 turbulent boundary layer.

relation (Liepmann and Roshko, 1957)

$$\frac{u'_n}{U_\infty} = \frac{1}{\gamma M_\infty} \frac{p'}{p_\infty} \tag{10}$$

where $u'_n = \mathbf{u}' \cdot \mathbf{n} = u' \cos \theta_n + w' \sin \theta_n$ is the velocity normal to the wave front and $\mathbf{n} = (\cos \theta_n, \sin \theta_n)$ is the plane-wave normal direction with θ_n the angle between $\mathbf{u}$ and $\mathbf{n}$. The wave-front orientation that is statistically most likely can be determined to be the direction that minimizes the difference between $u'_{n,rms}/U_\infty$ and $p'_{rms}/(\gamma M_\infty p_\infty)$. By using the free-stream statistics analogous to Table 4, $\theta_n \approx 120°$ (correspondingly $\theta \approx 30°$) is obtained. For comparison, the wave angle of acoustic radiation for a Mach 2.5 turbulent boundary layer is $\theta = 42°$ (Duan *et al.*, 2014). Laufer (1964) has used a similar but less rigorous relation $u'_n \cos \theta_n = u'$ to estimate the wave-orientation, since the streamwise velocity fluctuation u' is the only velocity component that could be measured in his experiments.

The differences in the calculated wave angles θ based on the plane-acoustic-wave assumption and the two-point correlation $C_{pp}(\Delta x, z, z_{ref})$ indicate that the the free-stream acoustic field does not correspond to truly planar waves. The deviation from purely planar behavior is also indicated by the imperfect correlation between p' and the streamwise (u') and wall-normal (w')velocity fluctuations in the free-stream region (recall the data presented in Table 4). As seen from Figure 20b, a substantial portion of the instantaneous

pressure field within the region of interest corresponds to conical disturbances propagating from some (possibly virtual) localized source within the boundary layer. The finite spanwise extent of the pressure wavepackets is consistent with the finite size of acoustic sources that are responsible for generating the waves. The details of the acoustic sources will be discussed in Section 4.3.

4.3. SOURCES OF FREESTREAM ACOUATIC RADIATION

In this section, the acoustic sources that give rise to the acoustic pressure fluctuations in the free stream are approximated in terms of flow turbulence according to the acoustic analogy approach by Phillips (1960). The Phillips' form of the acoustic analogy equation, the definition of acoustic source terms as well as their decomposition into linear and quadratic components are given in Duan *et al.* (2014).

Figure 21a plots the root mean square (r.m.s.) of the acoustic source term including both linear and nonlinear components as functions of z across the near-wall portion of the boundary layer. The rms of the source terms are normalized by $\left(\frac{\delta^2}{U_\infty^2}\right)$. Similar to the Mach 2.5 case (Duan *et al.*, 2014), the total source term for the present DNS peaks at $z^+ \approx 20$ and the nonlinear source term is dominant over the linear source term throughout the boundary layer. Among the six constituent terms of the nonlinear acoustic source (Figure 21b), $(\partial v'/\partial z)(\partial w'/\partial y)$ has the largest r.m.s. value, with approximately the same peak location as the total acoustic source. The dominance of $(\partial v'/\partial z)(\partial w'/\partial y)$ in the buffer layer may indicate the important role played by the near-wall streamwise structures in sound generation. Similar distribution of source terms as well as the dominance of the nonlinear components have been reported by Kim (1989) in the context of incompressible flows.

We note that the magnitude of the source terms is not the sole determinant of the local contribution to the acoustic radiation in the free stream. The solution to the acoustic analogy equation is given by the convolution of the source terms with the Green's function of this equation, which may be viewed as the local efficiency of the conversion of
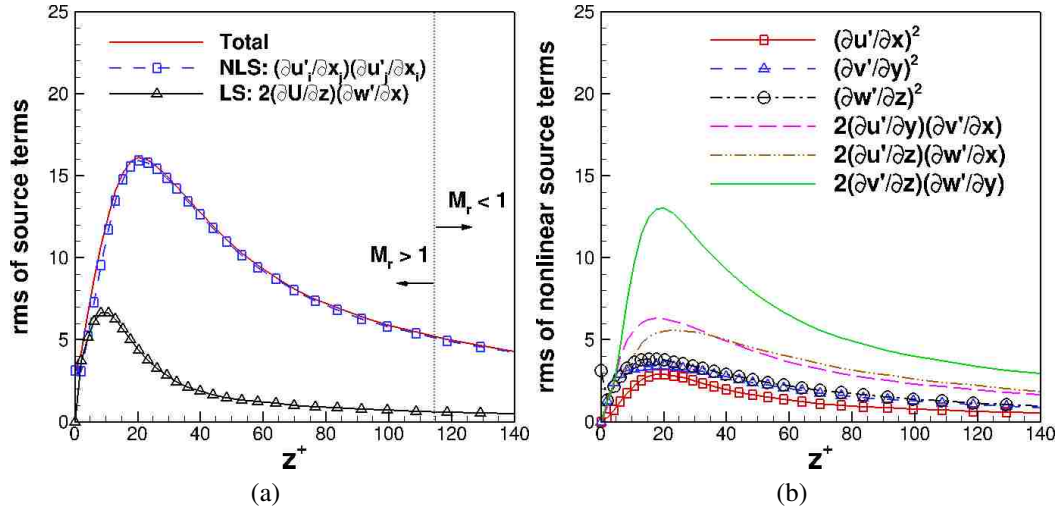
Figure 21. Profiles of the rms source terms (including the total, nonlinear source (NLS), and linear source (LS) terms) across the near-wall portion of the boundary layer.

hydrodynamic source terms into radiating acoustic disturbances. Due to the dramatic differences in the ability of sound generation between turbulent sources that travel at subsonic or supersonic speeds relative to the frees tream (i.e. the basic concept of 'eddy Mach wave' (Ffowcs-Williams and Maidanik, 1965; Phillips, 1960)), Figure 21a also shows the regions of flow with a supersonic ($M_r > 1$) and subsonic ($M_r < 1$) relative Mach number. The relative sonic location ($M_r = 1$) for the Mach 5.86 lies at $z^+ \approx 114$ ($z/\delta \approx 0.25$), compared with $z^+ \approx 22$ ($z/\delta \approx 0.04$) for the Mach 2.5 case, indicating a dramatic increase in the fraction of sound-radiating eddies as the free-stream Mach number increases. The increased portion of sound-generating eddies is consistent with the enhanced radiation intensity as the free-stream Mach number increases (Figure 8b). Moreover, the increased fraction of the inner layer that can radiate to the free stream contributes to a reduced gap between the peak frequency of fluctuations near the surface and within the free stream, as shown by Figure 10b.

5. SUMMARY AND CONCLUSIONS

DNS of a zero-pressure-gradient turbulent boundary layer with a nominal free-stream Mach number of 5.86 and a wall-to-recovery temperature ratio of $T_w/T_r = 0.76$ is conducted to investigate the wall-normal variation of the fluctuating pressure field and highlight the differences between the primarily vortical pressure signal within the boundary layer and the acoustic pressure signal in the free stream. Computational predictions for both the mean velocity profile and frequency spectrum of surface pressure fluctuations compare well with measurements in a Mach 6 wind tunnel facility, providing what we believe is the first ever comparison of this type at hypersonic Mach numbers. The spectrum peak of pressure signals shifts to lower frequencies as the location of interest moves away from the wall. Compared with the pressure signal within the boundary layer, the free-stream acoustic pressure fluctuations exhibit a significantly lower dominant frequency, a greater spatial extent, a smaller structure angle, and a smaller bulk propagation speed. Within the boundary layer (except in the immediate vicinity of the wall), Taylor's hypothesis approximately holds with pressure waves propagating with the local mean velocity. In the free stream, however, the propagation speed of pressure fluctuations is significantly smaller than the free-stream velocity, even though the 'frozen-eddy' assumption approximately holds as indicated by the value of $\gamma_p \approx 1$ (Figure 18). There is an apparent match in the Lagrangian time and spatial scales between the free-stream pressure structures and the structures near the wall. Given that the free-stream acoustic radiation is generated by turbulent fluctuations within the boundary layer, the apparent match in Lagrangian scales indicates that the acoustic sources are located near the wall. The source terms identified from the standpoint of an acoustic analogy (Phillips, 1960) are shown to be located mostly in the buffer layer and dominated by terms that are quadratic in fluctuating velocities. The numerical findings on the acoustic sources are consistent with the theory of 'Mach wave radiation'.

The DNS results are also compared with the recently reported Mach 2.5 DNS (Duan *et al.*, 2014) to highlight the variation of acoustic characteristics with Mach number. It is found that the Mach 5.86 DNS exhibits increased radiation intensity, enhanced energy content at high frequencies, shallower orientation of wave fronts with respect to the flow direction, and larger convection velocity relative to the Mach 2.5 case. These variations in the free-stream pressure field with Mach number agree well with the experimentally measured trends (Laufer, 1964) and are consistent with the 'Mach wave radiation' concept (Ffowcs-Williams and Maidanik, 1965; Phillips, 1960).

ACKNOWLEDGEMENTS

REFERENCES

Beresh, S. J., Henfling, J. F., Spillers, R. W., and Pruett, B. O. M., 'Fluctuating wall pressures measured beneath a supersonic turbulent boundary layer,' Physics of Fluids, 2011, **23**(075110).

Bernardini, M. and Pirozzoli, S., 'Wall pressure fluctuations beneath supersonic turbulent boundary layers,' Physics of Fluids, 2011, **23**(085102).

Bernardini, M., Pirozzoli, S., and Grasso, F., 'The wall pressure signature of transonic shock/boundary layer interaction,' Journal of Fluid Mechanics, 2011, **671**, pp. 288–312.

Bies, D. W., 'A review of flight and wind tunnel measurements of boundary layer pressure fluctuations and induced structure reponse,' Technical report, NASA CR-626, 1966.

Blake, W. K., *Mechanics of Flow-Induced Sound and Vibration*, Academic Press, Orlando, Florida, 1986.

Bookey, P., Wyckham, C., Smits, A. J., and Martin, M. P., 'New experimental data of stbli at dns/les accessible reynolds numbers,' AIAA Paper 2005-309, 2005.

Bounitch, A., Lewis, D. R., and Lafety, J. F., 'Experimental study of second-mode instabilities on a 7-degree cone at Mach 6,' in 'AIAA Paper 2011-1200,' 2011 .

Bradshaw, P., 'Inactive motion and pressure fluctuations in turbulent boundary layers,' Journal of Fluid Mechanics, 1967, **30**, pp. 241–258.

Bull, M. K., 'Wall-pressure fluctuations beneath turbulent boundary layers: Some reflection on forty years of research,' Journal of Sound and Vibration, 1996, **190**(3), pp. 299–315.

Cadot, O., Douady, S., and Couder, Y., 'Characterization of the low-pressure filaments in a three-dimensional turbulent shear flow,' Physics of Fluids, 1995, **7**, pp. 630–646.

Casper, K. M., 'Turbulent pressure fluctuations in a hypersonic boundary layer,' 2011, aAE 626 Final Project Report, Purdue University, West Lafayette, IN, USA, 2011.

Choi, H. and Moin, P., 'On the space-time characteristics of wall-pressure fluctuations,' Physics of Fluids, 1990, **2**(8), pp. 1450–1460.

Del Alamo, J. C. and Jimenez, J., 'Estimation of turbulent convection velocities and corrections to taylor's approximation,' Journal of Fluid Mechanics, 2009, **640**, pp. 5–26.

Dolling, D. S. and Dussauge, J. P., 'A survey of measurements and measuring techniques in rapidly distorted compressible turbulent boundary layers,' AGARDograph, 1989, **315**, pp. 1–18.

Donaldson, J. and Coulter, S., 'A review of free-stream flow fluctuation and steady-state flow quality measurements in the AEDC/VKF supersonic tunnel A and hypersonic tunnel B,' AIAA Paper 95-6137, 1995.

Duan, L., Beekman, I., and Martín, M. P., 'Direct numerical simulation of hypersonic turbulent boundary layers. part 2: Effect of wall temperature,' Journal of Fluid Mechanics, 2010, **655**, pp. 419–445.

Duan, L., Beekman, I., and Martín, M. P., 'Direct numerical simulation of hypersonic turbulent boundary layers. part 3: Effect of Mach number,' Journal of Fluid Mechanics, 2011, **672**, pp. 245–267.

Duan, L., Choudhari, M. M., and Wu, M., 'Numerical study of pressure fluctuations due to a supersonic turbulent boundary layer,' Journal of Fluid Mechanics, 2014, **746**, pp. 165–192.

Duan, L. and Martín, M. P., 'Direct numerical simulation of hypersonic turbulent boundary layers. part 4: Effect of high enthalpy,' Journal of Fluid Mechanics, 2011, **684**, pp. 25–59.

Eléna, M. and Lacharme, J. P., 'Experimental study of a supersonic turbulent boundary layer using a laser doppler anemometer,' Journal de Mécanique Théorique et Appliquée, 1988, **7**, pp. 175–190.

Ffowcs-Williams, J. E. and Maidanik, G., 'The Mach wave field radiated by supersonic turbulent shear flows,' Journal of Fluid Mechanics, 1965, **21**, pp. 641–657.

Ganapathisubramani, B., Clemens, N., Hambleton, W. T., Longmire, E. K., and Marusic, I., 'Investigation of large-scale coherence in a turbulent boundary layer uisng two-point correlations,' Journal of Fluid Mechanics, 2005, **524**, pp. 57–80.

Ganapathisubramani, B., Clemens, N. T., and Dolling, D. S., 'Large-scale motions in a supersonic turbulent boundary layer,' Journal of Fluid Mechanics, 2006, **556**, pp. 271–282.

Gloerfelt, X. and Berland, J., 'Turbulent boundary-layer noise: Direct radiation at mach number 0.5,' Journal of Fluid Mechanics, 2013, **723**, pp. 318–351.

Guarini, S. E., Moser, R. D., Shariff, K., and Wray, A., 'Direct numerical simulation of a supersonic turbulent boundary layer at Mach 2.5,' Journal of Fluid Mechanics, 2000, **414**, pp. 1–33.

Harris, J. and Blanchard, D., 'Computer program for solving laminar, transitional, or turbulent compressible boundary-layer equations for two-dimensional and axisymmetric flow,' NASA-TM-83207, 1982.

Jiang, G. S. and Shu, C. W., 'Efficient implementation of weighted ENO schemes,' Journal of Computational Physics, 1996, **126**(1), pp. 202–228.

Kat, R. D. and Oudheusden, B. W. V., 'Instantaneous planar pressure determination from PIV in turbulent flows,' Experiments in Fluids, 2012, **52**(5), pp. 1089–1106.

Kendall, J. M., 'Supersonic boundary layer transition studies,' Space Program Summary, 1970, **3**, pp. 43–47.

Kida, S. and Miura, H., 'Identification and analysis of vortical structures,' European Journal of Mechanics - B/Fluids, 1998, **17**(4), pp. 471–488.

Kim, J., 'On the structure of pressure fluctuations in simulated turbulent channel flow,' Journal of Fluid Mechanics, 1989, **205**, pp. 421–451.

Kim, J. and Hussain, F., 'Propagation velocity of perturbations in turbulent channel flow,' Physics of Fluids, 1993, **5**(3), pp. 695–706.

Kim, K. C. and Adrian, R. J., 'Very large-scale motion in the outer layer,' Physics of Fluids, 1999, **11**, pp. 417–422.

Kistler, A. L. and Chen, W. S., 'The fluctuating pressure field in a supersonic turbulent boundary layer,' Journal of Fluid Mechanics, 1963, **16**, pp. 41–64.

Kovasznay, L. S. G., 'Turbulence in supersonic flow,' Journal of Aeronautical Sciences, 1953, **20**, pp. 657–674.

Laufer, J., 'Some statistical properties of the pressure field radiated by a turbulent boundary layer,' Physics of Fluids, 1964, **7**(8), pp. 1191–1197.

Liepmann, H. W. and Roshko, A., *Elements of Gasdynamics*, John Wiley & Sons, Inc. New York, 1957.

Maestrello, L., 'Radiation from and panel response to a supersonic turbulent boundary layer,' Journal of Sound Vibration, 1969, **10**(2), pp. 261–262.

Marco, A. D., Camussi, R., Bernardini, M., and Pirozzoli, S., 'Wall pressure coherence in supersonic turbulent boundary layers,' Journal of Fluid Mechanics, 2013, **732**, pp. 445–456.

Martín, M., 'DNS of hypersonic turbulent boundary layers. part i: Initialization and comparison with experiments,' Journal of Fluid Mechanics, 2007, **570**, pp. 347–364.

Masutti, M., Chazot, E., and Carbonaro, M., 'Disturbance level characterization of a hypersonic blowdown facility,' AIAA Journal, 2012, **50**(12).

Morgan, B., Larsson, J., Kawai, S., and Lele, S. K., 'Improving low-frequency characteristics of recycling/rescaling inflow turbulence generation,' AIAA Journal, 2011, **49**(3), pp. 582–597.

Naka, Y., Stanislas, M., Foucaut, J. M., Coudert, S., Laval, J. P., and Obi, S., 'Space-time pressure-velocity correlations in a turbulent boundary layer,' Journal of Fluid Mechanics, 2015, **771**, pp. 624–675.

Pate, S. R., 'Dominance of radiated aerodynamic noise on boundary-layer transition in supersonic-hypersonic wind tunnels,' Technical Report AEDC-TR-77-107, Arnold Engineering Development Center, 1978.

Peltier, S. J., Humble, R. A., and Bowersox, R. D. W., 'PIV of a mach 5 turbulent boundary layer over diamond roughness elements,' AIAA Paper 2012-3061, 2012.

Phillips, O. M., 'On the generation of sound by supersonic turbulent shear layers,' Journal of Fluid Mechanics, 1960, **9**, pp. 1–28.

Piponniau, S., Dussauge, J. P., Debieve, J. F., and Dupont, P., 'A simple model for low-frequency unsteadiness in shock-induced separation,' Journal of Fluid Mechanics, 2009, **629**, pp. 87–108.

Pirozzoli, S. and Bernardini, M., 'Turbulence in supersonic boundary layers at moderate Reynolds numbers,' Journal of Fluid Mechanics, 2011, **688**, pp. 120–168.

Priebe, S. and Martín, M. P., 'Low-frequency unsteadiness in shock wave-turbulent boundary layer interaction,' Journal of Fluid Mechanics, 2012, **699**, pp. 1–49.

Schlatter, P. and Örlü, R., 'Assessment of direct numerical simulation data of turbulent boundary layers,' Journal of Fluid Mechanics, 2010, **659**, pp. 116–126.

Schneider, S. P., 'Effects of high-speed tunnel noise on laminar-turbulent transition,' Journal of Spacecraft and Rockets, 2001, **38**(3), pp. 323–333.

Schneider, S. P., 'Development of hypersonic quiet tunnels,' Journal of Spacecraft and Rockets, 2008, **45**(4), pp. 641–664.

Simens, M. P., Jimenez, J., Hoyas, S., and Mizuno, Y., 'A high-resolution code for turbulent boundary layers,' Journal of Computational Physics, 2009, **228**(11), pp. 4218–4231.

Smits, A. J. and Dussauge, J. P., *Turbulent Shear Layers in Supersonic Flow*, American Institute of Physics, 2 edition, 2006.

Spalart, P. R., 'Direct simulation of a turbulent boundary layer up to $re_\theta = 1410$,' Journal of Fluid Mechanics, 1988, **187**, pp. 61–98.

Stainback, P. C., 'Hypersonic boundary-layer transition in the presence of wind tunnel noise,' AIAA Journal, 1971, **9**(12), pp. 2475–2476.

Steen, L. E., *Characterization and Development of Nozzles for a Hypersonic Quiet Wind Tunnel*, Master's thesis, Purdue University, West Lafayette, IN, USA, 2010.

Taylor, E. M., Wu, M., and Martín, M. P., 'Optimization of nonlinear error sources for weighted non-oscillatory methods in direct numerical simulations of compressible turbulence,' Journal of Computational Physics, 2006, **223**(1), pp. 384–397.

Thompson, K. W., 'Time dependent boundary conditions for hyperbolic systems,' Journal of Computational Physics, 1987, **68**(1), pp. 1–24.

Tomkins, C. D. and Adrian, R. J., 'Spanwise structure and scale growth in turbulent boundary layers,' Journal of Fluid Mechanics, 2003, **490**, pp. 37–74.

Tsuji, Y., Fransson, J. H. M., Alferdsson, P. H., and Johansson, A. V., 'Pressure statistics and their scaling in high-reynolds-number turbulent boundary layers,' Journal of Fluid Mechanics, 2007, **585**, pp. 1–40.

Tsuji, Y., Imayama, S., Schlatter, P., Alfredsson, P. H., Johansson, A. V., Marusic, I., Hutchins, N., and Monty, J., 'Pressure fluctuation in high-reynolds-number turbulent boundary layer: Results from experiments and dns,' Journal of Turbulence, 2012, **13**(50), pp. 1–19.

Welch, P. D., 'The use of fast fourier transform for the estimation of power spectra: A method based on time averaging over short, modified periodograms,' IEEE Trans. Audio Electroacoustics, 1967, **AU-15**, pp. 70–73.

Williamson, J., 'Low-storage runge-kutta schemes,' Journal of Computational Physics, 1980, **35**(1), pp. 48–56.

Willmarth, W. W., 'Wall pressure fluctuations beneath turbulent boundary layers,' Annual Review of Fluid Mechanics, 1975, **7**, pp. 13–36.

Wu, M. and Martín, M. P., 'Direct numerical simulation of supersonic boundary layer over a compression ramp,' AIAA Journal, 2007, **45**(4), pp. 879–889.

Wu, M. and Martín, M. P., 'Analysis of shock motion in shockwave and turbulent boundary layer interaction using direct numerical simulation data,' Journal of Fluid Mechanics, 2008, **594**, pp. 71–83.

Xu, S. and Martín, M. P., 'Assessment of inflow boundary conditions for compressible turbulent boundary layers,' Physics of Fluids, 2004, **16**(7), pp. 2623–2639.

II. EFFECT OF WALL COOLING ON BOUNDARY-LAYER-INDUCED PRESSURE FLUCTUATIONS AT MACH 6

CHAO ZHANG[1], LIAN DUAN[1] and MEELAN M. CHOUDHARI[2]

[1]Missouri University of Science and Technology, Rolla, MO 65401, USA

[2]NASA Langley Research Center, Hampton, VA 23681, USA

ABSTRACT

Direct numerical simulations of turbulent boundary layers with nominal freestream Mach number of 6 and Reynolds number of $Re_\tau \approx 450$ are conducted at a wall-to-recovery temperature ratio of $T_w/T_r = 0.25$ and compared with a previous database for $T_w/T_r = 0.76$ in order to investigate pressure fluctuations and their dependence on wall temperature. The wall-temperature dependence of widely used velocity and temperature scaling laws for high-speed turbulent boundary layers is consistent with previous studies. The near-wall pressure fluctuation intensities are dramatically modified by wall temperature conditions. At different wall temperatures, the variation of pressure fluctuation intensities as a function of wall-normal distance is dramatically modified in the near-wall region but remains almost intact away from the wall. Wall cooling also has a strong effect on the frequency spectrum of wall pressure fluctuations, resulting in a higher dominant frequency and a sharper spectrum peak with a faster roll-off at both the high- and low-frequency ends. The effect of wall cooling on the freestream noise spectrum can be largely accounted for by the associated changes in boundary-layer velocity and length scales. The pressure structures within the boundary layer and in the free stream evolve less rapidly as the wall temperature decreases, resulting in an increase in the decorrelation length of coherent pressure structures for the colder wall case. The pressure structures propagate with similar speeds for both wall temperatures. Due to wall cooling, the generated pressure disturbances undergo less refraction

before they are radiated to the free stream, resulting in a slightly steeper radiation wave front in the free stream. Acoustic sources are largely concentrated in the near-wall region; wall cooling most significantly influences the nonlinear (slow) component of the acoustic source term by enhancing dilatational fluctuations in the viscous sublayer while damping vortical fluctuations in the buffer and log layers.

Keywords: high-speed flow, turbulence simulation, turbulent boundary layers

1. INTRODUCTION

An understanding of the physics of pressure fluctuations induced by high-speed turbulent boundary layers is important to the structural design of hypersonic vehicles and to the testing and evaluation of hypersonic vehicles in noisy hypersonic facilities. The fluctuating surface pressure on vehicle surfaces is responsible for vibrational load and may lead to damaging effects such as flutter. The freestream pressure fluctuations radiated from the turbulent boundary layer on the nozzle wall of conventional hypersonic wind tunnels give rise to tunnel noise that has first-order impact on laminar-turbulent transition in the tunnel. Given that the surface temperatures of hypersonic flight vehicles are typically significantly lower than the adiabatic wall temperature and that practical hypersonic facilities for testing and evaluating hypersonic vehicles are designed to have a non-adiabatic turbulent boundary layer on the nozzle wall, it is of practical importance to investigate wall-temperature effects on hypersonic turbulent boundary layers and their induced pressure fluctuations.

To date, there is limited literature on the effects of wall cooling on high-speed turbulent boundary layers. Most of the available measurements are restricted to basic turbulence quantities, such as the skin friction and Stanton number, and the mean and root mean square (r.m.s.) fluctuations of velocity and temperature (Fernholz and Finley, 1980; Smits and Dussauge, 2006). Existing numerical studies are largely focused on the effect of wall cooling on the distribution and scaling of velocity fluctuations and the relationships between temperature and velocity fields at a Mach number of 5 or less (Chu *et al.*, 2013;

Duan *et al.*, 2010; Hadjadj *et al.*, 2015; Maeder, 2000; Shadloo *et al.*, 2015; Shahab *et al.*, 2011; Trettel and Larsson, 2016; Zhang *et al.*, 2014). For example, Duan *et al.* (2010) performed direct numerical simulations (DNS) of turbulent boundary layers at Mach 5 over a broad range of wall-to-recovery temperature ratios ($T_w/T_r = 0.18$-1.0) and focused on assessing the validity of Morkonvin's hypothesis in the high-Mach number cold-wall regime. Zhang *et al.* (2014) studied the coupling between the thermal and velocity fields of compressible wall-bounded turbulent flows and introduced a generalized Reynolds analogy that explicitly accounts for finite wall heat flux for cold-wall boundary layers. Shadloo *et al.* (2015) and Hadjadj *et al.* (2015) conducted detailed analyses of the effect of wall temperature on the statistical behavior of turbulent boundary layers at Mach 2. Bowersox (2009) and Poggie (2015) studied the modeling of turbulent energy flux in adiabatic and cold-wall turbulent boundary layers. Trettel and Larsson (2016) introduced a new mean velocity scaling for compressible wall turbulence with heat transfer; this new scaling achieved excellent collapse of the mean velocity profile at different Reynolds numbers, Mach numbers, and rates of wall heat transfer.

As far as the boundary-layer-induced pressure fluctuations are concerned, the body of available data is even more scarce. Experimental measurements consist largely of those at the wall using surface-mounted pressure transducers (Beresh *et al.*, 2011; Fernholz *et al.*, 1989; Kistler and Chen, 1963). Previous DNS studies of pressure fluctuations induced by high-speed turbulent boundary layers have focused on boundary layers with adiabatic or nearly adiabatic walls (Bernardini and Pirozzoli, 2011; Di Marco *et al.*, 2013; Duan *et al.*, 2014, 2016). To the best of the knowledge of the authors, no existing studies have been conducted in the high-Mach-number cold-wall regime that provide the off-wall fluctuating pressure field including the freestream acoustic pressure fluctuations. As a result, a comprehensive understanding of the freestream disturbance field and its dependence on boundary-layer parameters (e.g. free-stream Mach number, wall temperature and Reynolds number) is still lacking. The objective of the current paper is to investigate the dependence

of boundary-layer-induced pressure fluctuations on wall temperature for hypersonic Mach numbers. In a previous paper by the present authors (Duan *et al.*, 2016), the successful application of DNS in capturing the global fluctuating pressure field has been demonstrated for a spatially developing flat plate nominally Mach 6 turbulent boundary layer with a wall-to-recovery temperature ratio of $T_w/T_r = 0.76$. A new DNS dataset at Mach 6 with a different wall temperature ($T_w/T_r = 0.25$) from the previous Mach 6 data (Duan *et al.*, 2016) is introduced for the study of wall-temperature effects. The effect of wall temperature on single- and multi-point statistics of the computed pressure fluctuations at multiple wall normal locations (including the inner layer, the log layer, the outer layer and the free stream) is reported, including the intensity, frequency spectra, space-time correlations and propagation velocities.

The remainder of this paper is structured as follows. The flow conditions selected for numerical simulation and the numerical method used are outlined in Section 2. Section 3 is focused on an analysis of statistical and structural features of pressure fluctuations at multiple wall-normal locations, highlighting their dependence on the wall temperature. The various statistics examined include pressure fluctuation intensities, power spectral densities, two-point pressure correlations, propagation speeds and acoustic sources. Conclusions from the study are presented in Section 5.

2. SIMULATION DETAILS

Direct numerical simulations are performed for zero-pressure-gradient cold-wall turbulent boundary layers with a freestream Mach number of 5.86. Two DNS cases (M6Tw025 and M6Tw076) with the same freestream conditions but different wall temperatures are examined, with the M6Tw076 case corresponding to the previous simulation by Duan *et al.* (2016). Table 1 outlines the freestream conditions for the simulations, including the freestream velocity U_∞, density ρ_∞, and temperature T_∞. The working fluid is assumed to be a perfect gas. The freestream condition is representative of that at the nozzle exit

of the Purdue Mach 6 Quiet Tunnel (BAM6QT) under noisy operations (Schneider, 2001; Steen, 2010). Table 2 lists the values of the mean boundary-layer parameters at the selected downstream location (x_a) for statistical analysis, including the momentum thickness θ, shape factor $H = \delta^*/\theta$ (where δ^* denotes the local displacement thickness), boundary layer thickness δ, friction velocity $u_\tau = \sqrt{\tau_w/\bar{\rho}_w}$, viscous length $z_\tau = \mu_w/\rho_w u_\tau$, and different definition of Reynolds number, where $Re_\theta \equiv \rho_\infty U_\infty \theta/\mu_\infty$, $Re_\tau \equiv \rho_w u_\tau \delta/\mu_w$, and $Re_{\delta_2} \equiv \rho_\infty U_\infty \theta/\mu_w$. Throughout this paper, subscripts ∞ and w will be used respectively to denote quantities in the free stream and at the wall. The viscosity μ is calculated using the Sutherland's Law $\mu = C_1 T^{3/2}/(T + C_2)$, with constants $C_1 = 1.458 \times 10^{-6}$ and $C_2 = 110.4$. The wall temperature T_w for Case M6Tw076 is similar to that at the nozzle wall of BAM6QT, corresponding to a wall temperature ratio of $T_w/T_r \approx 0.76$, with the recovery temperature estimated as $T_r = T_\infty \left(1 + r(\gamma - 1)M_\infty^2/2\right)$ based on a recovery factor of $r = 0.89$. Case M6Tw025 has the same freestream conditions and Reynolds number, Re_τ, as Case M6Tw076 but a lower wall temperature ($T_w/T_r \approx 0.25$) that is more likely to be encountered at high altitude flight. Thus, by comparing the results of Cases M6Tw025 and M6Tw076, the effect of wall cooling on the pressure fluctuations can be investigated at a fixed Reynolds number Re_τ.

Wall cooling causes a change in both the boundary layer thickness and the fluid properties across the boundary layer. Experiments and numerical data suggest that a single Reynolds number is not sufficient to characterize the flow (Lele, 1994; Smits, 1991). However, what definition for Reynolds number is "correct" to assess the effects of wall cooling is still an open question and the choice for that definition mainly depends on researcher preference and the research objective (Shadloo *et al.*, 2015). For instance, out of the few existing DNS studies on the effect of wall temperature, Lagha *et al.* (2011), Maeder (2000), and Shadloo *et al.* (2015) have chosen to match Re_τ for reporting their data; Duan *et al.* (2010) and Chu *et al.* (2013) have chosen to match $Re_{\delta 2}$; Shahab *et al.* (2011) have chosen to match Re_θ. In addition, Shadloo *et al.* (2015) compared the effect of choosing the

different definitions of Reynolds number (Re_τ, $Re_{\delta 2}$, Re_θ) on the turbulence statistics and showed that Re_τ performs best in collapsing the first and second order statistical moments for boundary layers with different wall heat transfers. In the current study, we have chosen to match Re_τ based partially on the findings of Shadloo *et al.* (2015). This selection of Reynolds number is also due to our decisions for grid resolutions and the limited extent of computational domain.

Table 1. Freestream conditions for Mach 6 DNS of turbulent boundary layers.

M_∞	U_∞(m/s)	ρ_∞(kg/m^3)	T_∞(K)
5.86	869.1	0.0443	55.0

Table 2. Boundary layer properties at the station (x_a) selected for the analysis of the pressure field ($x_a = 88.6\delta_i$ for Case M6Tw025 and $x_a = 54.1\delta_i$ for Case M6Tw076, with δ_i the boundary layer thickness at the domain inlet). Part 1.

Case	$T_w(K)$	T_w/T_r	θ(mm)	H	δ(mm)	$z_\tau(\mu m)$	u_τ(m/s)	δ_i(mm)
M6Tw025	97.5	0.25	0.199	8.4	3.6	8.0	33.8	1.33
M6Tw076	300	0.76	0.948	13.6	23.8	52.6	45.1	13.8

Table 3. Boundary layer properties at the station (x_a) selected for the analysis of the pressure field ($x_a = 88.6\delta_i$ for Case M6Tw025 and $x_a = 54.1\delta_i$ for Case M6Tw076, with δ_i the boundary layer thickness at the domain inlet). Part 2.

Case	$T_w(K)$	T_w/T_r	Re_θ	Re_τ	$Re_{\delta 2}$
M6Tw025	97.5	0.25	2121	450	1135
M6Tw076	300	0.76	9455	453	1746

The details of the DNS methodology, including numerical methods, initial and boundary conditions, have been documented in our previous papers (Duan *et al.*, 2014, 2016). The DNS methodology has been extensively validated against experiments and ex-
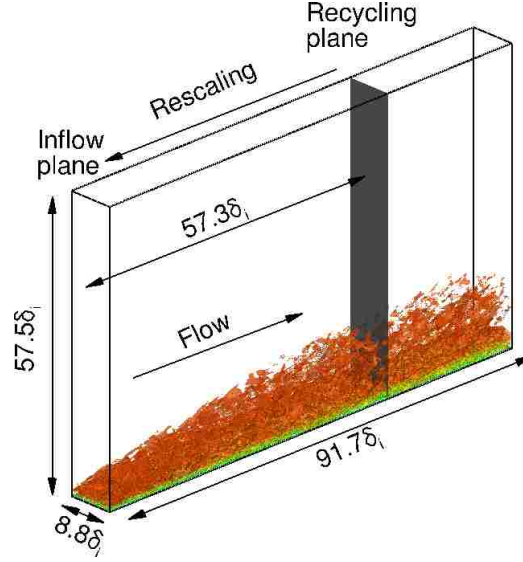
Figure 1. Computational domain and simulation setup for the DNS case M6Tw025.

isting numerical simulations for capturing boundary-layer-induced pressure fluctuations at supersonic/hypersonic speeds (Duan *et al.*, 2014, 2016). In particular, computational predictions for the mean-velocity profiles and surface pressure spectrum are in good agreement with experimental measurements for Case M6Tw076 (Duan *et al.*, 2016).

Figure 1 shows the computational setup for Case M6Tw025, which parallels that of Case M6Tw076 documented in Duan *et al.* (2016). The reference length δ_i is the thickness of the boundary layer (based on 99% of the freestream velocity) at the inlet plane. An instantaneous flow is shown in the domain, visualized by iso-surface of the magnitude of density gradient, $|\nabla\rho|\delta_i/\rho_\infty = 0.98$, colored by the streamwise velocity component (with levels from 0 to U_∞, blue to red). x, y, and z are, the streamwise, spanwise, and wall-normal coordinates, respectively. The computational domain size and grid resolution are determined based on the lessons learned from Duan *et al.* (2014, 2016) as summarized in Table 4. Viscous length scale $z_\tau = 8.0$ μm corresponds to at $x_a/\delta_i = 88.6$. Δz_{min}^+ and Δz_{max}^+ are the minimum and maximum wall-normal grid spacing for $0 \leq z/\delta_i \leq 8$; $\delta_i = 1.33$ mm. The streamwise length L_x is adjusted to assure that the turbulence fluctuations are uncorrelated and minimal spurious correlation can be introduced due to the

Table 4.   Grid resolution and domain size for Case M6Tw025. L_x, L_y and L_z are the domain size in the streamwise, spanwise and wall-normal directions, respectively.

$N_x \times N_y \times N_z$	L_x/δ_i	L_y/δ_i	L_z/δ_i	Δx^+	Δy^+	Δz^+_{min}	Δz^+_{max}
$2400 \times 400 \times 560$	91.7	8.8	57.5	6.42	3.72	0.46	4.75

inflow turbulence generation. The streamwise domain size is also large enough so that the freestream acoustic field has gone through the transient adjustment due to recycled inflow and has re-established equilibrium at the downstream location selected for statistical analysis ($x_a = 88.6\delta_i$). It can be shown that the pressure fluctuations both at the wall and in the free stream for Case M6Tw025 have become homogeneous in the streamwise direction after $x/\delta_i \approx 60$. Uniform grid spacings are used in the streamwise and spanwise directions. The grids in the wall-normal direction are clustered in the boundary layer with $\Delta z^+ = 0.46$ at the wall, and kept uniform with $\Delta z^+ \approx 5$ in the freestream until up to approximately $8\delta_i$ or 3.3δ, where δ_i and δ represent the mean boundary layer thickness based on $\bar{u}/U_\infty = 0.99$ at the inflow boundary and at the selected downstream location x_a, respectively. For the selected grid resolution, the wavelength of the highest-frequency spectral components of freestream pressure fluctuations (corresponding to $\omega\delta^*/U_\infty \approx 15$ as shown in Section 4.2) is discretized with at least nine points in the streamwise direction and twelve points in the wall-normal direction.

In the following sections, averages are first calculated over a streamwise window ($[x_a-0.5\delta_i, x_a+0.5\delta_i]$ with $x_a = 88.6\delta_i$ for Case M6Tw025 and $[x_a-0.9\delta_i, x_a+0.9\delta_i]$ with $x_a = 54.1$ for Case M6Tw076) and the spanwise direction for each instantaneous flow field; then, an ensemble average over 312 flow-field snapshots (corresponding to $\delta_i/U_\infty \approx 1016$ or $\delta/u_\tau \approx 14.6$) and over 153 flow-field snapshots (corresponding to $\delta_i/U_\infty \approx 240$ or $\delta/u_\tau \approx 7.2$) is calculated for Case M6Tw025 and Case M6Tw076, respectively. A smaller number of flow-field snapshots was sufficient for Case M6Tw076 because of the larger spanwise domain size ($L_y/\delta_i = 15.7$) for this case compared with that for Case M6Tw025

(L_y/δ_i = 8.8). The effect of spanwise domain size on flow statistics is monitored by comparing Case M6Tw076 with an auxiliary simulation of the same grid resolution but with a narrower span of L_y/δ_i = 6.26, and negligible difference is observed in flow statistics of interest. The outflow boundary condition has no influence on boundary-layer profiles within the selected streamwsie window over which averages are calculated. Statistical convergence for both cases is verified by calculating averages over varying streamwise window sizes or over different number of snapshots and by making sure that the differences in flow statistics are negligible ($<$ 1%) among the different data-averaging techniques. Data for freestream acoustic radiation was not sampled at the same value of z/δ for the two cases. Therefore, comparison of statistical and spectral characteristics will be made between predictions at z/δ = 2.36 (i.e. z_∞ = 2.36δ) for Case M6Tw025 and z/δ = 2.63 (i.e. z_∞ = 2.63δ) for Case M6Tw076. Throughout the paper, standard (Reynolds) averages are denoted by an overbar, $\overline{f}$ and fluctuations around standard averages are denoted by single prime as $f' = f - \overline{f}$. Negligible differences have been found between the standard and the density-weighted (Favre) averages for the statistics reported in the article.

3. ASSESSMENT OF DNS DATA

In this section, the first and second moment statistics of the velocity and temperature fields are reported at the selected downstream location (x_a). The data is compared with published data, especially those of turbulent boundary layers in the hypersonic, cold-wall regime.

Figure 2a plots the van Driest transformed mean velocity u_{VD}^+, which is defined as

$$u_{VD}^+ = \frac{1}{u_\tau} \int_0^{\overline{u}} (\overline{\rho}/\overline{\rho}_w)^{1/2} \, d\overline{u}. \tag{1}$$

The mean velocity shows an approximately logarithmic region where $u_{VD}^+ = \frac{1}{k} \log (z^+) + C$ upon van Driest transformation. Symbols: △ (green): Duan *et al.* (2010) M5T1, $M_\infty = 5$, $Re_\tau = 798$, $T_w/T_r = 0.18$. ▼: Duan *et al.* (2010) M5T2, $M_\infty = 5$, $Re_\tau = 386$, $T_w/T_r = 1.0$. ◄: Modesti and Pirozzoli (2016), $M_\infty = 1.9$, $Re_\tau = 448$, $T_w/T_r = 0.24$. ◇ (violet red): Wu *et al.* (2016), $M_\infty = 4.5$, $Re_\tau = 2200$, $T_w/T_r = 0.22$. ○: Shadloo *et al.* (2015), $M_\infty = 2$, $Re_\tau = 507$, $T_w/T_r = 0.5$. Consistent with the published data by Duan *et al.* (2010); Modesti and Pirozzoli (2016); Shadloo *et al.* (2015); Wu *et al.* (2016), the van Driest transformed mean velocity shows a shrinking of the linear viscous sublayer with higher wall cooling, while the additive constant C in the log law does not seem to be significantly affected. Figure 2b shows a significantly better collapse of data in both the viscous sublayer and the log layer among the computational datasets involving different wall-cooling rates, after the mean velocity and the wall-normal coordinate are transformed according to the proposal by Trettel and Larsson (2016) as

$$u_{TL}^+ = \int_0^{u^+} \left(\frac{\bar{\rho}}{\rho_w}\right)^{1/2} \left[1 + \frac{1}{2}\frac{1}{\bar{\rho}}\frac{d\bar{\rho}}{dz}z - \frac{1}{\bar{\mu}}\frac{d\bar{\mu}}{dz}z\right] du^+, \qquad z^* = \frac{\bar{\rho}(\tau_w/\bar{\rho})^{1/2}z}{\bar{\mu}} \qquad (2)$$

Figure 3 plots the streamwise turbulence intensity and the Reynolds shear stress. Symbols: —— (red): M6Tw025, $M_\infty = 5.86$, $Re_\tau = 450$, $T_w/T_r = 0.25$. –·–·– (blue): M6Tw076, $M_\infty = 5.86$, $Re_\tau = 453$, $T_w/T_r = 0.76$. –––: Duan *et al.* (2010), $M_\infty = 5$, $Re_\tau = 798$, $T_w/T_r = 0.18$. –··–··–: Duan *et al.* (2010), $M_\infty = 5$, $Re_\tau = 386$, $T_w/T_r = 1.0$. □: Shadloo *et al.* (2015), $M_\infty = 2$, $Re_\tau = 507$, $T_w/T_r = 0.5$. △ (violet red): Schlatter and Örlü (2010), $M_\infty \approx 0$, $Re_\tau = 500$. ●: Peltier *et al.* (2016) $M_\infty = 4.9$, $Re_\tau = 1100$, $T_w/T_r = 0.9$. A significantly improved collapse of data is achieved by Morkovin's scaling (Morkovin, 1962), which takes into account the variation in mean flow properties. Morkovin's scaling brings the magnitudes of the extrema in the compressible cases closer to the incompressible results of Schlatter and Örlü (2010). The better collapse of data between Cases M6Tw025 and M6Tw076 in Figure 3b indicate that the effect of wall cooling
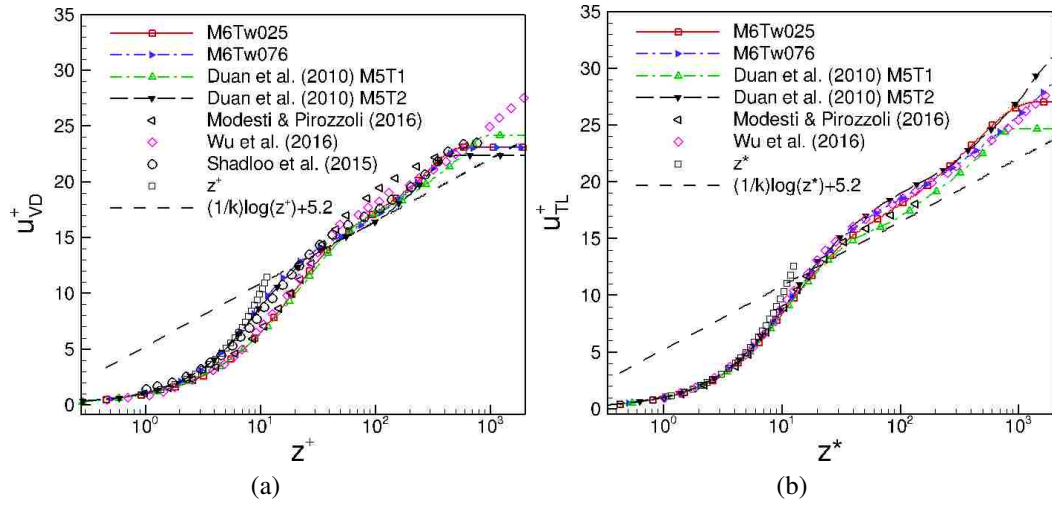
Figure 2. Mean velocity profiles transformed according to (a) van Driest and (b) Trettel and Larsson (2016).

on fluctuating velocity intensities can be largely accounted for by Morkovin's scaling. Similarly improved collapse of data is achieved by Morkovin's scaling for turbulence intensities in the spanwise and wall-normal directions.
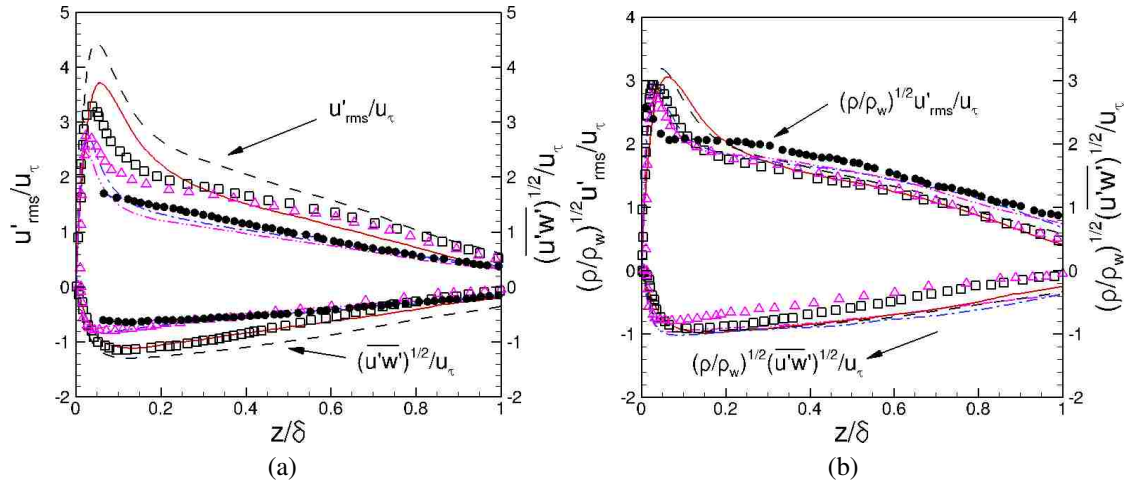
Figure 3. Distribution of r.m.s. velocity components as function of wall-normal distance.

As far as the coupling between thermal and velocity fields is concerned, Figures 4 and 5 plots several temperature-velocity scalings for high-speed turbulent boundary layers, including the mean temperature-velocity relation, the turbulent heat flux $\overline{\rho w'T'}$, the tur-

bulent Prandtl number $Pr_t \equiv \left(\overline{\rho u' w'}(\partial \overline{T}/\partial z) \right) / \left(\overline{\rho w' T'}(\partial \overline{u}/\partial z) \right)$, and the modified strong Reynolds analogies (SRA) of Huang *et al.* (1995) and Zhang *et al.* (2014). −−−: Duan *et al.* (2010), $M_\infty = 5$, $Re_\tau = 798$, $T_w/T_r = 0.18$. − · · − · · −: Duan *et al.* (2010), $M_\infty = 5$, $Re_\tau = 386$, $T_w/T_r = 1.0$. ○: Shadloo *et al.* (2015), $M_\infty = 2$, $Re_\tau = 507$, $T_w/T_r = 0.5$. The present spatial DNS at Mach 6 are generally consistent with the predictions from several previous studies at lower Mach numbers (Duan *et al.*, 2010; Shadloo *et al.*, 2015; Zhang *et al.*, 2014) in regard to the wall-temperature dependence of the temperature-velocity scalings.

In particular, Figure 4a shows that strong wall cooling causes a deviation of DNS from the Walz's relation (Walz, 1969) that is commonly used to relate the mean temperature and velocity as

$$\frac{\overline{T}}{T_\infty} = \frac{T_w}{T_\infty} + \frac{T_r - T_w}{T_\infty} \left(\frac{\overline{u}}{U_\infty} \right) + \frac{T_\infty - T_r}{T_\infty} \left(\frac{\overline{u}}{U_\infty} \right)^2 . \tag{3}$$

A significantly improved comparison for the cold-wall case (Case M6Tw025) is achieved by using the generalized Reynolds analogy of Zhang *et al.* (2014) in which a general recovery factor r_g is introduced and T_r in Equation 3 is accordingly replaced by T_{rg} as

$$\frac{\overline{T}}{T_\infty} = \frac{T_w}{T_\infty} + \frac{T_{rg} - T_w}{T_\infty} \left(\frac{\overline{u}}{U_\infty} \right) + \frac{T_\infty - T_{rg}}{T_\infty} \left(\frac{\overline{u}}{U_\infty} \right)^2 , \tag{4}$$

where $T_{rg} = T_\infty + r_g U_\infty^2/(2C_p)$, $r_g = 2C_p(T_w - T_\infty)/U_\infty^2 - 2Pr q_w/(U_\infty \tau_w)$ with Pr being the molecular Prandtl number and C_p the heat capacity at constant pressure. Equation 4 explicitly accounts for the wall heat flux q_w and it coincides with Walz's relation in the case of adiabatic walls.

Figure 4b shows that the DNS-predicted turbulent heat flux $\overline{\rho w' T'}$ compares well with the prediction of the theoretical model by Bowersox (2009), consistent with the finding by Poggie (2015). The DNS-predicted turbulent Prandtl number compares well with the computations of Shadloo *et al.* (2015) and shows a singular behavior near the wall where the correlation $\overline{w' T'}$ is zero (Figure 12a). The SRA relates the temperature fluctuations T'_{rms}

Figure 4. The coupling between thermal and velocity fields. Part 1.

to the streamwise velocity fluctuations u'_{rms} as given by

$$\frac{T'_{rms}/\overline{T}}{(\gamma-1)M^2(u'_{rms}/\overline{u})} = \frac{1}{a(1-(\partial\overline{T}_t/\partial\overline{T}))}.$$ (5)

where $a = Pr_t$ in Huang's modified SRA (Huang *et al.*, 1995) and $a = \overline{Pr_t} \equiv Pr_t(1 + \overline{w}\,\overline{\rho'u'}/\overline{\rho u'w'})/(1+\overline{w}\,\overline{\rho'T'}/\overline{\rho w'T'})$ in Zhang's version of modified SRA (Zhang *et al.*, 2014), and $M = \overline{u}/\sqrt{\gamma R\overline{T}}$ is the local Mach number. Figure 5b shows that the modified SRA of Zhang *et al.* (2014) gives a slightly improved prediction between u'_{rms} and T'_{rms} than that of Huang *et al.* (1995).

4. BOUNDARY-LAYER-INDUCED PRESSURE FLUCTUATIONS

In this section, the statistical and spectral characteristics of pressure fluctuations induced by hypersonic cold-wall turbulent boundary layers are discussed, highlighting their dependence on the wall temperature. The pressure statistics analyzed include the fluctuation intensity, frequency power spectral density, space-time correlations, and propagation
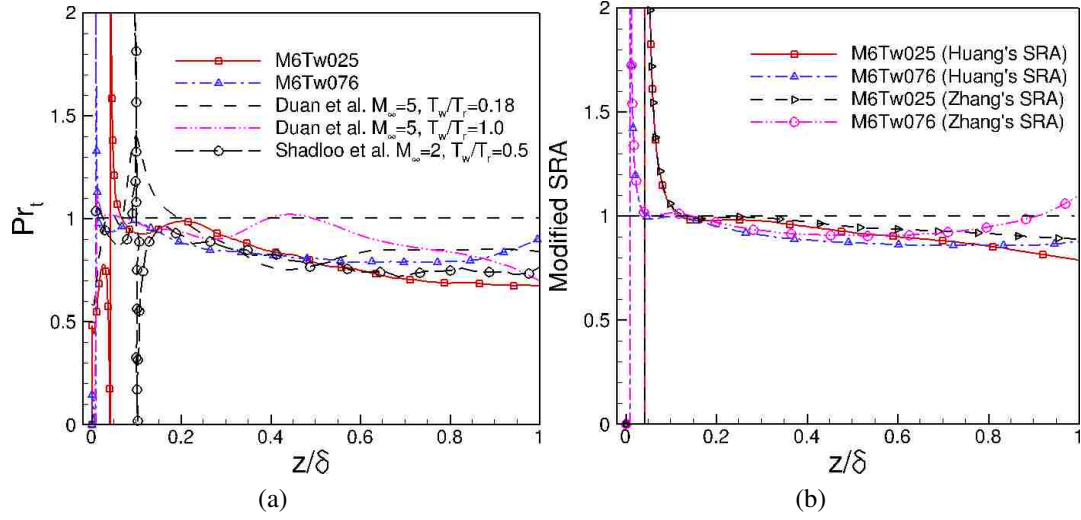
Figure 5. The coupling between thermal and velocity fields. Part 2.

speed. The frequency spectrum of the pressure fluctuations is defined as

$$\Phi_p(\omega, x, z) = \frac{1}{2\pi} \int_{-\infty}^{\infty} \overline{p'(x,y,z,t)p'(x,y,z,t+\tau)} e^{-i\omega\tau} d\tau, \qquad (6)$$

where the overbar indicates an average over the local streamwise window, the spanwise (y) direction, and the time (t). Power spectra for Case M6Tw025 are calculated using the Welch method (Welch, 1967) with twelve segments and 50% overlap. A Hanning window is used for weighting the data prior to the fast Fourier transform (FFT) processing. The sampling frequency is approximately 31 U_∞/δ_i (corresponding to 20 MHz), and the length of an individual segment is approximately 156 δ_i/U_∞ for Case M6Tw025. The calculation of power spectra for Case M6Tw076 follows that described in Duan *et al.* (2016). For both cases, the power spectra do not change by changing the window function between Hanning or Hamming windows (at least in the reported frequency ranges) and negligible differences are found when the number of data segments is varied from eight to twelve.

The two-point space-time correlation coefficient of the pressure field is defined as the following equation, where Δx and Δy are spatial separations in the streamwise and spanwise directions, respectively, Δt is the time delay, and z_{ref} is the wall-normal location at which the correlation is computed.

$$C_{pp}(\Delta x, \Delta y, \Delta t, x, z, z_{ref}) = \frac{\overline{p'(x,y,z_{ref},t)p'(x+\Delta x, y+\Delta y, z, t+\Delta t)}}{\left(\overline{p'^2(x,y,z_{ref},t)}\right)^{1/2}\left(\overline{p'^2(x+\Delta x, y+\Delta y, z, t+\Delta t)}\right)^{1/2}}, \quad (7)$$

4.1. R.M.S. OF PRESSURE FLUCTUATIONS

In this section, the wall-normal variation of pressure statistics for the cold-wall hypersonic turbulent boundary layer (Case M6Tw025) is discussed. The results are compared with turbulent boundary layers with an adiabatic or nearly adiabatic wall to highlight the effect of wall cooling.
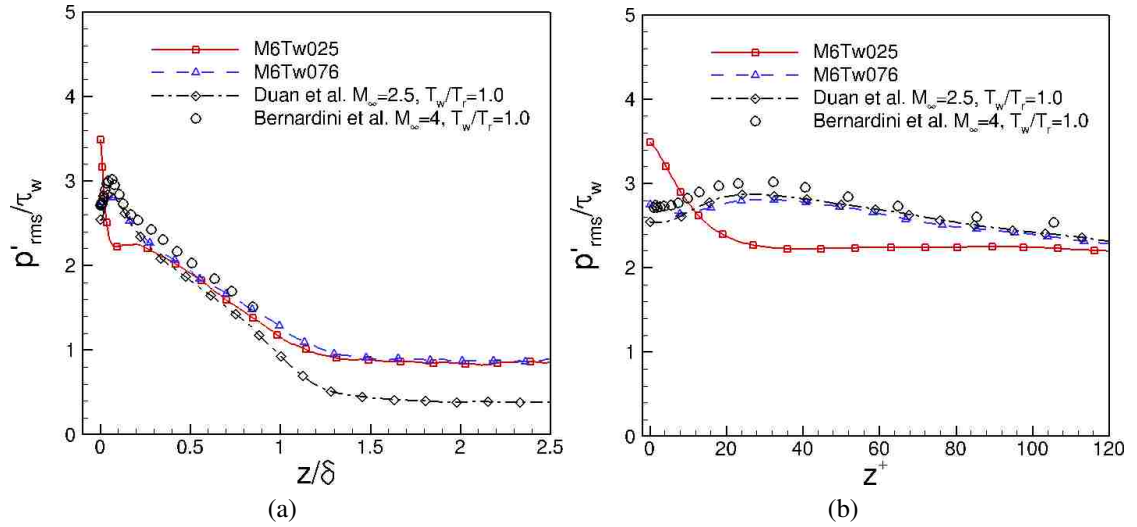
Figure 6. Pressure fluctuation r.m.s. profile p'_{rms} as a function of wall-normal distance normalized by (a, b) the local wall shear stress τ_w.

Figures 6a and 6b show the profiles of r.m.s. of pressure fluctuations p'_{rms} normalized by the local wall shear stress τ_w. Symbols: $\diamond$ Duan *et al.* (2014): $M_\infty = 2.5$, $Re_\tau = 510$, $T_w/T_r = 1.0$. $\circ$: Bernardini and Pirozzoli (2011): $M_\infty = 4$, $Re_\tau = 506$, $T_w/T_r = 1.0$. For Case M6Tw025, p'_{rms}/τ_w undergoes a rapid increase in magnitude as $z \to 0$, with $p'_{rms}/\tau_w \approx 3.5$ at the wall and $p'_{rms}/\tau_w \approx 2.2$ at $z/\delta \approx 0.08$. The magnitude of pressure fluctuation nearly plateaus for $0.08 \lesssim z/\delta \lesssim 0.2$. For Case M6Tw076 and the DNS results of Bernardini and Pirozzoli (2011), however, a similarly rapid increase in the magnitude of pressure fluctuation with respect to τ_w as $z \to 0$ is not observed. Instead, the maximum of p'_{rms}/τ_w is located away from the wall at $z/\delta \approx 0.08$ ($z^+ \approx 25$). The peak of p'_{rms}/τ_w is approximately 20 percent lower in magnitude for Case M6Tw076 as compared to Case M6Tw025. The large difference in p'_{rms}/τ_w close to the wall between the turbulent boundary layer with a cold wall (Case M6Tw025) and those with an adiabatic or nearly adiabatic wall (Case M6Tw076 and that by Bernardini and Pirozzoli (2011)) indicates a strong influence of wall cooling on the pressure fluctuations near the wall. The influence of wall cooling on p'_{rms}/τ_w becomes much weaker in the outer part of the boundary layer ($z/\delta > 0.3$) and nearly vanishes in the free stream. Outside the boundary layer, p'_{rms}/τ_w approaches a constant value of $p'_{rms}/\tau_w \approx 0.9$ for both M6Tw025 and M6Tw076 cases. Figures 6a and 6b show the profiles of r.m.s. pressure fluctuations normalized by the local wall shear stress p'_{rms}/τ_w. Figures 7a and 7b further plot the profiles of r.m.s. of pressure fluctuations p'_{rms} normalized by the local mean (static) pressure $\overline{p}$ and the freestream dynamic pressure $q_\infty = 0.5\rho_\infty U_\infty^2$, respectively. In contrast to the similar values of p'_{rms}/τ_w, significantly different values of $p'_{rms}/\overline{p}$ and p'_{rms}/q_∞ are shown throughout the boundary layer between Cases M6Tw025 and M6Tw076, indicating that the mean shear stress τ_w is a better scaling for p'_{rms} than the mean and dynamic pressures that account for the effect of wall cooling.
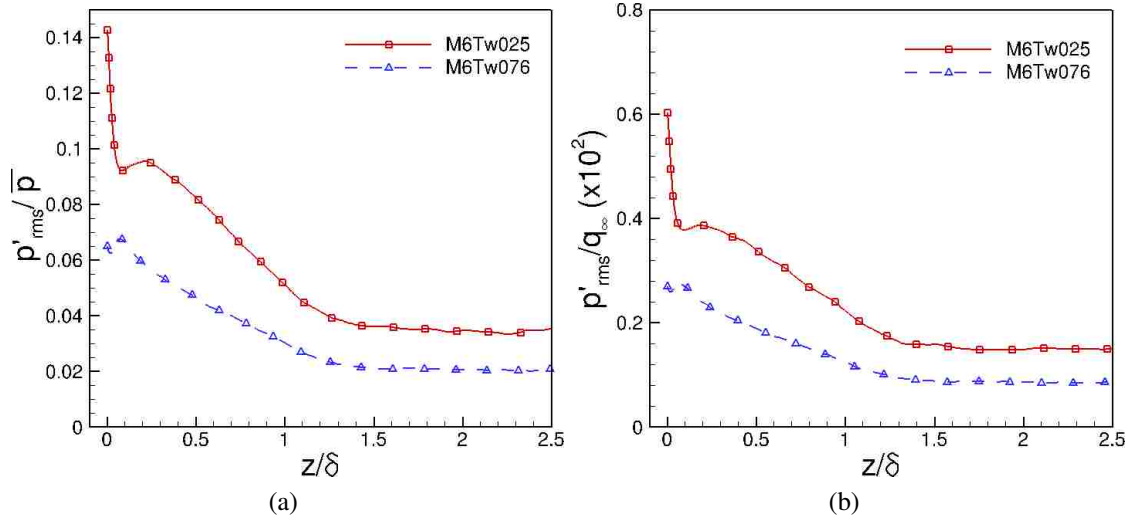
Figure 7. Pressure fluctuation r.m.s. profile p'_{rms} as a function of wall-normal distance normalized by (c) the mean pressure $\overline{p}$, and (d) the dynamic pressure q_∞.

4.2. FREQUENCY SPECTRA OF PRESSURE FLUCTUATIONS

Figures 8 and 9 compares the wall-pressure spectra between Cases M6Tw025 and M6Tw076. The pressure spectrum is normalized so that the area under each curve is equal to unity. The area under each curve is equal to unity. The value of p'_{rms} at the wall is 100.8 Pa for Case M6Tw025 and 44.3 Pa for Case M6Tw076. The spectra are normalized so that the area under each curve is equal to unity. For reference, straight lines with slopes of 2, -1, $-7/3$, and -5 are also included to gauge the rate of spectral roll-off across relatively low, mid, mid-to-high overlap, and high frequencies, respectively, according to Bull (1996).

The wall-pressure spectrum shows a strong wall-temperature dependence, especially in regions of mid frequencies (i.e., $\omega\delta^*/U_\infty > 0.03$ and $\omega\nu/u_\tau^2 < 0.3$) and mid-to-high overlap frequencies (i.e., $0.3 < \omega\nu/u_\tau^2 < 1$), and neither the outer scaling (Figure 8a) nor the inner scaling (Figure 8b) collapse the spectrum between the two DNS cases. Given that the pressure spectrum at mid frequencies is typically attributed to convected turbulence in the logarithmic region and that at mid-to-high overlap frequencies is attributed to eddies in the highest part of the buffer region ($20 < z^+ < 30$) (Bull, 1996), the large
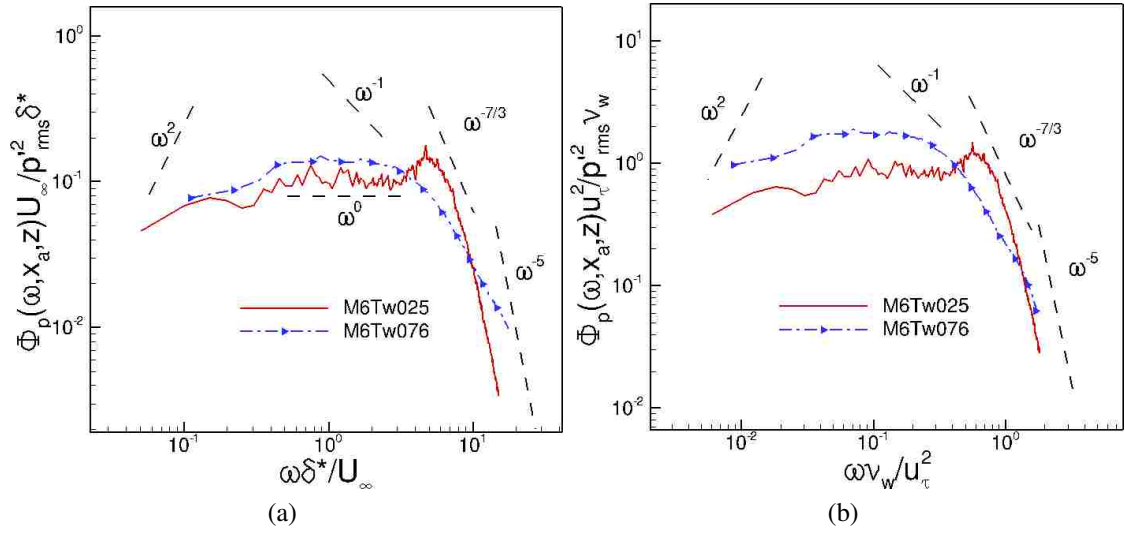
Figure 8. Comparison of pressure spectra at the wall ($z = 0$) between Cases M6Tw025 and M6Tw076.

variation in wall-pressure spectrum at mid and mid-to-high overlap frequencies with wall cooling is consistent with the large changes in eddies in buffer and log layers, as reflected by the differences in r.m.s. pressure values in Figure 6. The deviation from Kolmogorov's $-7/3$ scaling in the overlap region between mid and high frequencies is consistent with the findings by Tsuji *et al.* (2007) and Bernardini *et al.* (2011). At both wall temperatures, the wall pressure spectrum shows a rather weak frequency dependence at lowest computed frequencies and exhibits the ω^{-5} scaling predicted theoretically by Blake (1986) at highest computed frequencies. The pre-multiplied wall-pressure spectrum for Case M6Tw025 (Figures 9a and 9b) consists of a sharper peak with a faster roll-off at both high and low frequencies compared with Case M6Tw076, and wall cooling causes an increase in the dominant frequency from $\omega\delta^*/U_\infty \approx 4$ ($\omega\nu_w/u_\tau^2 = 0.4$ or $f\delta/U_\infty = 1.2$) for Case M6Tw076 to $\omega\delta^*/U_\infty \approx 5$ ($\omega\nu_w/u_\tau^2 = 0.6$ or $f\delta/U_\infty = 1.7$) for Case M6Tw025.

Regarding the freestream pressure spectra, Figure 10a shows that the low-frequency range of the pressure spectra Φ_p is relatively insensitive to T_w/T_r when expressed in outer variables; and Figure 10b shows that the high-frequency portions nearly overlap in inner
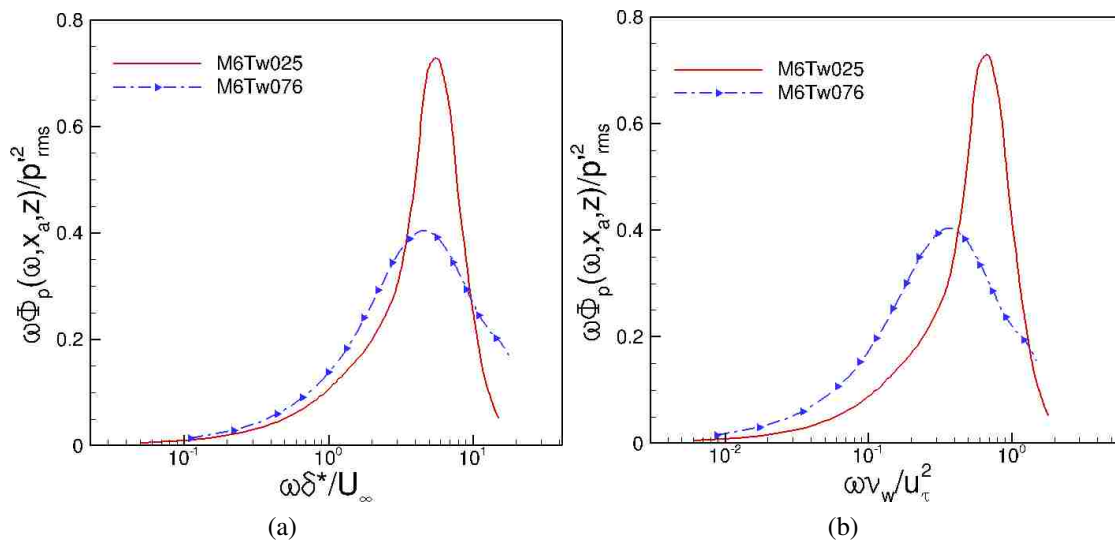
Figure 9. Comparison of pre-multiplited spectrum at the wall ($z = 0$) between Cases M6Tw025 and M6Tw076.

variables, which conforms to the findings of wall-pressure spectrum in low-speed adiabatic flows (Bull, 1996). Moreover, Figures 11a and 11b show that the peak of the pre-multiplied spectrum is centered at a frequency of $\omega\delta^*/U_\infty \approx 1.5$, which is more than three times lower than that of the pressure spectrum at the wall, indicating that the characteristic frequency of acoustic mode is significantly lower than that of the vortical fluctuation close to the surface. The dominant frequency of freestream pressure spectrum is independent of wall temperature, indicating relatively insignificant influence of wall cooling on the freestream pressure spectrum. (The area under each curve is equal to unity. The value of p'_{rms} in the free stream is 24.8 Pa for Case M6Tw025 and 13.9 Pa for Case M6Tw076.)

4.3. SPATIAL CORRELATION OF PRESSURE FLUCTUATIONS

To illustrate the spatial size and orientation of statistically significant three-dimensional (3D) pressure structures, Figure 12 plots the 3D correlation coefficient of the pressure signal $C_{pp}(\Delta x, \Delta y, 0, x_a, z, z_{ref})$ as a function of wall-normal distance. The flow goes from left to right toward positive x direction. Three-dimensional isosurfaces are shown at C_{pp}
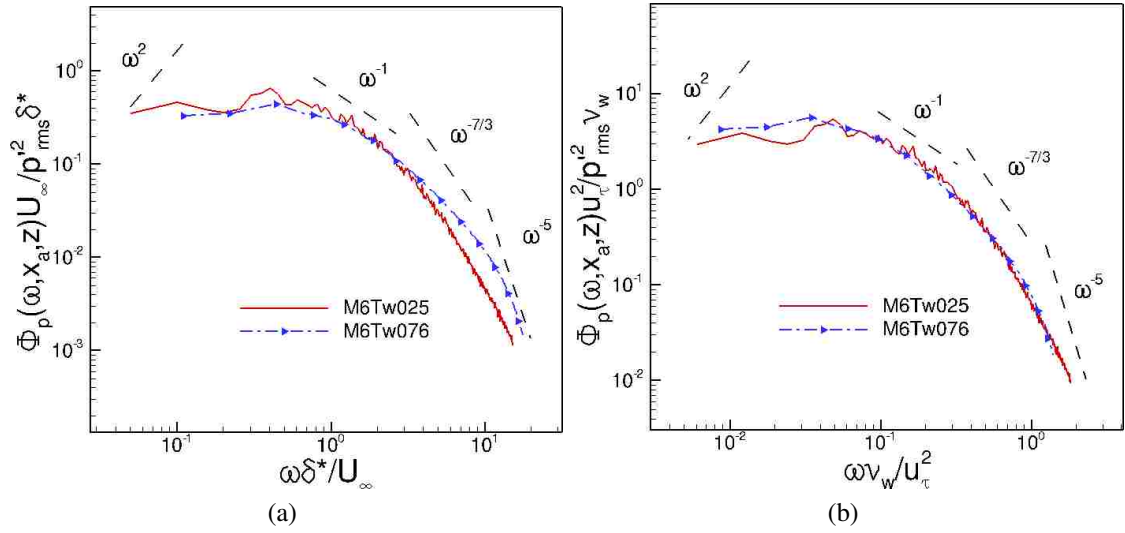
Figure 10. Comparison of pressure spectra in the free stream ($z = z_\infty$) between Cases M6Tw025 and M6Tw076.

= 0.1 (blue) and 0.6 (green). In the horizontal planes going through the correlation origin ($z = z_{ref}$), the contour lines colored white range from 0.1 to 0.9. For each reference height z_{ref}, there exists a downward-leaning pressure structure with finite spatial size and an inclined orientation. The pressure structure has a spatial length scale of order boundary layer thickness $O(\delta)$ in each direction and increases in size as the distance from the wall increases.

The pressure structure is approximately perpendicular to the direction of U_∞ at the wall and becomes increasingly more downward leaning as it moves away from the wall in the inner and outer regions of the boundary layer. In the free stream, the inclination angle with respect to the direction of U_∞ approaches $\theta_{xz} \approx 28°$. The freestream wave-front orientation closely matches the wave front orientation of the instantaneous acoustic radiation visualized by numerical schlieren image, as will be shown in Figure 15. The gray contours are those of numerical schlieren with density gradient contour levels selected to emphasize disturbances in the free stream. The color contours are those of the magnitude of vorticity with contour levels selected to emphasize the large-scale motions within the boundary
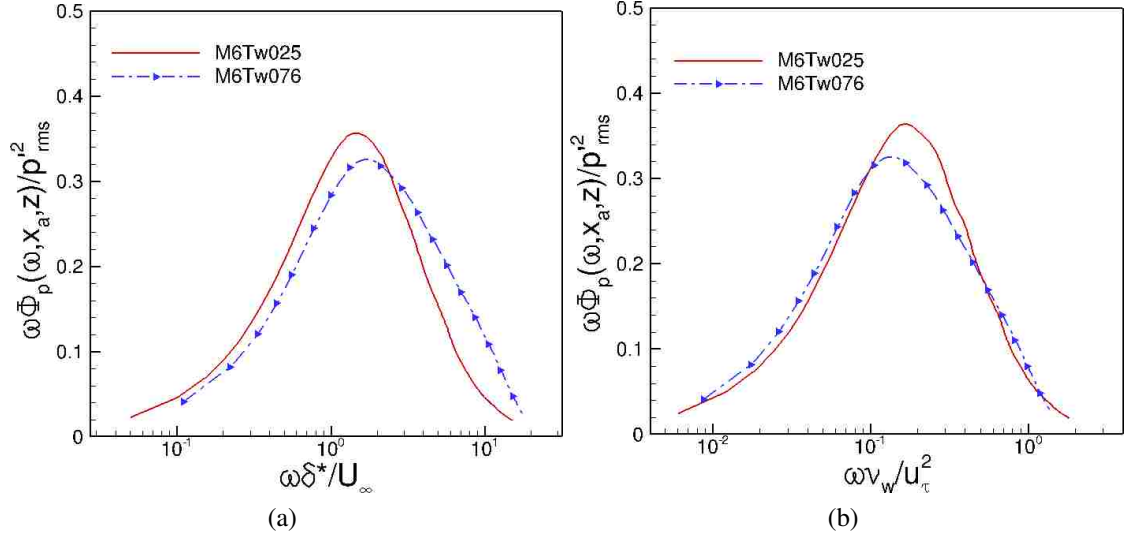
Figure 11. Comparison of pre-multiplited spectrum in the free stream ($z = z_\infty$) between Cases M6Tw025 and M6Tw076.

layer. The angle θ is between the flow direction and the acoustic wave front. Consistent with the spatial correlation in the freestream region (Figure 12d), the 3D visualization in Figure 15 shows the freestream pressure waves deviate from purely planar behavior in the spanwise wall-normal ($y - z$) plane and exhibit a preferred orientation of $\theta \approx 28°$ in the streamwise wall-normal ($x - z$) plane. The finite spanwise extent of the freestream pressure waves is consistent with the finite size of acoustic sources that are responsible for generating the waves. Similar patterns of freestream acoustic radiation are also found for Case M6Tw076 (Duan *et al.*, 2016).

Figure 14 compares the spatial correlation coefficient (with zero spanwise separation $\Delta y = 0$) in the streamwise wall-normal plane between Cases M6Tw025 and M6Tw076. ———: M6Tw025; —·—·—: M6Tw076. Four contour levels are shown: C_{pp}=0.1; 0.2; 0.4; 0.8. At the wall ($z_{ref}/\delta = 0$), the pressure structures have similar inclination angle of $\theta_{xz} \approx 81°$ for both cases. In the free stream, the structure angle for Cases M6Tw025 and M6Tw076 decreases to $\theta_{xz} \approx 28°$ and $\theta_{xz} \approx 21°$, respectively. The change in inclination might indicate that pressure disturbances generated within the boundary layer undergo less

(a) $z_{ref}/\delta = 0$

(b) $z_{ref}/\delta = 0.15$

(c) $z_{ref}/\delta = 0.73$

(d) $z_{ref}/\delta = 2.36$
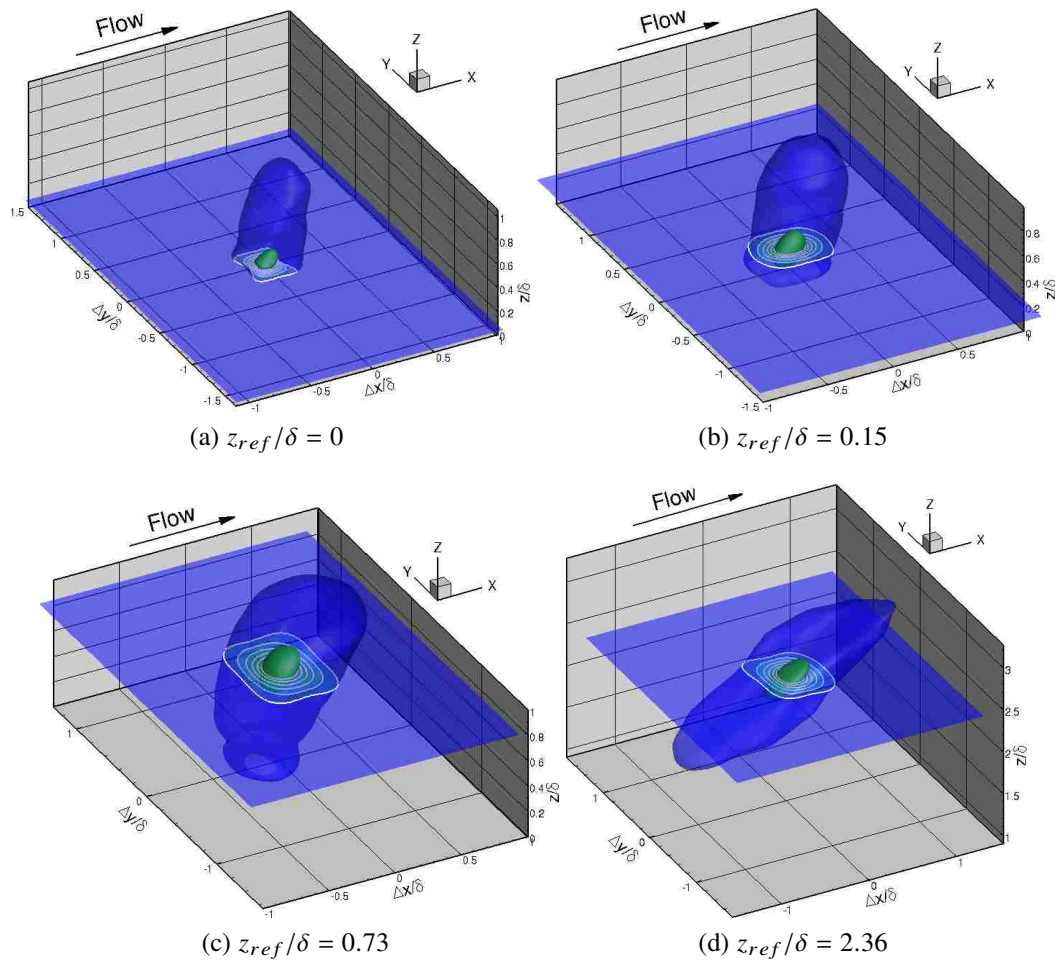
Figure 12. Three-dimensional representation of the spatial correlation coefficient C_{pp} of the pressure signal at multiple wall-normal locations for Case M6Tw025.
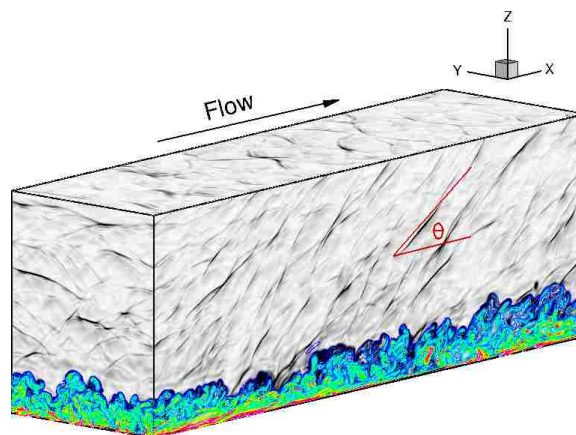
Figure 13. Instantaneous flow visualization for Case M6Tw025.

(a) Wall
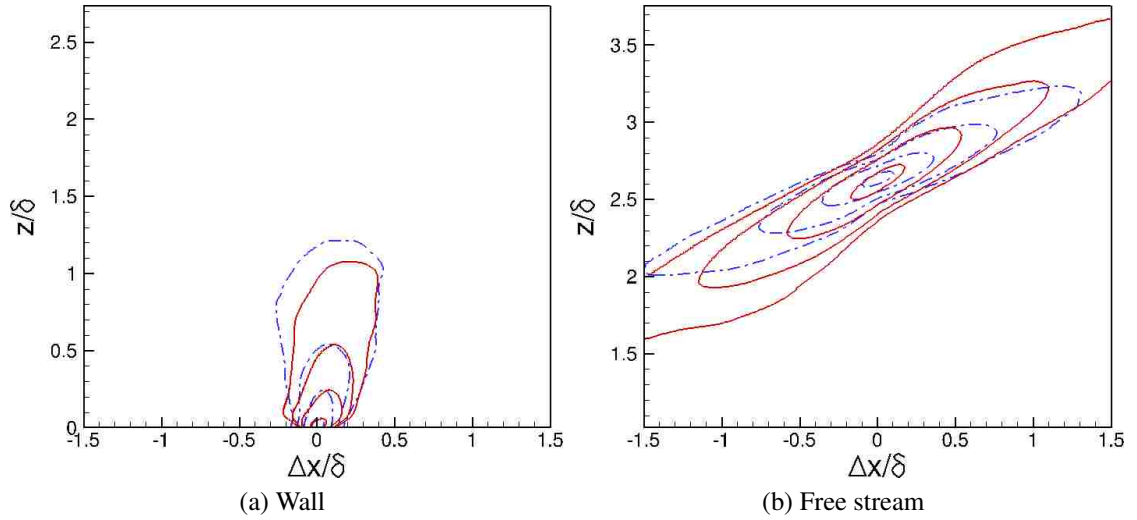
(b) Free stream

Figure 14. Contours of spatial correlation coefficient of the pressure signal C_{pp} in the streamwise wall-normal plane.

refraction before they are radiated to the free stream, resulting in a higher wave angle for Case M6Tw025; the reduction in refraction for Case M6Tw025 may be due to the less drastic variation in fluid properties (such as fluid density and temperature) because of wall cooling.

4.4. PROPAGATION AND EVOLUTION OF PRESSURE STRUCTURES

To quantify the overall propagation speed of pressure-carrying eddies or wavepackets as a function of distance from the wall, the bulk propagation speed is obtained as follows

$$U_b \equiv -\frac{\overline{(\partial p/\partial t)(\partial p/\partial x)}}{\overline{(\partial p/\partial x)^2}}. \tag{8}$$

The expression defines the bulk propagation speed U_b by finding the value of U_b that minimizes the difference between the real time evolution of $p(x,t)$ and a propagating frozen wave $p(x-U_b t)$. A figure of merit for the frozen-wave approximation can be further defined

as

$$\gamma_p \equiv \frac{\left|\overline{(\partial p/\partial x)(\partial p/\partial t)}\right|}{\left[\overline{(\partial p/\partial t)^2} \; \overline{(\partial p/\partial x)^2}\right]^{1/2}}, \tag{9}$$

where γ_p equals unity for a perfectly frozen wave, and is zero for fast decaying or deforming waves as they convect downstream. This definition of bulk propagation speed and figure of merit for the frozen-wave approximation was first used by Del Álamo and Jiménez (2009) for the streamwise velocity fluctuations in turbulent channel flows.
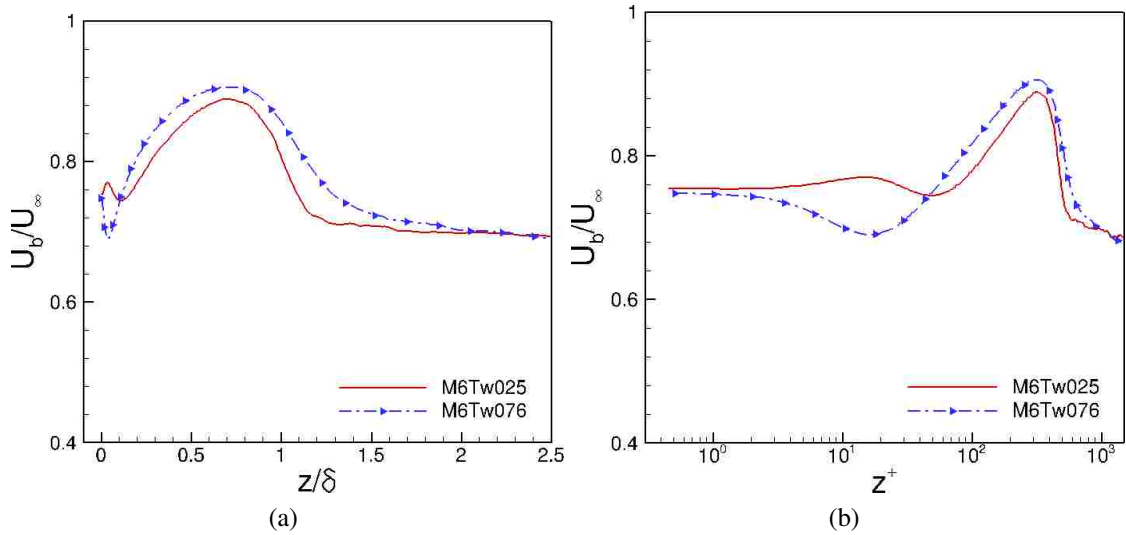
Figure 15. Comparison of bulk propagation speed of pressure fluctuations in (a) outer and (b) inner units between Case M6Tw025 and M6Tw076.

Figure 15 shows a comparison of the bulk propagation speed U_b between Cases M6Tw025 and M6Tw076. U_b is defined based on Equation 8. Wall cooling has small influence on the propagation speed of pressure structures within the main part of the boundary layer and has nearly no influence on the propagation speed of radiated pressure waves in the free stream. Consistent with previous findings (Duan *et al.*, 2014, 2016), the freestream propagation speed for Case M6Tw025 is significantly lower than the mean velocity in the free stream. Figure 16 shows the wall-normal distribution of γ_p that provides a figure of merit for the frozen-wave approximation for Cases M6Tw025 and M6Tw076. At both wall-temperature conditions, γ_p is close to unity across the boundary layer, indicating that the

propagation effect is overall more dominant over the evolution effect for the pressure structures. As the wall temperature decreases, the pressure structures become more 'frozen' with less significant evolution as they propagate downstream, especially for the pressure structures in the free stream.
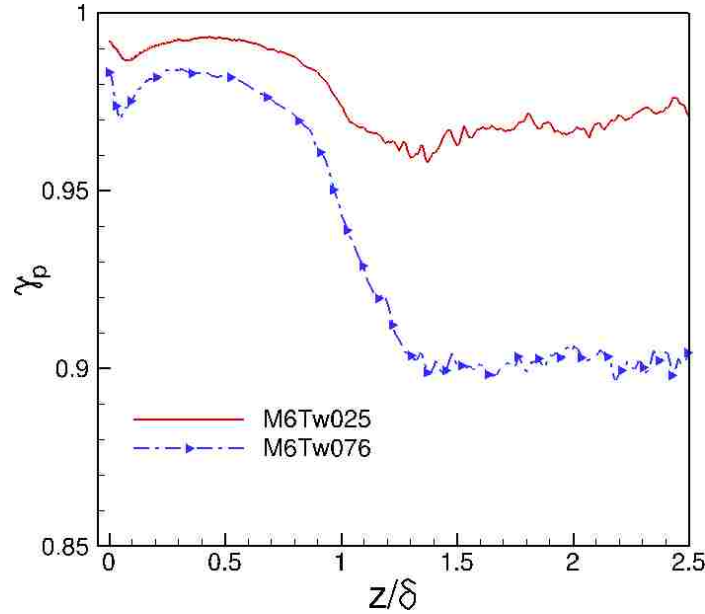
Figure 16. The distribution of correlation coefficient γ_p that provides a figure of merit for the frozen-wave approximation.

The propagation and evolution of large-scale pressure structures can be further investigated via the space-time correlation contours of pressure fluctuations. Figure 17 shows contours of constant space-time correlation $C_{pp}(\Delta x, 0, \Delta t, x_a, z_{ref}, z_{ref})$ at the wall ($z_{ref} = 0$) and in the free stream ($z_{ref} = z_\infty$) for Cases M6Tw025 and M6Tw076. ———: M6Tw025; —·—·—: M6Tw076. Four contour levels are shown: C_{pp}=0.1; 0.2; 0.4; 0.8. The skewed shape of the contours at both locations indicates the propagative nature of the pressure field, which is characterized by downstream propagation of either the coherent pressure-carrying eddies within the boundary layer or the pressure wavepackets in the free stream. Based on the space-time correlation data, the speed of propagation of pressure fluctuations can be estimated as the ratio $\Delta x/\Delta t$ for a given time delay Δt at the value of

(a) Wall   (b) Free stream
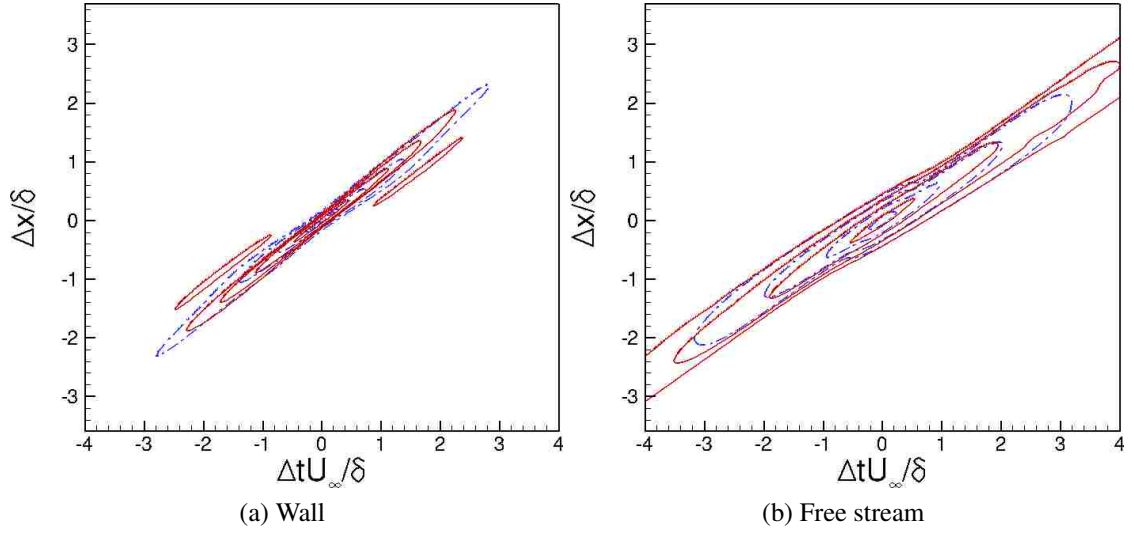
Figure 17. Contours of constant space-time correlation coefficient of the pressure signal $C_{pp}(\Delta x, 0, \Delta t, x_a, z_{ref}, z_{ref})$.

Δx where

$$\left. \frac{\partial C(r_x, 0, \Delta t, x_a, z_{ref}, z_{ref})}{\partial r_x} \right|_{r_x = \Delta x} = 0, \tag{10}$$

or for a given streamwise separation Δx at the value of Δt where

$$\left. \frac{\partial C(\Delta x, 0, r_t, x_a, z_{ref}, z_{ref})}{\partial r_t} \right|_{r_t = \Delta t} = 0. \tag{11}$$

Figures 18a and 18b compare the variation of bulk propagation speed with freestream Mach number at the wall and in the free stream, respectively, with some existing experiments and simulations. Symbols: squares, Kistler and Chen (1963); left triangles, Bernardini and Pirozzoli (2011); diamonds, Laufer (1964); letter A, B, C: Duan *et al.* (2014); up triangle, circle, down triangle: Case M6Tw025; letter D, E, F: Case M6Tw076. U_{b1}, U_{b2} and U_{b3} are defined based on Equation 10, 11 and 8, respectively. In the figure, U_{b1} is defined based on the space-time correlation coefficient with Equation 10 for the time delay Δt or frequency ($\omega = 2\pi/\Delta t$) where the pre-multiplied frequency spectrum (Figures 8 and 10) attains its maximum. In analogy, U_{b2} is derived based on Equation 11 for the streamwise

(a) Wall
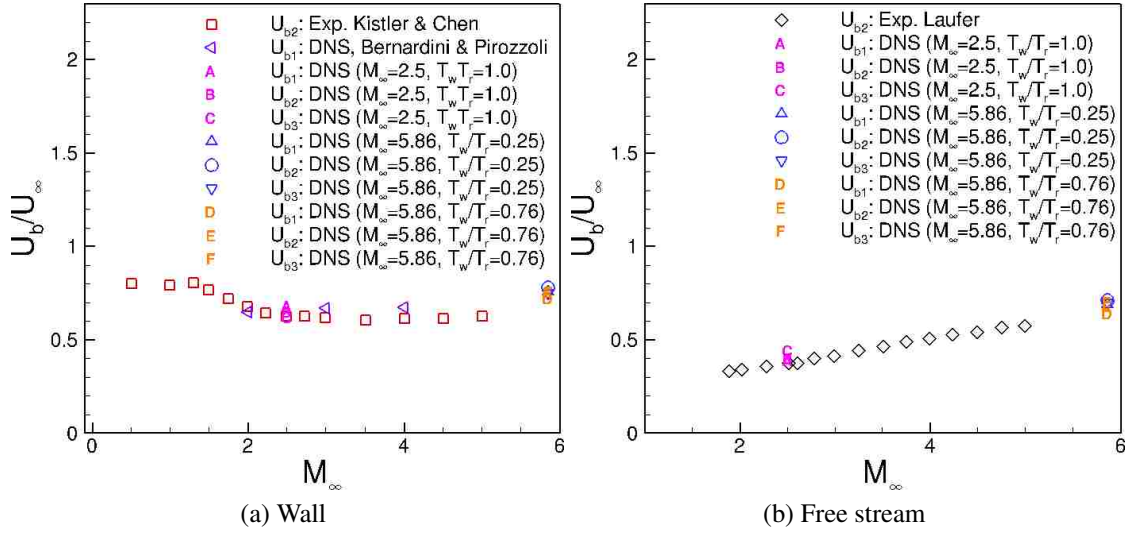
(b) Free stream

Figure 18. Bulk propagation speeds of the pressure fluctuation as a function of freestream Mach number.

separation Δx or wavenumber ($k_1 = 2\pi/\Delta x$) where the pre-multiplied one-dimensional wavenumber spectrum attains its maximum. U_{b3} is computed using Equation 8 by assuming 'frozen wave/eddy'. Consistent with Figure 15, the propagation speed based on the space-time correlation coefficient is comparable between Cases M6Tw025 and M6Tw076, indicating that wall cooling has only a small influence on the overall propagation speed of pressure structures away from the wall. The Mach-number dependence of bulk propagation speed is consistent with the previous data reported by Bernardini and Pirozzoli (2011) for U_b at the wall and by Duan $et\ al.$ (2014, 2016); Laufer (1964) for U_b in the free stream.

$$U_p(\omega) = \omega \Delta x / \theta_p(\omega) \tag{12}$$

To study the propagation speed of spectral components of pressure fluctuations, the phase speed of pressure fluctuations is defined in the above equation, where Δx is the distance between two pressure signals separated in the streamwise direction, and $\theta_p(\omega)$ is the phase difference between the two streamwise-separated pressure signals derived based on the cross-spectrum of the two signals. In the current study, the streamwsie separation Δx
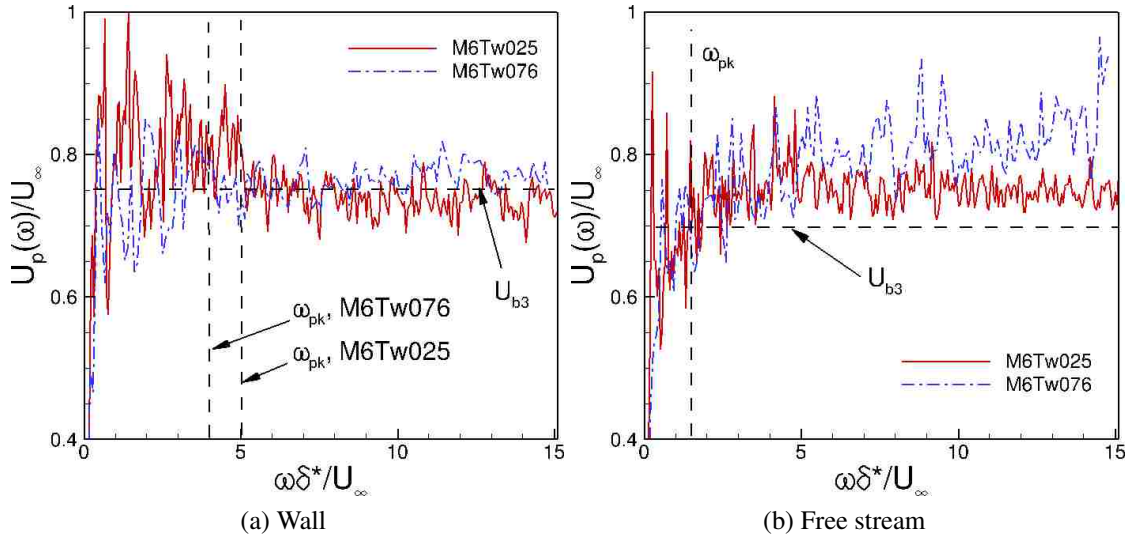
Figure 19. Comparison of phase speed.

is chosen to be the smallest streamwise distance at which two pressure signals are spatially sampled ($\Delta x^+ = 6.42$ and 28.9 for Case M6Tw025 and M6Tw076, respectively). At the selected streamwise separation, the coherence between the two signals is close to unity and the definition (Equation 12) thus provides a 'local' measurement of the phase speed. This definition was first used by Stegen and Van Atta (1970) to measure the local phase speed of the Fourier components of the longitudinal velocity fluctuations in grid turbulence with a small probe spacing. Figure 19 shows the phase speed of pressure fluctuations $U_p(\omega)$ at the wall and in the free stream. The phase speed $U_p(\omega)$ is defined based on Equation 19. The vertical dash line denotes the peak frequency ω_{pk} where the pre-multiplied frequency spectrum attains its maximum. At the wall, the phase speed shows a weak frequency dependence for both cases, and the wall-pressure structures of all frequencies propagate with speeds similar to the local bulk propagation speed. In the free stream, while the phase speed of the dominant pressure structures is similar to the local bulk propagation speed, wall cooling slightly increases the freestream phase speed at higher frequencies, and the high-frequency pressure structures propagate with a speed larger than the bulk propagation speed. To interpret the Lagrangian decorrelation length of the coherent pressure struc-
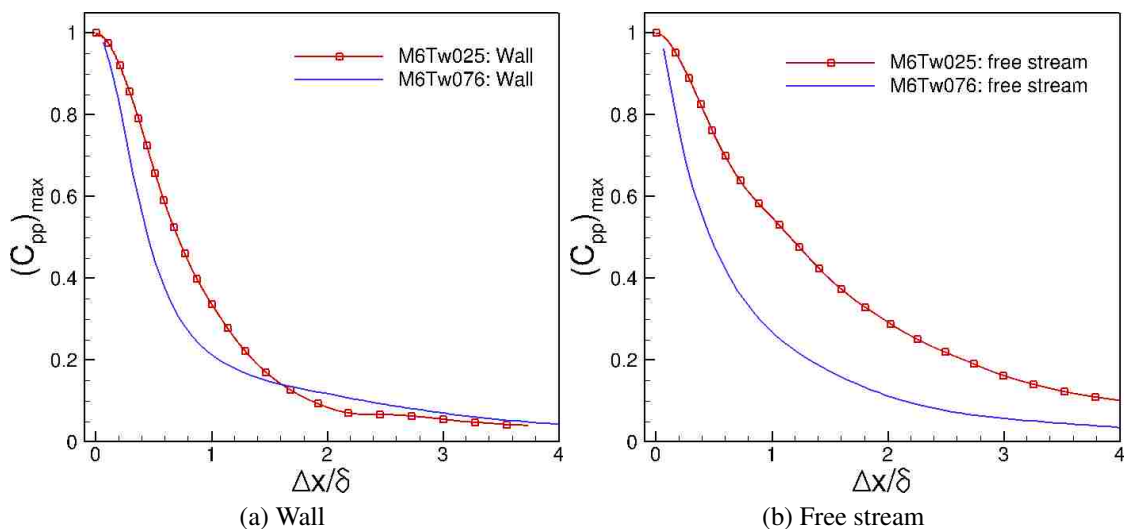
Figure 20. Comparison of the maximum spatial-time correlation coefficient of pressure fluctuations, $(C_{pp})_{max}$, as a function of streamwise separation Δx (a) at the wall and (b) in the free stream for Cases M6Tw025 and M6Tw076.

tures, Figure 20 compares the spatial decay of the maximum space-time correlation of pressure fluctuations, $(C_{pp})_{max}$, at the wall and in the free stream for Cases M6Tw025 and M6Tw076. The slower rate of spatial decay in $(C_{pp})_{max}$ for Case M6Tw025 indicates that wall cooling deenergizes pressure structures, making them evolve less rapidly as they propagate downstream. Such a trend is consistent with the larger values of the 'frozen-wave' index γ_p (Figure 16) for Case M6Tw025.

4.5. FREESTREAM ACOUSTIC RADIATION

In this section, the nature of freestream acoustic fluctuations radiated from the turbulent boundary layer is analyzed, including the modal compositions and the acoustic sources.

The characteristics of free-stream fluctuations is analyzed using the theory of modal analysis, which was initially proposed by Kovasznay (1953). According to Kovasznay, the fluctuations at any point within a uniform mean flow can be represented as a superposition

of three different modes with covarying physical properties: the vorticity mode, the acoustic or sound-wave mode and the entropy mode (also referred to as entropy spottiness or temperature spottiness).

Table 5 lists the freestream values of several fluctuating flow variables for Cases M6Tw025 and M6Tw076. R is the gas constant in the ideal-gas equation of state $p = \rho RT$. Here, s is specific entropy, Ω is the vorticity, and the subscript 't' denotes stagnation quantities. A comparison of the data from these two tables indicates that the magnitude of freestream fluctuations normalized by the respective mean values increase significantly as the wall temperature decreases, including both the velocity fluctuations and the fluctuations in thermodynamic variables. In particular, the pressure fluctuations in the free stream, including $p'_{rms}/\overline{p}$ and $p'_{t,rms}/\overline{p}_t$, are considerably different for both cases (3.47% vs 2.05% for $p'_{rms}/\overline{p}$, 1.08% vs 0.669% for $p'_{t,rms}/\overline{p}_t$, larger value for the colder-wall case). However, $p'_{rms}/\overline{p}$ and $p'_{t,rms}/\overline{p}_t$ bear nearly the same ratio of about 1.7 across the two cases. For both wall-temperature cases, the variation in r.m.s. amplitudes of velocity fluctuations along the three Cartesian axes indicates the anisotropy of the freestream velocity fluctuations, with the wall-normal component of the velocity fluctuations the largest among the three. The relative perturbations in thermodynamic variables are nearly an order of magnitude larger than the velocity fluctuations and nearly satisfy isentropic relations, indicating the acoustic nature of the freestream fluctuations. The dominance of the acoustic model is also indicated by the large ratio of the dilatational fluctuations $\overline{(\partial u'_i/\partial x_i)^2}$ to the vortical fluctuations $\overline{\Omega'_j \Omega'_j}$ and the small values of the entropy fluctuations s'_{rms}/R compared with the pressure fluctuations $p'_{rms}/\overline{p}$.

Laufer (1964) had assumed that the u' and p' fluctuations to be perfectly anticorrelated during the reduction of his hot wire measurements based on the assumption of purely planar acoustic waves. However, the numerical simulations for both values of surface temperature ratio show that the correlation coefficient between u' and p' is different from -1. Cooling of the surface leads to a correlation coefficient of -0.829 for Case M6Tw025,

Table 5. The freestream disturbance field for Cases M6Tw025 and M6Tw076.

	M6Tw076	M6Tw025
$u'_{rms}/\overline{u}$	1.36×10^{-3}	2.34×10^{-3}
$v'_{rms}/\overline{u}$	1.05×10^{-3}	1.62×10^{-3}
$w'_{rms}/\overline{u}$	2.05×10^{-3}	3.20×10^{-3}
$p'_{rms}/\overline{p}$	2.05×10^{-2}	3.47×10^{-2}
$\rho'_{rms}/\overline{\rho}$	1.46×10^{-2}	2.48×10^{-2}
$T'_{rms}/\overline{T}$	5.89×10^{-3}	9.89×10^{-3}
$(\rho u)'_{rms}/\overline{\rho u}$	1.38×10^{-2}	2.29×10^{-2}
$T'_{t,rms}/\overline{T}_t$	1.98×10^{-3}	3.08×10^{-3}
$p'_{t,rms}/\overline{p}_t$	6.69×10^{-3}	1.08×10^{-2}
$\overline{(\partial u'_i/\partial x_i)^2}/\overline{\Omega'_j \Omega'_j}$	31580	12153
s'_{rms}/R	2.11×10^{-3}	2.29×10^{-4}
$\overline{u'p'}/u'_{rms}p'_{rms}$	-0.653	-0.829
$\overline{v'p'}/v'_{rms}p'_{rms}$	-0.00639	-0.00512
$\overline{w'p'}/w'_{rms}p'_{rms}$	0.925	0.956
$\overline{\rho'p'}/\rho'_{rms}p'_{rms}$	1	1
$\overline{T'p'}/T'_{rms}p'_{rms}$	1	1

which is closer to -1 than the correlation coefficient of -0.653 for Case M6Tw076. The less significant deviation from the purely planar behavior for Case M6Tw025 may indicate that acoustic radiation becomes closer to planar acoustic waves with increased wall cooling.

To understand the effect of wall cooling on the pressure field, an analysis following Phillips (1960) has been carried out to study the acoustic sources that are responsible for the pressure fluctuations induced by the turbulent boundary layer. The acoustic source terms can be derived by rearranging the Navier-Stokes equations into the form of a wave equation, after neglecting the diffusive terms, as

$$\left\{ \frac{D^2}{Dt^2} - \frac{\partial}{\partial x_i} a^2 \frac{\partial}{\partial x_i} \right\} \log\left(\frac{p}{p_0}\right) = \gamma S, \tag{13}$$

where $S \equiv (\partial u_i/\partial x_j)(\partial u_j/\partial x_i)$ is the acoustic source term which is quadratic in the total flow velocity, p_0 is a convenient reference pressure, D/Dt is the substantial derivative based on mean flow velocity, and γ is the specific heat ratio. The terms on the left-hand side of

Equation 13 are those of a wave equation in a medium moving with the local mean velocity of the flow. The acoustic source term S on the right-hand side can be further decomposed into its linear (rapid) component $2(\partial \bar{U}/\partial z)(\partial w'/\partial x)$ and its nonlinear (slow) component $(\partial u'_i/\partial x_j)(\partial u'_j/\partial x_i)$. The details about the acoustic analogy equation, the definition and the decomposition of acoustic source terms are discussed in our previous papers (Duan *et al.*, 2014, 2016).
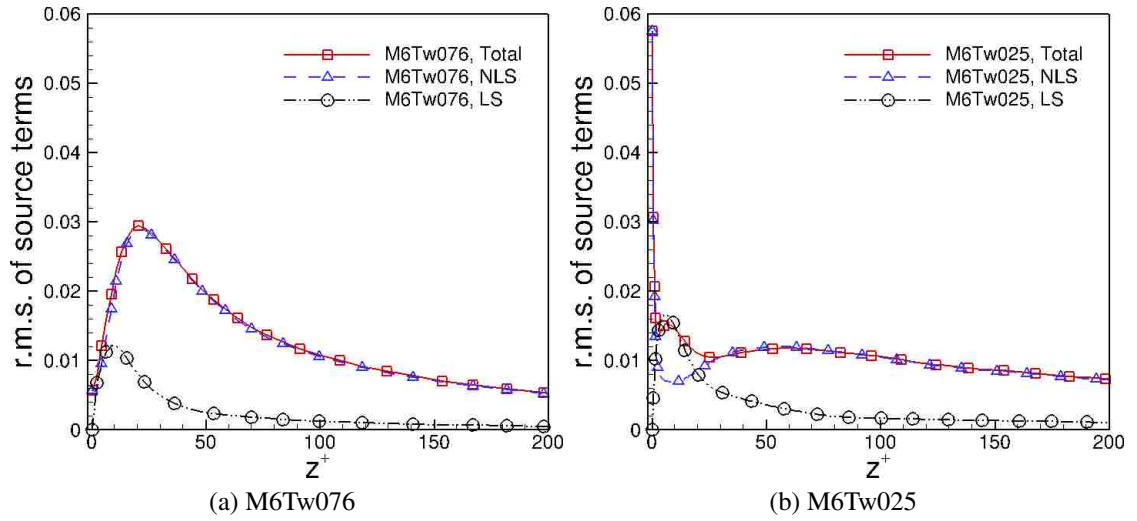
(a) M6Tw076   (b) M6Tw025

Figure 21. Profiles of the r.m.s. source terms (including the total, nonlinear source (NLS), and linear source (LS) terms) across the near-wall portion of the boundary layer.

Figure 21 plots the r.m.s. of the acoustic source term, S'_{rms}, and its linear and nonlinear components in the near-wall region of the boundary layer against wall-normal distance. The r.m.s. of the source terms are normalized by $(\nu_w/u_\tau^2)^2$. For both wall temperatures, the near-wall variation of the total acoustic source term conforms well with that of p'_{rms} (Figure 6b). For Case M6Tw076, the nonlinear source term is dominant over the linear term throughout the boundary layer (Figure 21a), and $(\partial v'/\partial z)(\partial w'/\partial y)$ has the largest r.m.s. among the constituent terms of the nonlinear acoustic source (Figure 22). The dominance of $(\partial v'/\partial z)(\partial w'/\partial y)$ may be indicative of the important role played by streamwise vortical structures in sound generation (Duan *et al.*, 2016).
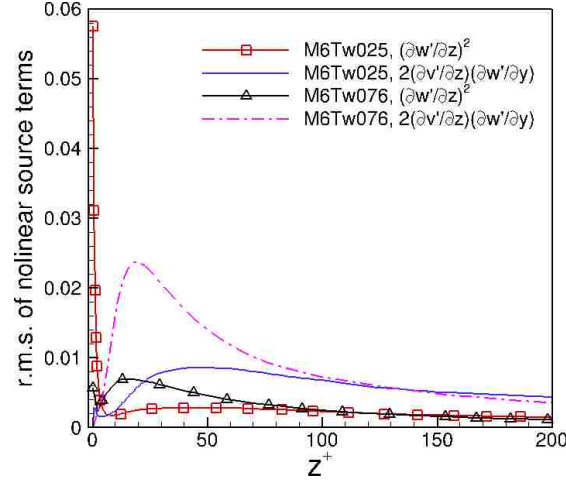
Figure 22. Profiles of the dominant acoustic source terms across the near-wall portion of the boundary layer.

As the wall temperature is decreased, the r.m.s. of the nonlinear acoustic term is significantly reduced in the buffer layer due to the damping of $(\partial v'/\partial z)(\partial w'/\partial y)$, and the linear source term becomes relatively more dominant in this region (Figure 21b). In the meantime, the r.m.s. value of the nonlinear acoustic term is dramatically increased in the viscous sublayer with $(\partial w'/\partial z)^2$ becoming the most dominant term in this region (Figure 22). Given that $(\partial w'/\partial z)^2$ is related to the dilatational fluctuations of velocity and $(\partial v'/\partial z)(\partial w'/\partial y)$ is related with the near-wall streamwise vortical fluctuations, the variation of these terms with wall temperature may indicate that wall cooling influences sound generation largely by enhancing dilatational motions in the viscous sublayer while damping streamwise vortical structures in the buffer layer. The enhancement of the dilatational motions in the viscous sublayer and the damping of the streamwise vortical structures in the boundary layer is also apparent from the rapid increase in r.m.s. dilation and r.m.s. streamwise vorticity near the wall, as seen from Figures 23a and 23b. The enhancement of dilatational motions near the wall is not unexpected as wall cooling increases the turbulent Mach number by causing a decrease in the local sound speed. Figure 24 compares the phase speed derived from the acoustic source term, $U_s(\omega)$, between Cases M6Tw025 and

M6Tw076 in the buffer layer. $U_s(\omega)$ is defined based on Equation 12 for the acoustic source term S. Wall cooling increases the convection speed of the acoustic sources for all frequencies. At the dominant frequency of freestream acoustic radiation $\omega_{pk}\delta/U_\infty = 1.5$, which corresponds to the peak frequency of the pre-multiplied spectrum shown in Figure 11a, the convection speed of the acoustic source is $0.64U_\infty$ ($M_r = 2.11$) and $0.55U_\infty$ ($M_r = 2.64$), respectively, for Cases M6Tw025 and M6Tw076, with $M_r \equiv (U_\infty - U_s)/a_\infty$. The fact that acoustic sources propagate supersonically with respect to the free stream is consistent with the concept of 'eddy Mach wave' radiation (Phillips, 1960). Given that the radiation wave angle can be approximated via the 'Mach angle' relation as $1/\sin\theta = M_r$, the smaller value of M_r for Case M6Tw025 is consistent with the larger radiation wave angle of $28°$ for this case (Figure 14b).
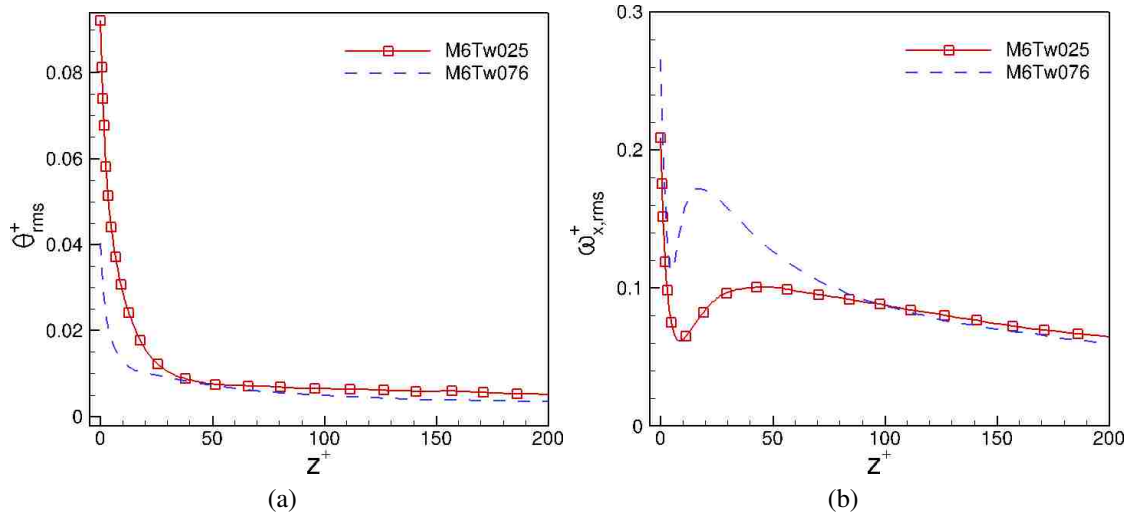
Figure 23. Profiles of the r.m.s. of dilatation and streamwise vorticity across the near-wall portion of the boundary layer normalized using ν_w/u_τ^2.

5. SUMMARY AND CONCLUSIONS

DNS of Mach 5.86 turbulent boundary layers with two wall temperatures ($T_w/T_r = 0.25, 0.76$) are compared to investigate the effect of wall cooling on the pressure fluctuations generated by hypersonic turbulent boundary layers. Simulations show that wall cool-
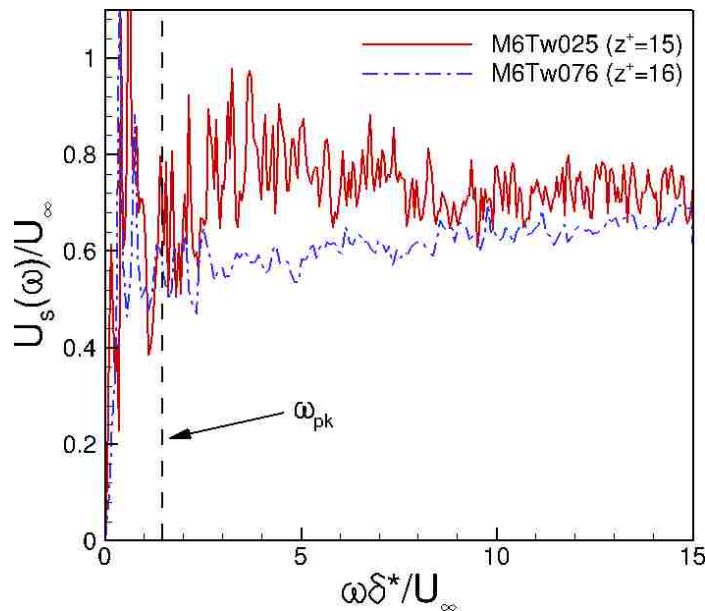
Figure 24. Phase speed of the acoustic source term.

ing significantly modifies the pressure-fluctuation intensities near the wall, with $p'_{w,rms}/\tau_w$ varying from 2.8 for $T_w/T_r = 0.76$ to 3.5 for $T_w/T_r = 0.25$. Furthermore, the frequency spectra of wall-pressure fluctuations for the two cases show considerable differences when plotted in terms of either outer-layer or inner-layer variables. The peak of the pre-multiplied spectrum shifts to a higher value as the wall temperature decreases. Wall cooling slows down the evolution of pressure wavepackets at the wall, resulting in a larger decorrelation length of pressure structures, but has little influence on the bulk propagation speeds of wall-pressure structures. Regarding the freestream pressure fluctuations, although the intensity shows a strong wall-temperature dependence when normalized by the mean freestream pressure ($\overline{p}_\infty$), it compares well between the two cases when normalized by the local wall shear stress τ_w. The frequency spectra of freestream radiation collapse well between the two cases when normalized in terms of outer or inner boundary-layer parameters. Wall cooling results in an increase in the radiation wave angle (defined based on spatial correlations C_{pp}) from $21°$ for $T_w/T_r = 0.76$ to $28°$ for $T_w/T_r = 0.25$. Similar to pressure structures at the wall, the freestream pressure structures evolve less rapidly as the wall temperature

decreases. The propagation speed of freestream pressure structures is found to be insensitive to wall temperature and is significantly smaller than the freestream velocity for both cases. An analysis of acoustic sources using the acoustic analogy of Phillips (1960) shows that wall cooling influences sound generation largely by enhancing dilatational motions in the viscous sublayer while damping streamwise vortical structures in the buffer layer.

ACKNOWLEDGEMENTS

REFERENCES

Beresh, S. J., Henfling, J. F., Spillers, R. W., and Pruett, B. O. M., 'Fluctuating wall pressures measured beneath a supersonic turbulent boundary layer,' Phys. Fluids, 2011, **23**(7), p. 075110.

Bernardini, M. and Pirozzoli, S., 'Wall pressure fluctuations beneath supersonic turbulent boundary layers,' Phys. Fluids, 2011, **23**(8), p. 085102.

Bernardini, M., Pirozzoli, S., and Grasso, F., 'The wall pressure signature of transonic shock/boundary layer interaction,' J. Fluid Mech., 2011, **671**, pp. 288–312.

Blake, W. K., *Mechanics of Flow-Induced Sound and Vibration*, Academic Press, Orlando, Florida, 1986.

Bowersox, R. D. W., 'Extension of equilibrium turbulent heat flux models to high-speed shear flows,' J. Fluid Mech., 2009, **633**, pp. 61–70.

Bull, M. K., 'Wall-pressure fluctuations beneath turbulent boundary layers: Some reflection on forty years of research,' J. Sound Vib., 1996, **190**(3), pp. 299–315.

Chu, Y. B., Zhang, Y. Q., and Lu, X. Y., 'Effect of wall temperature on hypersonic turbulent boundary layer,' J. Turbul., 2013, **14**(12), pp. 37–57.

Del Álamo, J. C. and Jiménez, J., 'Estimation of turbulent convection velocities and corrections to Taylor's approximation,' J. Fluid Mech., 2009, **640**, pp. 5–26.

Di Marco, A., Camussi, R., Bernardini, M., and Pirozzoli, S., 'Wall pressure coherence in supersonic turbulent boundary layers,' J. Fluid Mech., 2013, **732**, pp. 445–456.

Duan, L., Beekman, I., and Martín, M. P., 'Direct numerical simulation of hypersonic turbulent boundary layers. Part 2: Effect of wall temperature,' J. Fluid Mech., 2010, **655**, pp. 419–445.

Duan, L., Choudhari, M. M., and Wu, M., 'Numerical study of pressure fluctuations due to a supersonic turbulent boundary layer,' J. Fluid Mech., 2014, **746**, pp. 165–192.

Duan, L., Choudhari, M. M., and Zhang, C., 'Pressure fluctuations induced by a hypersonic turbulent boundary layer,' J. Fluid Mech., 2016, **804**, pp. 578–607.

Fernholz, H. H., Dussauge, J. P., Finlay, P. J., Smits, A. J., and Reshotko, E., 'A survey of measurements and measuring techniques in rapidly distorted compressible turbulent boundary layers,' AGARDograph, 1989, **315**, pp. 1–18.

Fernholz, H. H. and Finley, P. J., 'Critical commentary on mean flow data for two-dimensional compressible turbulent boundary layers.' AGARDograph, 1980, **253**.

Hadjadj, A., Ben-Nasr, O., Shadloo, M. S., and Chaudhuri, A., 'Effect of wall temperature in supersonic turbulent boundary layers: A numerical study,' Int. J. Heat Mass Transfer, 2015, **81**, pp. 426–438.

Huang, P. G., Coleman, G., and Bradshaw, P., 'Compressible turbulent channel flows: DNS results and modelling,' J. Fluid Mech., 1995, **305**, pp. 185–218.

Kistler, A. L. and Chen, W. S., 'The fluctuating pressure field in a supersonic turbulent boundary layer,' J. Fluid Mech., 1963, **16**, pp. 41–64.

Kovasznay, L. S. G., 'Turbulence in supersonic flow,' J. Aeronaut. Sci., 1953, **20**, pp. 657–674.

Lagha, M., Kim, J., Eldredge, J. D., and Zhong, X., 'A numerical study of compressible turbulent boundary layers,' Phys. Fluids, 2011, **23**(1), p. 015106.

Laufer, J., 'Some statistical properties of the pressure field radiated by a turbulent boundary layer,' Phys. Fluids, 1964, **7**(8), pp. 1191–1197.

Lele, S. K., 'Compressibility Effects on Turbulence,' Annu. Rev. Fluid Mech, 1994, **26**, pp. 211–254.

Maeder, T., *Numerical investigation of supersonic turbulent boundary layers*, Ph.D. thesis, ETH, Zürich, 2000.

Modesti, D. and Pirozzoli, S., 'Reynolds and Mach number effects in compressible turbulent channel flow,' Int. J. Heat Fluid Flow, 2016, **59**, pp. 33–49.

Morkovin, M. V., 'Effects of compressibility on turbulent flows,' in A. J. Favre, editor, 'Mécanique de la Turbulence,' CNRS, 1962 pp. 367–380.

Peltier, S. J., Humble, R. A., and Bowersox, R. D. W., 'Crosshatch roughness distortions on a hypersonic turbulent boundary layer,' Phys. Fluids, 2016, **28**(4), p. 045105.

Phillips, O. M., 'On the generation of sound by supersonic turbulent shear layers,' J. Fluid Mech., 1960, **9**, pp. 1–28.

Poggie, J., 'Compressible turbulent boundary layer simulations: Resolution effects and turbulence modeling,' AIAA Paper 2015-1983, 2015.

Schlatter, P. and Örlü, R., 'Assessment of direct numerical simulation data of turbulent boundary layers,' J. Fluid Mech., 2010, **659**, pp. 116–126.

Schneider, S. P., 'Effects of high-speed tunnel noise on laminar-turbulent transition,' J. Spacecr. Rockets, 2001, **38**(3), pp. 323–333.

Shadloo, M. S., Hadjadj, A., and Hussain, F., 'Statistical behavior of supersonic turbulent boundary layers with heat transfer at $M_\infty = 2$,' Int. J. Heat Fluid Flow, 2015, **53**, pp. 113–134.

Shahab, M. F., Lehnasch, G., GatskiEmail, T. B., and Comte, P., 'Statistical characteristics of an isothermal, supersonic developing boundary layer flow from DNS data,' Flow Turbul. Combust, 2011, **86**(3), pp. 369–397.

Smits, A. J., 'Turbulent boundary layer structure in supersonic flow,' Phil. Trans. R. Soc. London Ser. A, 1991, **336**(1641), pp. 81–93.

Smits, A. J. and Dussauge, J. P., *Turbulent Shear Layers in Supersonic Flow*, American Institute of Physics, 2 edition, 2006.

Steen, L. E., *Characterization and Development of Nozzles for a Hypersonic Quiet Wind Tunnel*, Master's thesis, Purdue University, West Lafayette, IN, USA, 2010.

Stegen, G. R. and Van Atta, C. W., 'A technique for phase speed measurements in turbulent flows,' J. Fluid Mech., 1970, **42**, pp. 689–699.

Trettel, A. and Larsson, J., 'Mean velocity scaling for compressible wall turbulence with heat transfer,' Phys. Fluids, 2016, **28**(2), p. 026102.

Tsuji, Y., Fransson, J. H. M., Alferdsson, P. H., and Johansson, A. V., 'Pressure statistics and their scaling in high-Reynolds-number turbulent boundary layers,' J. Fluid Mech., 2007, **585**, pp. 1–40.

Walz, A., *Boundary Layers of Flow and Temperature*, MIT Press, 1969.

Welch, P. D., 'The use of Fast Fourier Transform for the estimation of power spectra: A method based on time averaging over short, modified periodograms,' IEEE Trans. Audio Electroacoustics, 1967, **AU-15**, pp. 70–73.

Wu, B., Bi, W., Hussain, F., and She, Z. S., 'On the invariant mean velocity profile for compressible turbulent boundary layers,' J. Turbul., 2016, pp. 1–17.

Zhang, Y., Bi, W., Hussain, F., and She, Z., 'A generalized Reynolds analogy for compressible wall-bounded turbulent flows,' J. Fluid Mech., 2014, **739**, pp. 392–420.

III. DIRECT NUMERICAL SIMULATION DATABASE FOR SUPERSONIC AND HYPERSONIC TURBULENT BOUNDARY LAYERS

CHAO ZHANG[1], LIAN DUAN[1] and MEELAN M. CHOUDHARI[2]

[1]Missouri University of Science and Technology, Rolla, MO 65401, USA

[2]NASA Langley Research Center, Hampton, VA 23681, USA

ABSTRACT

In this paper, we present a direct numerical simulation database of high-speed zero-pressure-gradient turbulent boundary layers developing spatially over a flat plate with nominal freestream Mach number ranging from 2.5 to 14 and wall-to-recovery temperature ranging from 0.18 to 1.0. The flow conditions of the DNS are representative of the operational conditions of the Purdue Mach 6 quiet tunnel, the Sandia Hypersonic Wind Tunnel at Mach 8, and the AEDC Hypervelocity Tunnel No. 9 at Mach 14. The DNS database is used to gauge the performance of compressibility transformations, including the classical Morkovin's scaling and strong Reynolds analogy as well as the newly proposed mean velocity and temperature scalings that explicitly account for wall heat flux. Several insights into the effect of direct compressibility are gained by inspecting the thermodynamic fluctuations and the Reynolds stress budget terms. Precomputed flow statistics, including Reynolds stresses and their budgets, will be available at the website of the NASA Langley Turbulence Modeling Resource, allowing other investigators to query any property of interest.

Keywords: high-speed flow, turbulence simulation, turbulent boundary layers

1. INTRODUCTION

The knowledge of turbulent boundary layers at high Mach numbers is important to the design of high speed vehicles, as turbulent boundary layers determine the aerodynamic drag and heat transfer. One of the most important foundations for our understanding of high speed turbulence is Morkovin's hypothesis, which postulates that high speed turbulence structure in zero pressure-gradient turbulent boundary layers remains largely the same as its incompressible counterpart (Smits and Dussauge, 2006). An important consequence of Morkovin's hypothesis is the so-called 'compressibility transformations' that transform the mean velocity and Reynolds stress profiles in a compressible boundary layer to equivalent incompressible profiles by accounting for mean property variations across the thickness of the boundary layer. A classical example of such transformations is the density-weighted velocity scaling of Van Driest (van Driest, 1956). Another consequence of Morkovin's hypothesis is the analogy between the temperature and velocity fields that leads to velocity-temperature relations such as the classical Walz formula (Walz, 1969) and the strong Reynolds numbers analogy (SRA) (Gaviglio, 1987; Huang *et al.*, 1995; Morkovin, 1962). In addition to the classical Van Driest transformation and the SRA, which have been verified largely for supersonic turbulent boundary layers ($M_\infty < 5$) with an adiabatic wall, new mean velocity and velocity-temperature scaling relations have recently been proposed to explicitly account for a finite wall heat flux (Patel *et al.*, 2016; Trettel and Larsson, 2016; Zhang *et al.*, 2014). For example, Patel et al. (Patel *et al.*, 2015) proposed a semilocal Reynolds number Re_τ^* for comparing wall turbulence statistics among cases with substantially different mean density and viscosity profiles. Trettel and Larsson (Trettel and Larsson, 2016) recently provided an extension to the Van Driest transformation for compressible wall turbulence with heat transfer by deriving a novel velocity transformation based on arguments about log-layer scaling and near-wall momentum conservation. Zhang et al. (Zhang *et al.*, 2014) generalized the temperature-velocity relation of Walz and Huang's SRA to explicitly account for a finite wall heat flux. These

new scaling relations have been shown to yield much improved collapse of the supersonic data to the incompressible case when there is a strong heat transfer at the surface (Modesti and Pirozzoli, 2016). The success of the compressibility transformations and the SRA may suggest that there exist few, if any, dynamic differences due to Mach number, as postulated by Morkovin, at least for wall turbulence at moderate Mach numbers ($M_\infty < 5$).

At hypersonic speeds ($M_\infty > 5$), the validity of Morkovin's hypothesis may come into question because of the increasing density and pressure fluctuations at high Mach numbers. Turbulent fluctuations can even become locally supersonic relative to the surrounding flow, creating the so-called eddy shocklets that could significantly modify the dynamics of the flow. However, the Mach number at which Morkovin's hypothesis would lose significant accuracy remains largely undetermined. There are still limited measurements at hypersonic speeds that are detailed and accurate enough for testing the validity of Morkovin's hypothesis. Experimental investigations of hypersonic turbulent boundary layers have been conducted historically with hot-wire anemometry (see, for example, the review by Roy and Blottner (Roy and Blottner, 2006)). A recent investigation by Williams et al. (Williams *et al.*, 2018) showed that much of the historical hot-wire measurements of turbulence statistics suffered from poor frequency response and/or spatial resolution. Hot-wire anemometry may also suffer from uncertainties associated with the mixed-mode sensitivity of the hot wires, given that the hot wire measures a combination of the fluctuating mass flux and the fluctuating total temperature (Kovasznay, 1953). In addition to hot-wire anemometry, direct measurements of spatially varying velocity fields of high-speed turbulent boundary layers have been attempted using Particle Image Velocimetry (PIV) (Ekoto *et al.*, 2008; Peltier *et al.*, 2016; Tichenor *et al.*, 2013; Williams *et al.*, 2018). Among the existing PIV measurements, the measurement by Williams et al. (Williams *et al.*, 2018) in a Mach 7.5 flat-plate turbulent boundary layer is the only PIV measurement conducted at a Mach number above five. Although the existing PIV results provided direct experimental evidence for the validity of Morkovin scaling for the streamwise velocity at Mach numbers

as high as 7.5, accurate measurements were not yet acquired for the wall-normal compo-
nent of the velocity or the Reynolds stress. The existing PIV data exhibited reduced levels
of the wall-normal component of the velocity in comparison with the predictions based on
the Morkovin scaling, and the deviation became larger with increasing Mach number. As
noticed by Williams et al. (Williams *et al.*, 2018), the loss in accuracy is largely due to par-
ticle response limitations that result in significantly reduced levels of wall-normal velocity
fluctuations.

Complementary to experiments, direct numerical simulations (DNS) of high-speed
turbulent boundary layers have been conducted to overcome the experimental difficulties
and provide access to three-dimensional turbulence statistics. Although several DNS have
been conducted for studying Morkovin's scaling in turbulent boundary layers with moder-
ate freestream Mach number ($M < 5$) (Hadjadj *et al.*, 2015; Maeder, 2000; Modesti and
Pirozzoli, 2016; Pirozzoli and Bernardini, 2011; Poggie *et al.*, 2015; Shahab *et al.*, 2011;
Trettel and Larsson, 2016; Zhang *et al.*, 2014), there is little DNS data for turbulent bound-
ary layers in the high Mach number regime (Roy and Blottner, 2006). Martín (Martín, 2007,
June 2004) made a pioneering effort toward characterizing boundary-layer turbulence in
the hypersonic regime by developing a temporal DNS database of canonical zero-pressure-
gradient, flat-plate turbulent boundary layers up to Mach 8 with varying wall temperatures.
Duan et al. (Duan *et al.*, 2010, 2011; Duan and Martín, 2011) extended the datasets of
Martín (Martín, June 2004) to even higher Mach numbers (up to Mach 12) with cold wall
and high enthalpy and conducted a systematic study of wall turbulence and its dependence
on freestream Mach number, wall cooling, and high enthalpy. Additional DNS studies of
hypersonic turbulent boundary layers in the literature include that by Lagha et al. (Lagha
et al., 2011) up to Mach 20 with an adiabatic wall ($T_w/T_r = 1.0$) and that by Priebe and
Martín at Mach 7.2 (Priebe and Martín, June 2011) with $T_w/T_r = 0.53$. Except for the work
by Duan et al. (Duan *et al.*, 2010), who systematically studied the effect of wall cooling
on boundary-layer turbulence at Mach 5, most of the previous DNS at high Mach number

simulated a turbulent boundary layer over a hypothetically adiabatic wall. The new scaling relations of Refs. (Patel *et al.*, 2016; Trettel and Larsson, 2016; Zhang *et al.*, 2014) that explicitly account for finite wall heat flux have not yet been systematically assessed under high Mach number, cold-wall conditions.

As far as the modeling of high-speed turbulence is concerned, the most common classes of compressibility correction for Reynolds-averaged Navier-Stokes (RANS) turbulence models were developed for improving predictions of free-shear layers or jets. As such, these corrections are often unacceptable for attached boundary layer flows. However, practical experiences indicate that the need for correction in hypersonic boundary layers becomes increasingly evident as Mach number increases, particularly for cold walls (Rumsey, 2010; Zeman, Jan. 1993). In particular, Rumsey (Rumsey, 2010) recently investigated the performance of many of the compressibility corrections described in the literature for $k - \omega$ turbulence models in hypersonic boundary-layer applications. He found that the dilatation-dissipation correction designed by Zeman (Zeman, Jan. 1993) works reasonably well for predicting turbulent skin friction at high-Mach-number, cold wall conditions. As concluded by Rumsey, the effects of dilatation-dissipation and pressure-dilation on turbulence models are still not clear for high-Mach-number, cold wall cases, and there is a need for improved understanding and better physical modeling for turbulence models applied to hypersonic boundary layers.

In the present paper, we describe a new DNS database of spatially developing, flat-plate turbulent boundary layers that was developed using a large computational domain with low-dissipative spatial discretization, and that covers a wide range of freestream Mach number ($M_\infty = 2.5 - 14$) and wall-to-recovery temperature ratio ($T_w/T_r = 0.18 - 1.0$). Unlike the temporal DNS of Martín (Martín, June 2004) and Duan et al. (Duan *et al.*, 2010, 2011) that used a small streamwise domain ($\approx 8\delta$) with a periodic boundary condition in the streamwise direction, these DNS simulate spatially developing turbulent boundary layers with a long streamwise domain length ($> 50\delta_i$) to minimize any artificial effects

of inflow turbulence generation and to guarantee the convergence of high-order turbulence statistics. Moreover, the new DNS database mimics realistic flow conditions such as those in hypersonic wind tunnel facilities with a cooled wall rather than simulating hypersonic turbulent boundary layers over a hypothetically adiabatic wall (Duan *et al.*, 2011; Lagha *et al.*, 2011; Martín, 2007). The combination of high freestream Mach number (with nominal freestream Mach number as high as $M_\infty = 14$) and cold wall temperature (with wall-to-recovery temperature as low as $T_w/T_r = 0.18$) covered in the database extends the available database to more extreme, yet practical, cases that serve as a reference for modeling wall-bounded turbulence in the high-Mach-number, cold-wall regime as well as for developing novel compressibility transformations that collapse compressible boundary-layer profiles to incompressible results. For that purpose, both statistical quantities and subsets of raw flow samples are made publicly available on a web site, which will allow other investigators to access any property of interest. In the following sections, we briefly describe the DNS methodology and present a limited number of numerical results, including a comparison with recent experimental data and an application of the numerical data to gauge the performance of some recently proposed compressibility transformations (Trettel and Larsson, 2016; Zhang *et al.*, 2014) and to probe intrinsic compressibility effects.

2. NUMERICAL DATABASE AND UNDERLYING METHODOLOGY

The database used for the current analysis includes the DNS of spatially-developing, flat-plate turbulent boundary layers over a wide range of nominal freestream Mach numbers ($M_\infty = 2.5$–14) and wall-to-recovery temperature ratios ($T_w/T_r = 0.18$–1.0). Table 1 outlines the freestream conditions for the simulations, and Table 2 summarizes the boundary-layer parameters at a selected location where the turbulence statistics are gathered.

Cases M2p5, M6Tw076, and M6Tw025 correspond to the DNS reported in previous papers (Duan *et al.*, 2014, 2016; Zhang *et al.*, 2017, Jan. 2016), in which pressure statistics including the freestream acoustic radiation were presented and discussed in detail.

Table 1. Freestream and wall-temperature conditions for various DNS cases.

Case	M_∞	U_∞ (m/s)	ρ_∞ (kg/m^3)	T_∞ (K)	T_w (K)	T_w/T_r	δ_i (mm)
M2p5	2.50	823.6	0.100	270.0	568.0	1.0	4.0
M6Tw025	5.84	869.1	0.044	55.2	97.5	0.25	1.3
M6Tw076	5.86	870.4	0.043	55.0	300.0	0.76	13.8
M8Tw048	7.87	1155.1	0.026	51.8	298.0	0.48	20.0
M14Tw018	13.64	1882.2	0.017	47.4	300.0	0.18	18.8

The flow conditions of Case M2p5 match those of the temporal simulation of Guarini et al. (Guarini *et al.*, 2000); Case M6Tw076 simulates representative conditions of the Purdue Mach 6 Quiet Tunnel; Case M6Tw025 has nearly identical flow conditions as the wind-tunnel relevant case M6Tw076 while varying the surface temperature ratio T_w/T_r from 0.76 to 0.25 to allow an assessment of the effect of surface temperature. Two additional cases at higher freestream Mach numbers (Cases M8Tw048 and M14Tw018) are presented herein for the first time, with flow conditions representative of the nozzle exit of the Sandia Hypersonic Wind Tunnel at Mach 8 and the AEDC Hypervelocity Tunnel No. 9 at Mach 14, respectively. The new cases extend the available database to more extreme, yet practical, cases that would allow one to probe the effects of Mach number on turbulence scaling and structure under these conditions. Choosing flow conditions that are representative of several hypersonic wind tunnels has led to successful one-to-one comparisons of the DNS with experimental measurements in these wind tunnels (Duan *et al.*, Jan. 2018). As much as possible, the Re_τ parameter is kept within the narrow range of 450–500, the only exception being the Mach 14 case where the Re_τ increased because a longer spatial domain was necessary to ensure that the effects of inflow treatment had decayed and the boundary layer had achieved a quasi-equilibrium state. The decision to match Re_τ is based on the existing literature (Lagha *et al.*, 2011; Shadloo *et al.*, 2015) as well as on the need to limit the computational costs even though simulations at a single Reynolds number may not be sufficient to characterize the flow (Lele, 1994; Smits and Martín, Aug. 2004). All the DNS

cases fall within the perfect gas regime. The working fluid is air with viscosity calculated by using Sutherland's law, except for Case M8Tw048 where the working fluid is nitrogen and its viscosity is calculated by using Keyes law (Keyes, 1951). Compared to the large differences in boundary-layer properties caused by varying the freestream Mach number and the wall temperature, the differences caused by using a different working fluid in DNS are small, if not negligible. A constant molecular Prandtl number of 0.71 is used for all of the DNS cases.

Table 4 summarizes the domain sizes and grid resolutions for all DNS cases. The simulations either involve a single domain with a long streamwise box or are carried out in two stages involving overlapping streamwise domains as illustrated in Figure 1. An instantaneous flowfield is shown, visualized by an isosurface of the density gradient magnitude, corresponding to $|\nabla \rho| \delta_i / \rho_\infty = 0.9825$, colored by the streamwise velocity component (with levels from 0 to U_∞, blue to red). The boundary layer is allowed to develop spatially over an extended region along the streamwise direction ($> 50\delta_i$) so as to minimize any artificial effects of the inflow turbulence generation and to contain the largest relevant flow structures within the computational domain. The two overlapping streamwise domains used in Case M14Tw018 further minimize any artificial effects of the rescaling procedure. This conservative approach was deemed necessary because of the combination of higher freestream Mach number and colder wall temperature than the other cases considered herein, as well as in other computational studies reported in the literature. Another noteworthy feature of the present database corresponds to the large spanwise domain (nearly an order of magnitude larger than the boundary layer thickness), which guarantees spanwise statistical decorrelation in turbulence fluctuations throughout the boundary layer.

The boundary layer is simulated in a rectangular box over a flat plate with spanwise periodic boundary conditions and a modified rescaling/recycling method for inflow turbulence generation (Duan *et al.*, 2014). The numerical code solves the compressible Navier-Stokes equations in conservative form, using an optimized seventh-order weighted essen-

Table 2. Boundary layer properties at the station selected for the analysis for various DNS cases. Part 1.

Case	x_a/δ_i	θ (mm)	H	δ (mm)	z_τ (μm)	u_τ (m/s)	$-B_q$	M_τ
M2p5	53.0	0.58	4.1	7.7	15.0	40.6	0	0.08
M6Tw025	88.6	0.20	8.4	3.6	8.0	33.8	0.14	0.17
M6Tw076	54.1	0.95	13.6	23.8	52.6	45.1	0.02	0.13
M8Tw048	56.9	1.19	17.4	35.2	73.5	54.3	0.06	0.15
M14Tw018	199.3	1.35	37.6	66.1	102.4	67.6	0.19	0.19

Table 3. Boundary layer properties at the station selected for the analysis for various DNS cases. Part 2.

Case	x_a/δ_i	Re_θ	Re_τ	Re_{δ_2}	Re_τ^*	$-B_q$	M_τ
M2p5	53.0	2835	510	1657	1187	0	0.08
M6Tw025	88.6	2121	450	1135	932	0.14	0.17
M6Tw076	54.1	9455	453	1746	4130	0.02	0.13
M8Tw048	56.9	9714	480	1990	4092	0.06	0.15
M14Tw018	199.3	14408	646	2354	4925	0.19	0.19

tially nonoscillatory (WENO) scheme (Martín *et al.*, 2006; Taylor *et al.*, 2006) for capturing eddy shocklets and ensuring numerical stability. A third-order low-storage Runge-Kutta scheme is used for time integration (Williamson, 1980). A detailed description of the problem formulation, the numerical scheme, and the initial and boundary conditions can be found in Ref. (Duan *et al.*, 2014, 2016; Zhang *et al.*, 2017, Jan. 2016). The validity of numerical methods and procedures have been established in multiple previous publications (Duan and Choudhari, 2014; Duan *et al.*, 2016; Zhang *et al.*, 2017), with the computational domain size and grid resolution summarized in Table 4. L_x, L_y and L_z are the domain size in the streamwise, spanwise and wall-normal directions, respectively. Δx^+ and Δy^+ are the uniform grid spacing in the streamwise and spanwise directions, respectively; Δz_{min}^+ and Δz_{max}^+ denote the minimum and maximum wall-normal grid spacing. The grid resolutions are normalized by the viscous length z_τ at the location where the turbulence statistics are gathered. N_f is the number of fields used to accumulate statistics, and

(a) M8Tw048

(b) M14Tw018
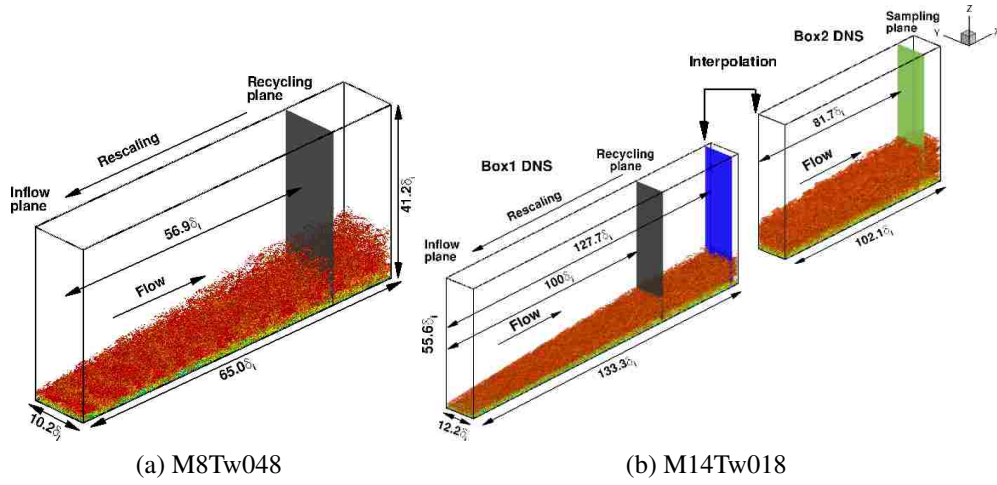
Figure 1. Computational domain and simulation setup for DNS of Mach 8 and Mach 14 turbulent boundary layers, with flow conditions representative of the nozzle exit of the Sandia Hypersonic Wind Tunnel at Mach 8 and the AEDC Hypervelocity Tunnel No. 9 at Mach 14, respectively.

T_f is the time spanned by those fields. The values of δ_i, z_τ, u_τ, and δ for each case is listed in Tables 1 and 2. δ_i corresponds to that of Box 1 in Case M14Tw018. The computational grid resolution inside the boundary layer is comparable to those reported in the literature in the context of previous simulations of turbulent wall-bounded flows using comparable numerical algorithms (Duan *et al.*, 2010, 2011, 2014, 2016; Zhang *et al.*, 2017, Jan. 2016). The effect of spanwise domain size on flow statistics is monitored by sufficient decay of two-point correlations and/or by comparing to cases with an auxiliary simulation of the same grid resolution but with a narrower span, and negligible difference is observed in the flow statistics of interest. Furthermore, the physical realism and accuracy of the computed flow fields have been validated by comparing to experimental results at similar flow conditions (Duan *et al.*, Jan. 2018, 2016). Additional comparisons of DNS results with both experiments and other high-quality simulations are presented in the following sections.

In the following sections, averages are first calculated over a streamwise window ($[x_a - 0.9\delta_i, x_a + 0.9\delta_i]$) and the spanwise direction for each instantaneous flow field; then, an ensemble average over N_f flow-field snapshots spanning a time interval of $T_f u_\tau / \delta$ is

calculated. Statistical convergence is verified by calculating averages over varying stream-wise window sizes or over a different number of snapshots and by making sure that the differences in flow statistics are negligible (<1%) among the different data-averaging techniques. Throughout the paper, statistics are reported based on fluctuations either around the standard (Reynolds) averages or around density-weighted (Favre) averages. For Mach numbers as high as 13.64, only small differences (< 3%) have been found between the standard and density-weighted (Favre) averages for the statistics reported in this article.

Table 4. Grid resolution and domain size for the direct numerical simulations. Part 1.

Case	$N_x \times N_y \times N_z$	L_x/δ_i	L_y/δ_i	L_z/δ_i	Δx^+	Δy^+	Δz^+_{min}	Δz^+_{max}
M2p5	$1760 \times 800 \times 400$	57.2	15.6	41.0	9.2	5.5	0.60	9.5
M6Tw025	$2400 \times 400 \times 560$	91.7	8.8	57.5	6.4	3.7	0.46	4.8
M6Tw076	$1600 \times 800 \times 500$	58.7	15.7	39.7	9.6	5.1	0.51	5.3
M8Tw048	$3200 \times 500 \times 600$	65.0	10.2	41.2	5.4	5.4	0.55	5.6
M14Tw018-1	$2500 \times 460 \times 540$	133.3	12.2	55.6	9.4	4.7	0.47	5.2
M14Tw018-2	$2000 \times 460 \times 786$	102.1	12.2	55.6	9.4	4.7	0.47	5.7

Table 5. Grid resolution and domain size for the direct numerical simulations. Part 2.

Case	$N_x \times N_y \times N_z$	N_f	$T_f u_\tau/\delta$
M2p5	$1760 \times 800 \times 400$	282	14.9
M6Tw025	$2400 \times 400 \times 560$	312	7.3
M6Tw076	$1600 \times 800 \times 500$	153	7.3
M8Tw048	$3200 \times 500 \times 600$	248	5.7
M14Tw018-1	$2500 \times 460 \times 540$	–	–
M14Tw018-2	$2000 \times 460 \times 786$	137	1.4

3. COMPUTATIONAL RESULTS

3.1. COMPRESSIBILITY TRANSFORMATIONS

In this section, the DNS database is used to gauge the performance of several velocity and temperature scalings. Complementary to the previous studies of Duan et al. (Duan *et al.*, 2010, 2011), the present study pays special attention to the recently proposed scaling

relations (Patel *et al.*, 2015; Trettel and Larsson, 2016; Zhang *et al.*, 2014) that have not yet been scrutinized in the high-Mach-number, cold-wall regime, in addition to the classical scalings according to Morkovin.

Figures 2 and 3 plot the Van Driest transformed mean velocity u_{VD}^+, which is defined as

$$u_{VD}^+ = \frac{1}{u_\tau} \int_0^{\overline{u}} (\overline{\rho}/\overline{\rho}_w)^{1/2} \, d\overline{u}. \tag{1}$$

The mean velocity shows an approximately logarithmic region where $u_{VD}^+ = \frac{1}{k} \log(z^+) + C_{VD}$ upon Van Driest transformation. The Van Driest transformed mean velocity shows a decrease in the mean slope S_{VD} in the linear viscous sublayer with higher wall cooling rate $-B_q$. A similar trend was reported in previous studies of Refs. (Duan *et al.*, 2010; Modesti and Pirozzoli, 2016; Shadloo *et al.*, 2015; Wu *et al.*, 2016; Zhang *et al.*, 2017). The log-layer intercept C_{VD} slightly increases with wall-cooling rate and Reynolds number, although the change seems to be less rapid in comparison with the results for compressible channel flows with cooled walls (Coleman *et al.*, 1995; Foysi *et al.*, 2004; Trettel and Larsson, 2016) and a turbulent boundary layer at Mach 4.5 (Maeder, 2000). Here, we use the semilocal Reynolds number Re_τ^* as a characteristic Reynolds number for comparing C_{VD} among the different DNS cases, since Re_τ^* is known from Patel et al. (Patel *et al.*, 2015) to be the governing parameter for wall turbulence statistics with different mean density and viscosity profiles, at least for wall turbulence at lower Mach numbers.

An alternative transformation of mean velocity was proposed by Trettel and Larsson (Trettel and Larsson, 2016) for compressible wall turbulence with cold walls, based on arguments about log-layer scaling and near-wall momentum conservation. The velocity scaling is defined as

$$u_{TL}^+ = \int_0^{u^+} \left(\frac{\bar{\rho}}{\rho_w} \right)^{1/2} \left[1 + \frac{1}{2} \frac{1}{\bar{\rho}} \frac{d\bar{\rho}}{dz} z - \frac{1}{\bar{\mu}} \frac{d\bar{\mu}}{dz} z \right] du^+. \tag{2}$$
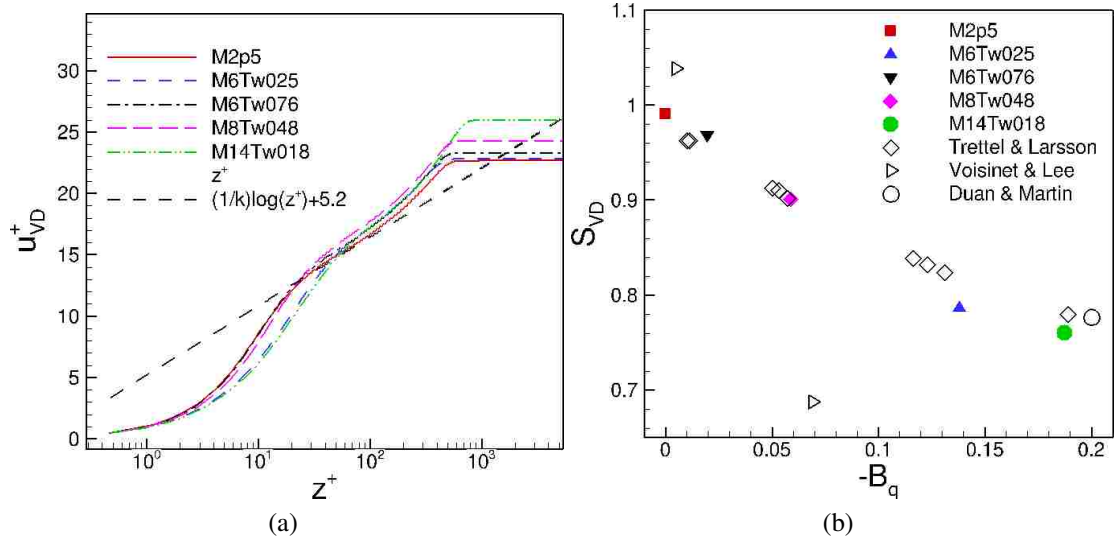
Figure 2. Effect of applying the Van Driest transformation to the mean velocity profile. Part 1.

Figures 4 and 5 shows a much improved collapse within the viscous sublayer region of the computational datasets when the modified velocity u_{TL}^+ is used for comparison. The open diamonds denote the results for compressible turbulent channels by Trettel and Larsson (Trettel and Larsson, 2016). Furthermore, the sublayer slope S_{TL} of the transformed velocity is nearly constant at different wall-cooling rates. The collapse of u_{TL}^+ in the viscous sublayer is not unexpected, since the velocity transformation of Trettel and Larsson (Trettel and Larsson, 2016) is designed to satisfy the stress-balance condition within the entire inner layer, including the viscous sublayer. In the log region, however, the log-law intercept C_{TL} of the transformed velocity u_{TL}^+ shows a similar scatter as that of the Van Driest transformed velocity at different wall-cooling rates and Reynolds numbers; and the value of C_{TL} for boundary layers is consistently larger than that for channel flows. The difference in the log-law intercept between boundary layers and channels may suggest an influence of the "wake" component on the log region for boundary layers. The lack of collapse in C_{TL} for boundary layers may also be due to the discrepancy in the characteristic Reynolds number Re_τ^* among the boundary layer DNS cases or a lack of an extended log-law region
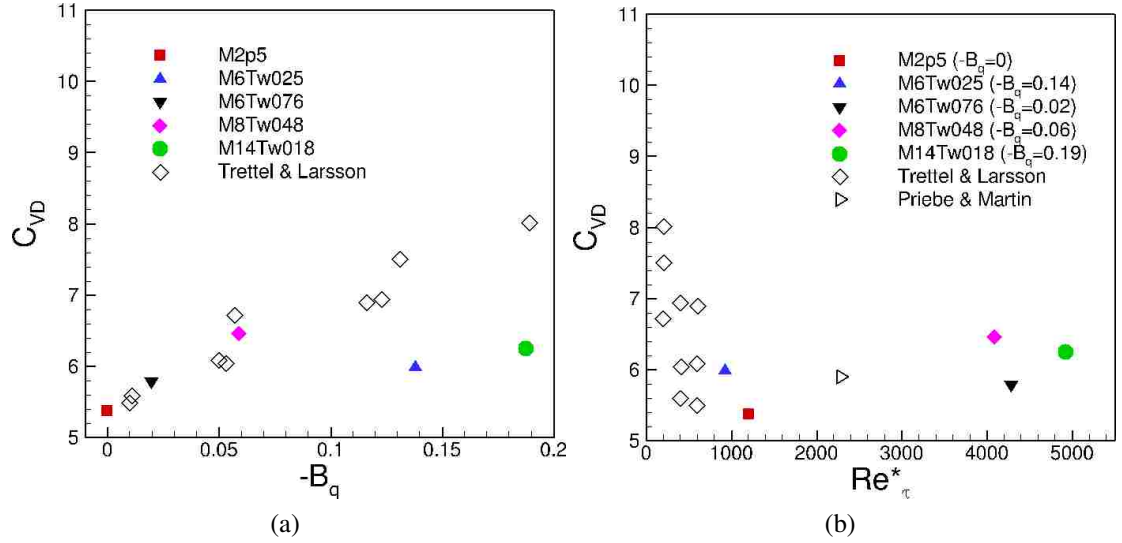
Figure 3. Effect of applying the Van Driest transformation to the mean velocity profile. Part 2.

for the existing boundary-layer datasets, making it difficult to accurately probe the log-law region. Although not shown here, a different mean velocity transformation proposed by Patel et al. (Patel *et al.*, 2016) based on Re_τ^* gives very similar results as that of Trettel and Larsson (Trettel and Larsson, 2016).

Figures 6 and 7 plot the wall-normal profiles of the turbulence intensities and the Reynolds shear stress. For comparison, experimental data by Williams et al. (Williams *et al.*, 2018) ($M_\infty = 7.5$, $Re_\tau = 279$, $T_w/T_r = 0.8$) and DeGraaff & Eaton (Degraaff and Eaton, 2000) ($M_\infty \approx 0$, $Re_\tau = 2220$) along with DNS data by Priebe & Martín (Priebe and Martín, June 2011) ($M_\infty = 7.2$, $Re_\tau = 233$, $T_w/T_r = 0.53$), Sillero et al. (Sillero *et al.*, 2013) ($M_\infty \approx 0$, $Re_\tau = 1310$), and Jiménez et al. (Jiménez *et al.*, 2010) ($M_\infty \approx 0$, $Re_\tau = 445$) are also plotted in this figures. In general, an apparently good collapse of the data across a wide range of Mach numbers is achieved via Morkovin's scaling (Morkovin, 1962), consistent with the experimental and computational observations of Refs. (Duan *et al.*, 2010, 2011; Peltier *et al.*, 2016; Williams *et al.*, 2018) at lower Mach numbers and/or without strong wall cooling. The wall-normal component of turbulence intensity and the Reynolds stress

Figure 4. Effect of applying the Trettel and Larsson (Trettel and Larsson, 2016) transformation to the mean velocity profile. Part 1.

measured by PIV (Williams *et al.*, 2018) exhibit reduced magnitude than those predicted by the various DNS at high Mach number. Such a reduction in magnitude is typical of particle-based velocimetry studies of supersonic flows (Williams *et al.*, 2018). Figures 8 and 9 further show that the peak locations of turbulence intensities and the Reynolds shear stress in the classical inner scaling (z^+) shift away from the wall with increasing wall-cooling rate. The semilocal scaling (z^*) of Huang et al. (Huang *et al.*, 1995) better collapses the location of the near-wall peak of turbulence intensities and the Reynolds shear stress. There is an apparent increase in the peak value of the Morkovin transformed streamwise turbulence intensity u'_{rms}/u^* as the freestream Mach number increases, which is consistent with the DNS of turbulent channel flows at bulk Mach numbers of 1.5 and 3 by Modesti & Pirozzoli (Modesti and Pirozzoli, 2016). A similar increase in the near-wall peak value with increasing Mach number is not observed for the spanwise and wall-normal turbulence intensities nor for the Reynolds shear stress. Away from the wall in the outer layer, the semilocal scaling appears to exaggerate the discrepancy among the different cases, while the outer scaling (z/δ) would better collapse the data as suggested in Figure 6.
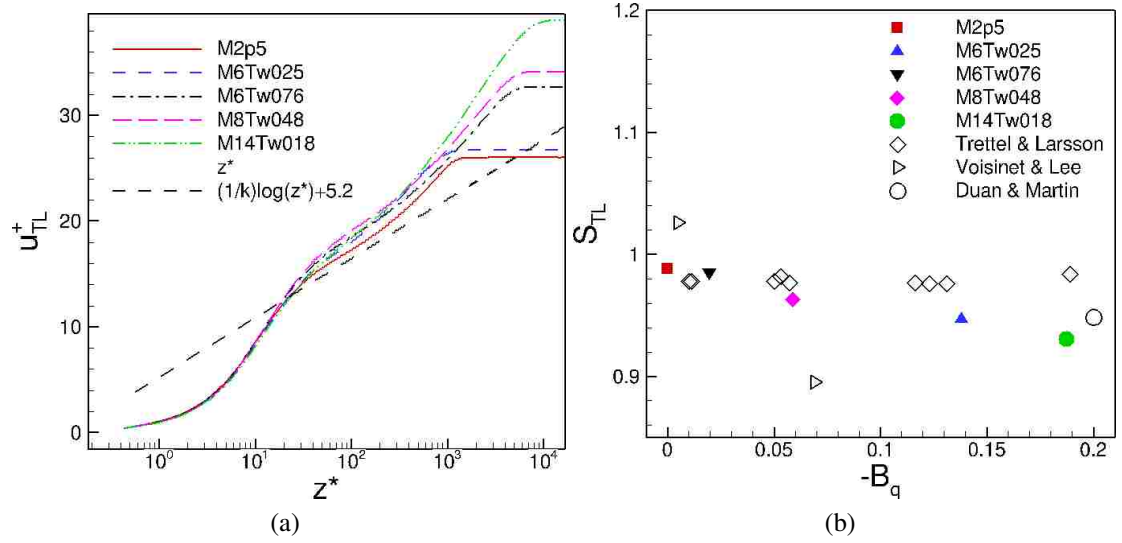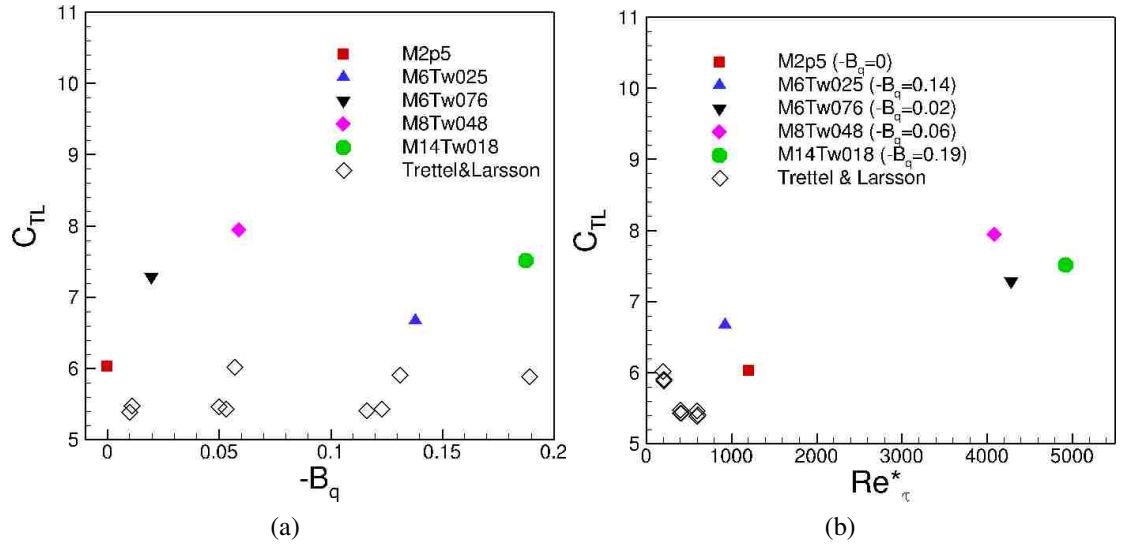
Figure 5. Effect of applying the Trettel and Larsson (Trettel and Larsson, 2016) transformation to the mean velocity profile. Part 2.

The vorticity fluctuation components are presented in Figures 10a and 10b, scaled in wall units and semilocal units, respectively. Variable in wall units are normalized by u_τ / z_τ, and variables in semilocal units are normalized by u^* / z_τ^*. For comparison, the DNS data by Bernardini and Pirozzoli (Bernardini and Pirozzoli, 2011) ($M_\infty = 4$, $T_w / T_r = 1$, $Re_\tau = 500$) is also plotted in Figure 10a. Excellent comparison in vorticity fluctuations is achieved between Case M2p5 of the current DNS and the DNS of Bernardini and Pirozzoli (Bernardini and Pirozzoli, 2011) at Mach 4 with an adiabatic wall.

The semilocal scaling yields a much improved collapse of vorticity fluctuation distributions among the DNS cases in most parts of the boundary layer, although notable differences exist in $z^* \lesssim 10$ for the spanwise vorticity component and in $z^* \lesssim 30$ for the streamwise and wall-normal components. Since the vorticity fluctuations are largely induced by small scale turbulence motions, the better collapse of vorticity profiles among the various DNS cases with semilocal scaling may indicate that the small scale motions are dictated by local mean flow conditions in terms of the mean density and the mean viscosity. A similar observation has been made by Modesti and Pirozzoli (Modesti and Pirozzoli, 2016)

(a) Streamwise

(b) Spanwise

(c) wall-normal

Figure 6. Turbulence intensities transformed according to Morkovin as a function of wall-normal distance z/δ, where $u^* = u_\tau \sqrt{\overline{\rho_w}/\overline{\rho}}$ is the Morkovin transformed velocity scale.
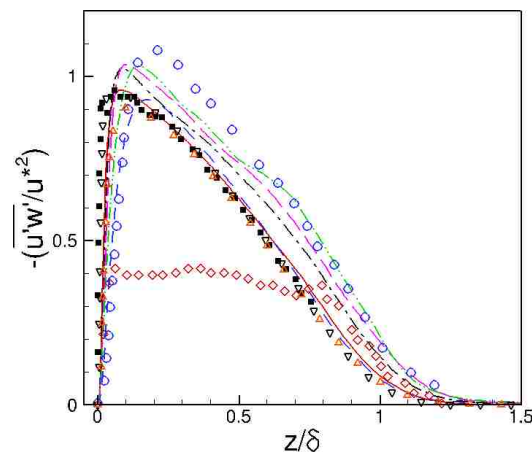
Figure 7. Reynolds shear stress transformed according to Morkovin as a function of wall-normal distance z/δ, where $u^* = u_\tau \sqrt{\overline{\rho_w}/\overline{\rho}}$ is the Morkovin transformed velocity scale.
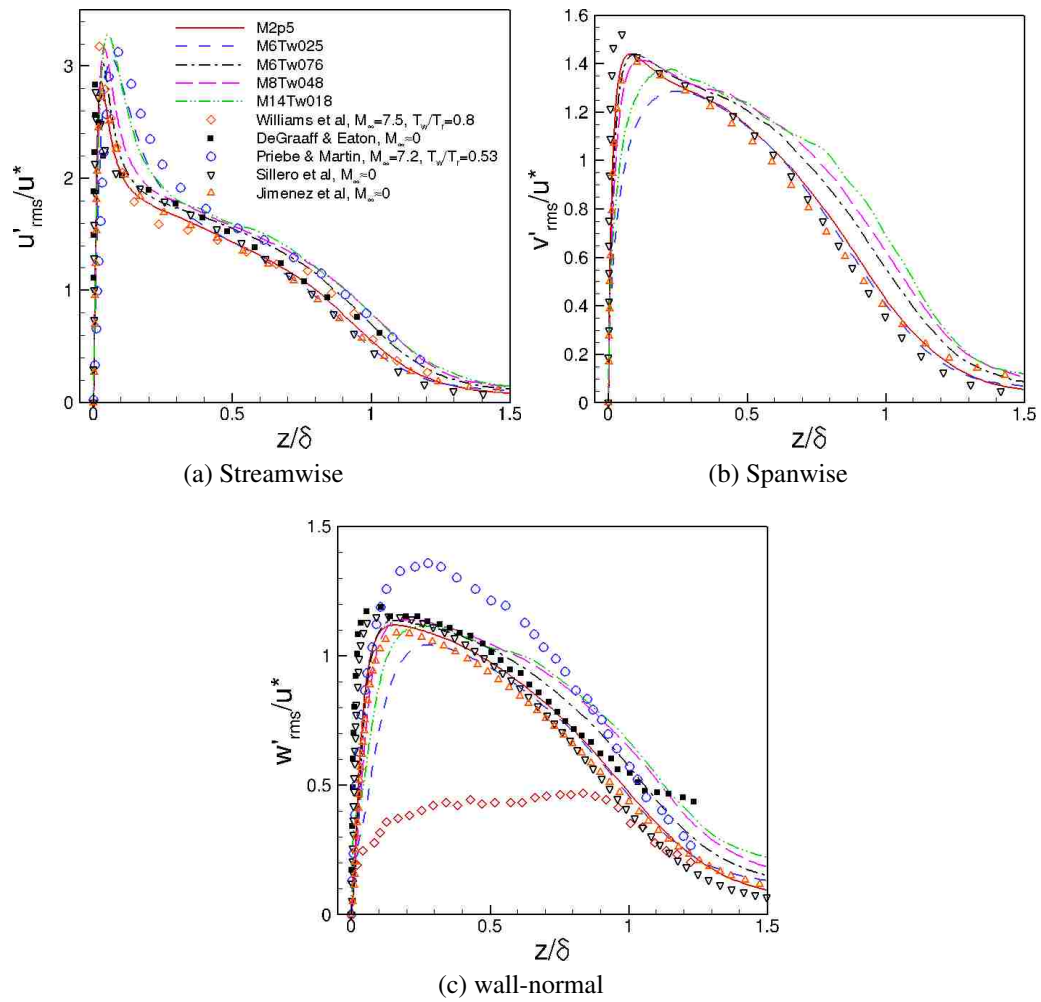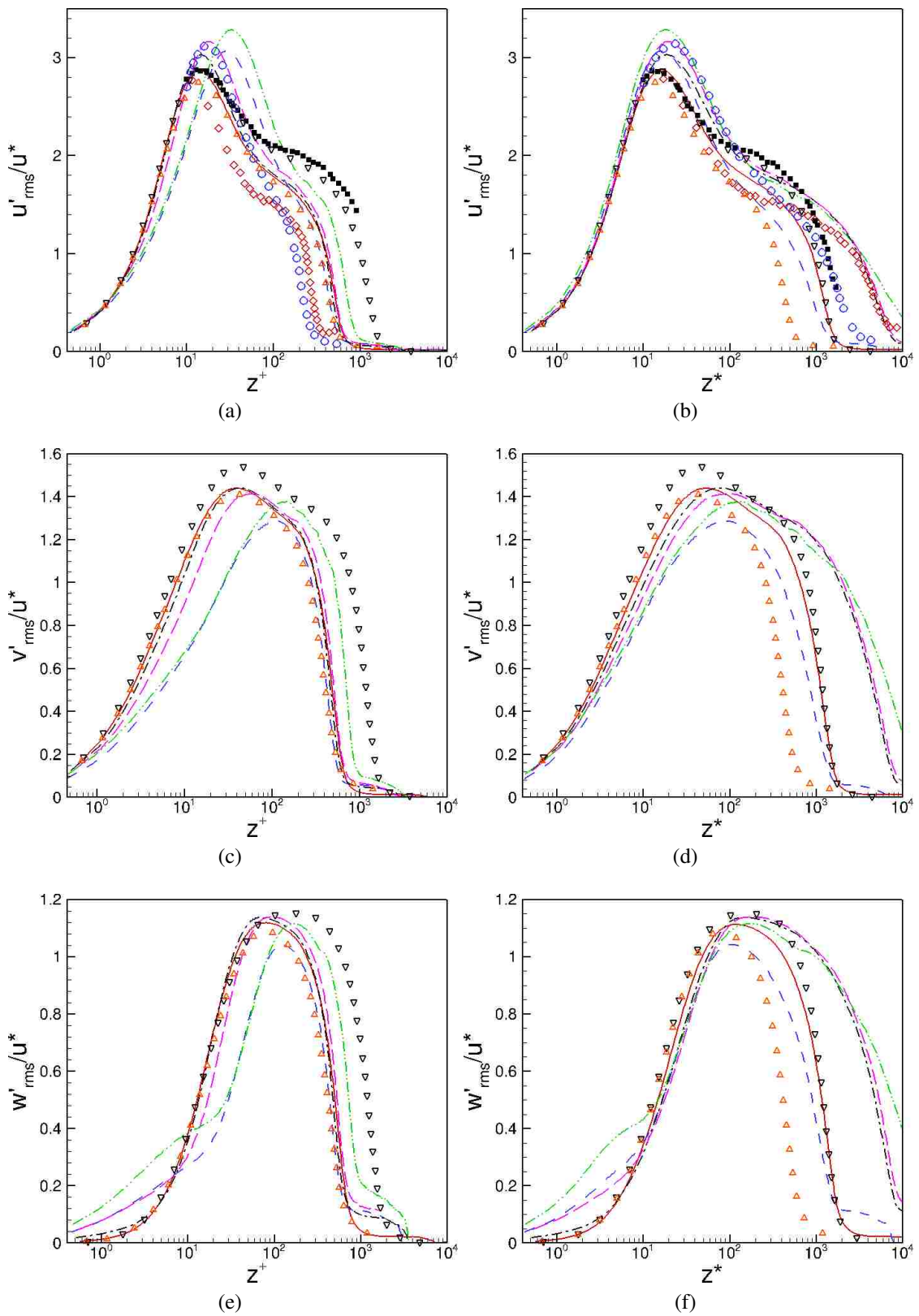
Figure 8. Turbulence intensities transformed according to Morkovin in (a,c,e) classical inner scaling and (b,d,f) semilocal scaling.
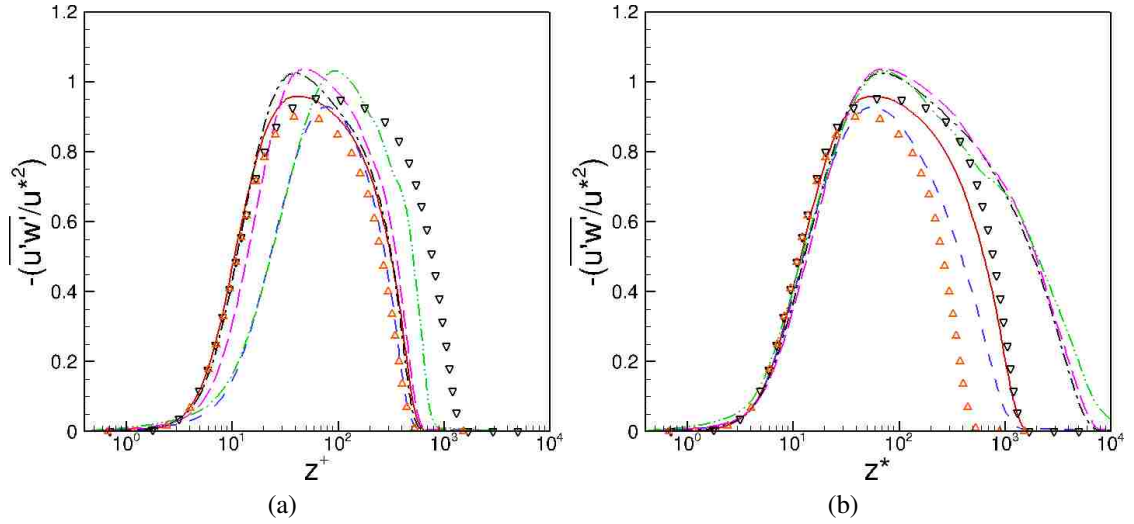
Figure 9. Reynolds shear stress transformed according to Morkovin in (a) classical inner scaling and (b) semilocal scaling.

in their DNS study of compressible isothermal channel flow at bulk Mach numbers of 1.5 and 3. Furthermore, the differences in semilocally scaled vorticity fluctuations $\omega'_{i,rms} z^*_\tau / u^*$ within the near-wall region among the various DNS cases may be due to wall temperature effects that cause a change in turbulence anisotropy, as a similar variation in the near-wall vorticity fluctuations has also been reported by Patel et al. (Patel *et al.*, 2016) in the context of zero-Mach-number channel flows with different surface heat transfer rates. The changes in turbulence anisotropy in the near-wall region is also indicated by Figure 16 in Section 3.3.

As far as the coupling between thermal and velocity fields is concerned, Figure 11 plots the mean temperature as a function of the mean velocity for the two highest Mach number DNS cases (M8Tw048 and M14Tw018). Figure 11a shows the classical relation of Walz (Walz, 1969): $\frac{\bar{T}}{T_\infty} = \frac{T_w}{T_\infty} + \frac{T_r - T_w}{T_\infty} \left(\frac{\bar{u}}{U_\infty} \right) + \frac{T_\infty - T_r}{T_\infty} \left(\frac{\bar{u}}{U_\infty} \right)^2$; Figure 11b shows the generalized relation of Zhang et al. (Zhang *et al.*, 2014): $\frac{\bar{T}}{T_\infty} = \frac{T_w}{T_\infty} + \frac{T_{rg} - T_w}{T_\infty} \left(\frac{\bar{u}}{U_\infty} \right) + \frac{T_\infty - T_{rg}}{T_\infty} \left(\frac{\bar{u}}{U_\infty} \right)^2$, where $T_{rg} = T_\infty + r_g U_\infty^2 / (2C_p)$ and $r_g = 2C_p(T_w - T_\infty)/U_\infty^2 - 2Pr q_w / (U_\infty \tau_w)$.
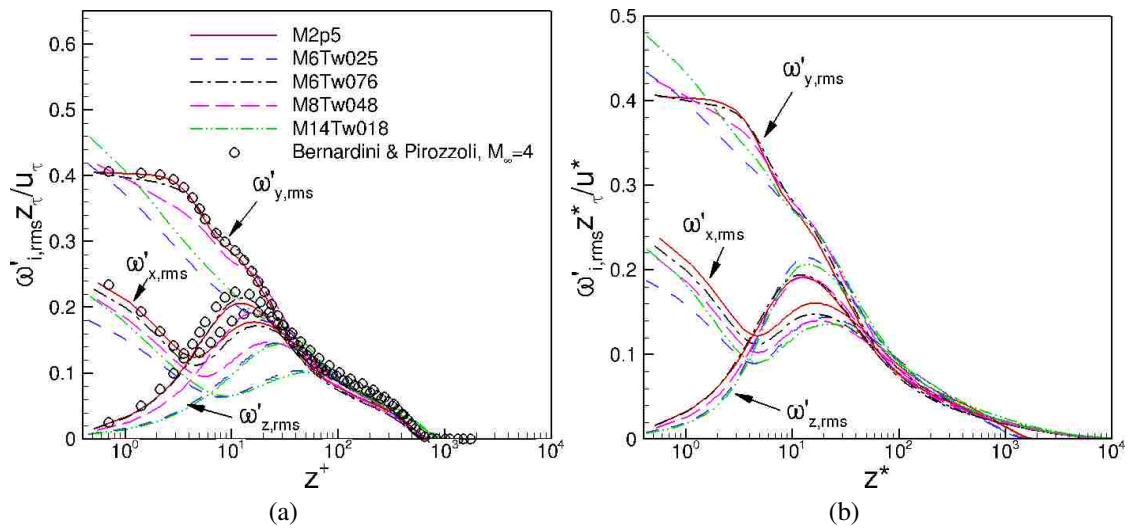
Figure 10. Wall-normal distribution of vorticity fluctuations nondimensionalized by (a) wall units and (b) semilocal units, respectively.
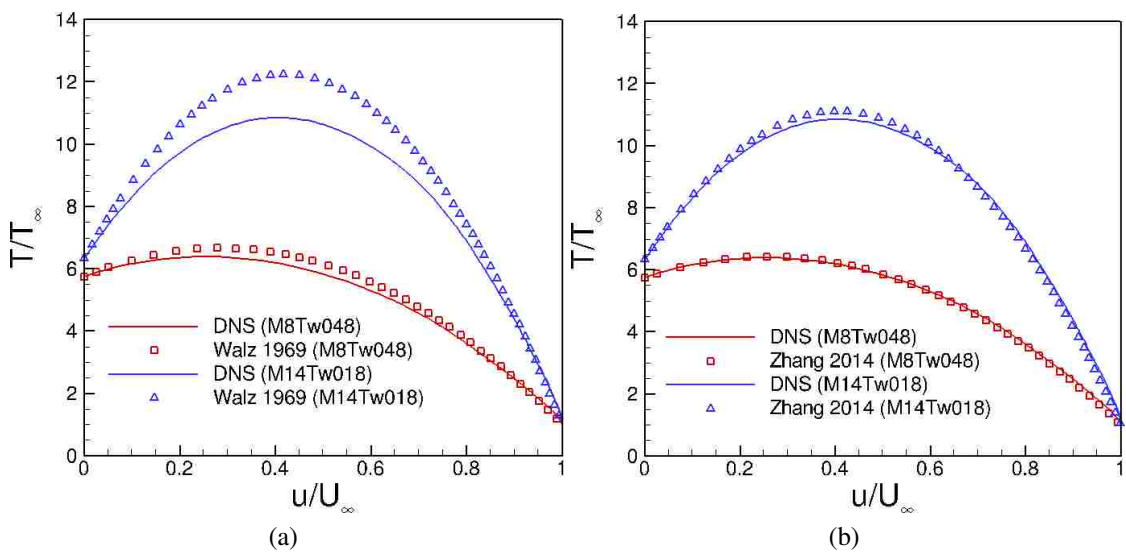
Figure 11. Relation between mean temperature and mean velocity.

The DNS results are compared with the classical relation of Walz (Walz, 1969) and a modified relation of Zhang et al. (Zhang *et al.*, 2014). The Walz relation compares reasonably well with the DNS data for case M8Tw048, while a significantly larger deviation from DNS exists for case M14Tw018. The modified version of Zhang et al. (Zhang *et al.*, 2014), which explicitly accounts for the finite wall heat flux, leads to a much improved comparison with the DNS at Mach numbers as high as 14.

Figure 12 shows that the turbulent Prandtl number Pr_t and the modified SRA of Huang et al. (Huang *et al.*, 1995) across the boundary layer. The Huang's SRA (HSRA) relates the temperature fluctuations T'_{rms} to the streamwise velocity fluctuations u'_{rms} as given by

$$\frac{T'_{rms}/\overline{T}}{(\gamma-1)M^2(u'_{rms}/\overline{u})} = \frac{1}{Pr_t(1-(\partial\overline{T}_t/\partial\overline{T}))}. \tag{3}$$

The results from Figure 12 suggest that both Pr_t and HSRA are insensitive to the freestream Mach number and the wall temperature conditions, with values close to unity in most of the outer region of the boundary layer. Although not shown here, a different modified SRA recently proposed by Zhang et al. (Zhang *et al.*, 2014) gives marginally improved prediction compared to HSRA for $z/\delta < 0.8$. The temperature-velocity scalings as high as Mach 13.64 are generally consistent with the predictions from several previous studies at lower Mach numbers (Duan *et al.*, 2010; Shadloo *et al.*, 2015; Zhang *et al.*, 2014).

3.2. THERMODYNAMIC PROPERTIES

In this section, several thermodynamic fluctuations and their dependence on Mach number and wall temperature conditions are presented. Thermodynamic fluctuations, especially the density fluctuations, appear in many unclosed terms in the Reynolds-averaged Navier-Stokes (RANS) equations, the knowledge of which is thus useful for turbulence modeling.
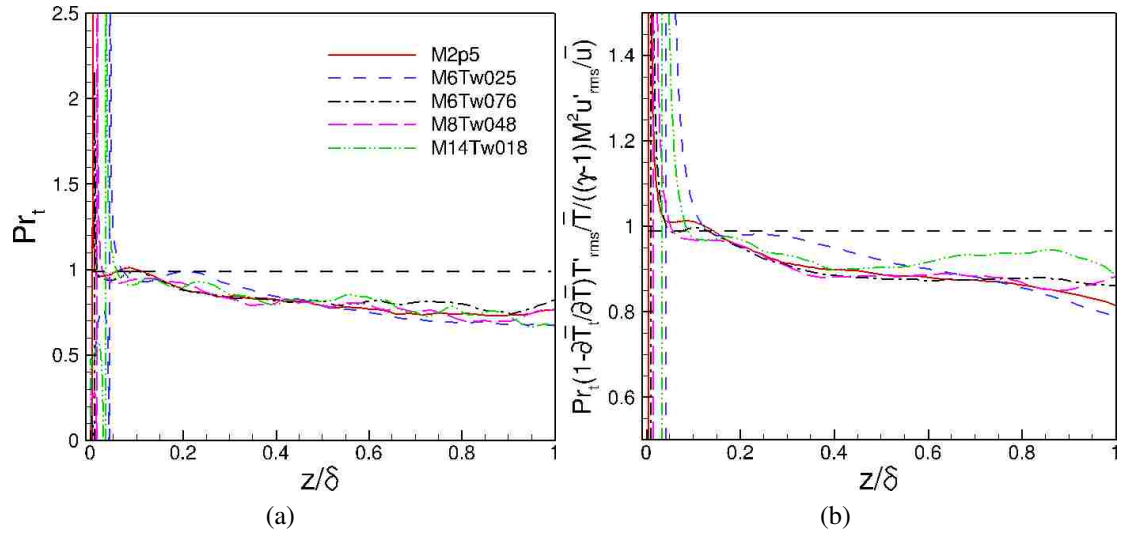
Figure 12. (a) Turbulent Prandtl number and (b) Huang's modified SRA as a function of wall-normal distance.

Figures 13a and 13b plot the simulation results of the wall-normal variation of the fluctuating Mach number M'_{rms}, with the wall-normal distance nondimensionalized by wall units and semilocal units, respectively. The fluctuating Mach number increases dramatically with the freestream Mach number, and such an increase cannot be accounted for with the semilocal scaling. At Mach 7.87 and 13.64, the fluctuating Mach number develops a strong peak with a peak value greater than one toward the edge of the boundary layer. As a result, the turbulent fluctuations become locally supersonic relative to the surrounding flow, likely creating local shocklets that may be the source of significant dilatational dissipation and entropy production. Figures 14a and 14b further show that the peak of M'_{rms} at the boundary layer edge is associated with the strong local fluctuations of density and temperature. The sharp gradients of the density and temperature at the boundary layer edge may be connected with the turbulent-non-turbulent interface or the edge of the turbulent bulges as illustrated in Figure 15. The contours are those of numerical schlieren, with density gradient contour levels selected to emphasize large scale motions of the boundary layer. The location of the y-z plane is indicated by the vertical dashed line. Unlike the r.m.s. profiles
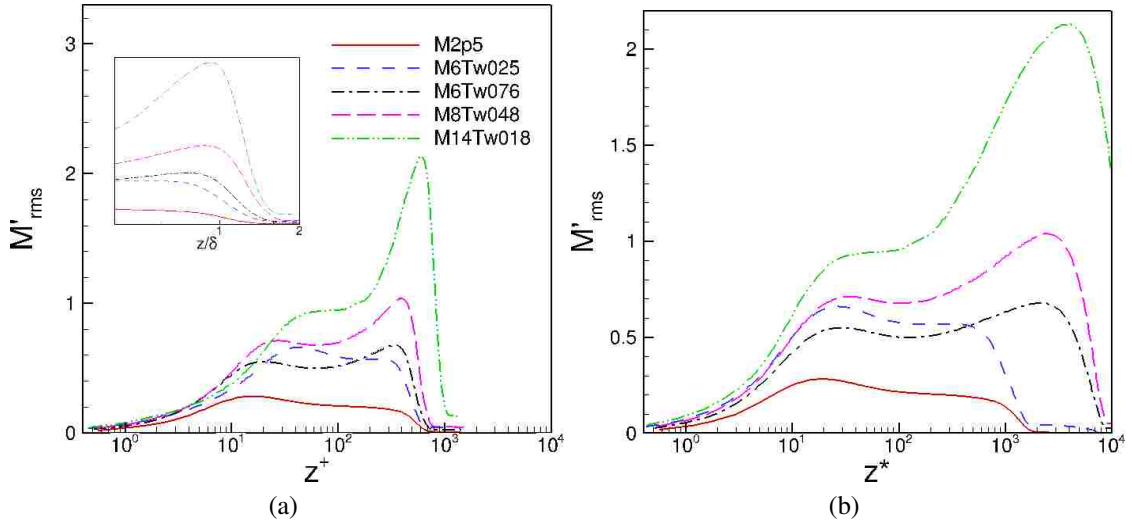
Figure 13. Wall-normal distribution of fluctuating Mach number for various Mach number cases, with the wall-normal distance nondimensionalized by (a) wall units and (b) semilocal units.

of density and temperature from Figures 14a and 14b, the profile of r.m.s. pressure fluctuations (Figure 14c) does not exhibit a strong peak near the edge of the boundary layer. The different behavior of the density and temperature fluctuations in comparison with the pressure fluctuations as well as the similarity in the density and temperature magnitudes near the edge of the boundary layer may be indicative of the local importance of the entropic mode. Indeed, as shown by Figure 14d, the entropy fluctuation profile exhibits a local peak near the boundary layer edge, similar to that of density and temperature fluctuations. The peak in entropy may be the result of enhanced heat conduction due to rapid variation in unsteady temperature profile that acts as a strong local source of entropy spots. The entropy fluctuations decay rapidly outside the boundary layer. For $z/\delta \gtrapprox 1.6$, the acoustic mode becomes dominant due to "eddy-Mach-wave" radiation from the boundary layer (Laufer, 1964). The acoustic radiation increases significantly with increasing freestream Mach number as reported in Refs. (Duan *et al.*, 2014, 2016; Zhang *et al.*, 2017).
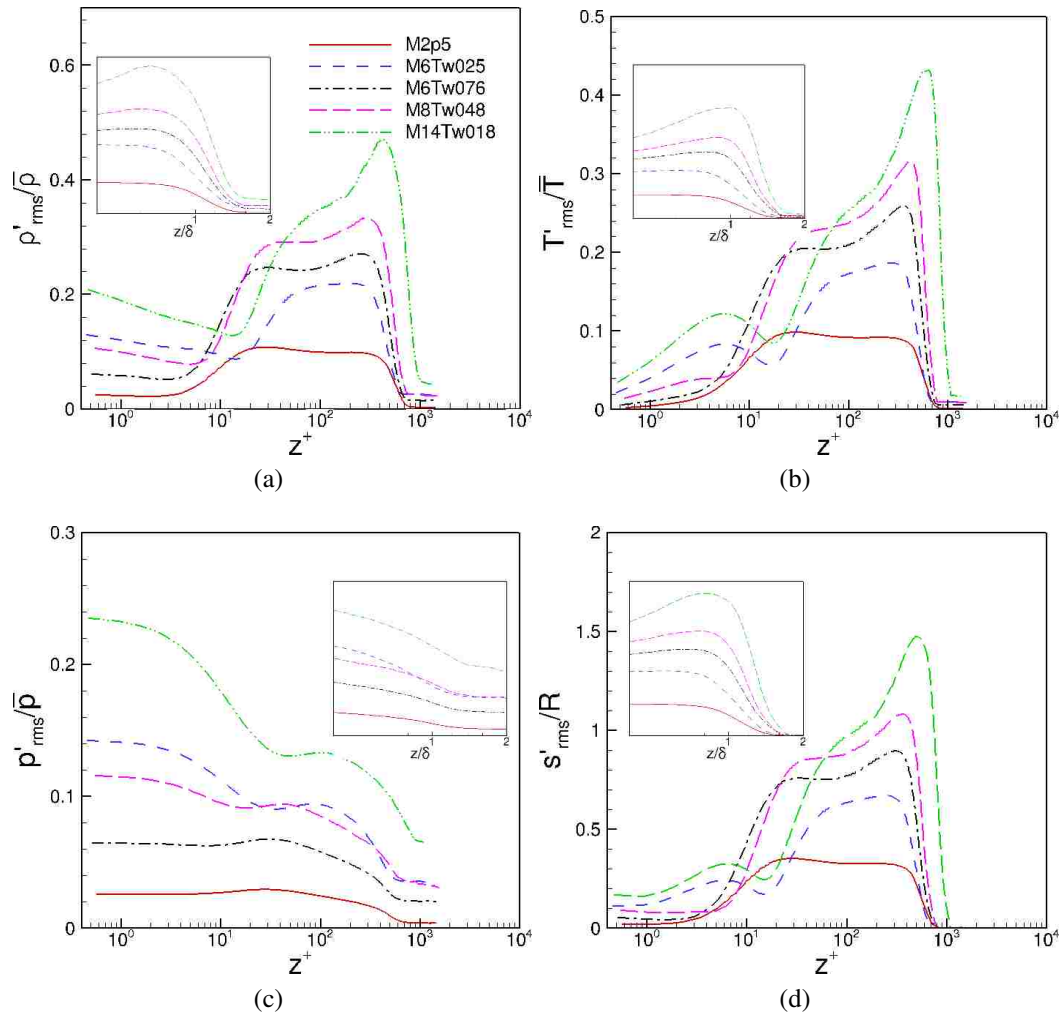
Figure 14. Wall-normal distribution of the r.m.s. fluctuations of (a) density, (b) temperature, (c) pressure, and (d) entropy for various Mach number cases.
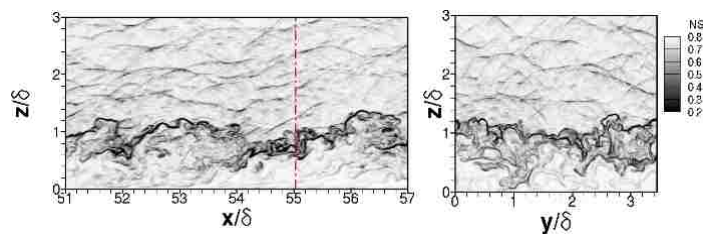
Figure 15. Visualization of a typical instantaneous flow field for Case M14Tw018 in a streamwise wall-normal (*x*-*z*) plane and a spanwise wall-normal (*y*-*z*) plane.
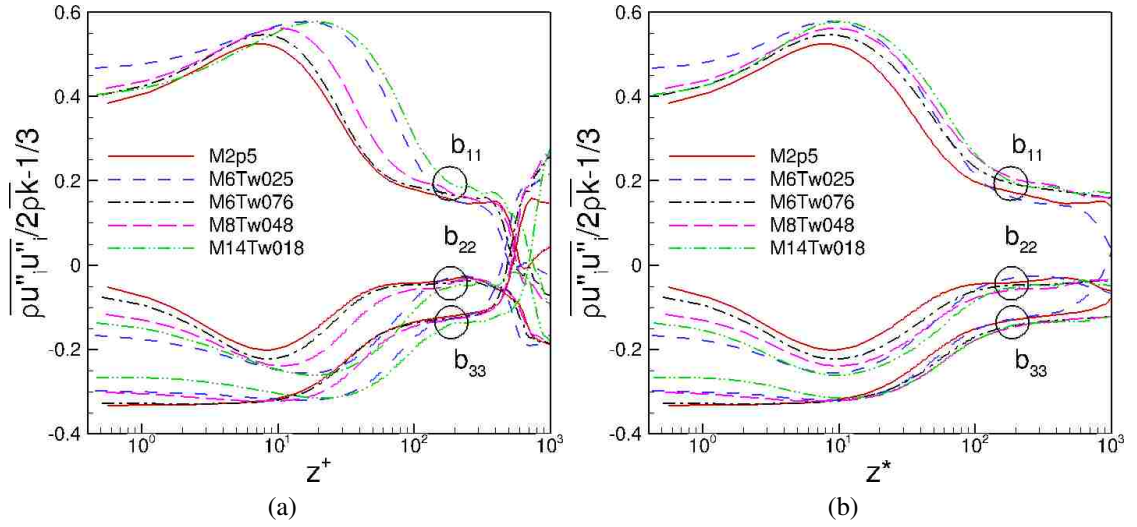
Figure 16. Distributions of normal Reynolds stress anisotropies.

3.3. REYNOLDS STRESS ANISOTROPY

Figures 16 and 17 plot the Reynolds stress anisotropy for the various Mach number cases. Open circles are used to group the various cases for each normal stress component in (a) and (c), and hence, to make the profiles for different components easier to distinguish from each other. The anisotropy tensor is defined as $b_{ij} = \overline{\rho u_i'' u_j''}/2\overline{\rho k} - \delta_{ij}/3$. The anisotropy tensor is defined as

$$b_{ij} = \frac{\overline{\rho u_i'' u_j''}}{2\overline{\rho k}} - \frac{1}{3}\delta_{ij}. \tag{4}$$

The semilocal scaling is successful in collapsing the near-wall peak locations of the normal and shear stress anisotropies among the DNS cases. Of the three normal components of anisotropy, the streamwise component b_{11} increases with increasing Mach number and wall cooling for $z^* \gtrapprox 10$, while the opposite is seen for the spanwise component b_{22}. As discussed by Patel et al. (Patel *et al.*, 2016, 2015) and Duan et al. (Duan *et al.*, 2010), the increase in b_{11} with increasing Mach number and wall-cooling rate may indicate a decrease in the redistribution of turbulent energy from the streamwise direction to the other
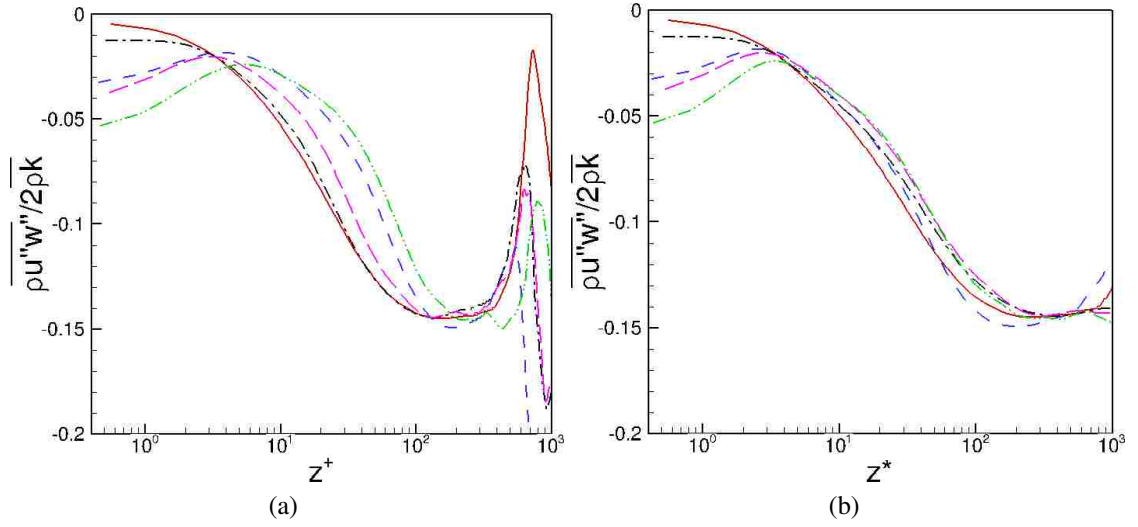
Figure 17. Distributions of Reynolds shear stress anisotropy.

two directions when the Mach number and wall-cooling rate increase. The decreased re-distribution of turbulent energy is also consistent with the increased peak value of u'_{rms}/u^* (Figure 8b) when the Mach number and wall cooling rate are increased.

Compared with b_{11} and b_{22}, the wall-normal component of the normal stress anisotropy, b_{33}, and the Reynolds shear stress anisotropy, b_{13}, are less sensitive to Mach number and wall-cooling conditions, with the influence of Mach number and wall cooling limited to $z^* \lessapprox 10$.

3.4. TURBULENT KINETIC ENERGY BUDGET

The turbulent kinetic energy (TKE) for a compressible boundary layer is given by

$$\frac{D(\overline{\rho}\tilde{k})}{Dt} = P + TT + \Pi - \phi + D + ST \tag{5}$$

with

$$P = -\overline{\rho u_i'' u_k''} \frac{\partial \widetilde{u}_i}{\partial x_k}$$

$$TT = -\frac{\partial}{\partial x_k}(\frac{1}{2}\overline{\rho u_i'' u_i'' u_k''})$$

$$\Pi = \Pi^t + \Pi^d = -\frac{\partial}{\partial x_i}(\overline{p'u_i''}) + \overline{p'\frac{\partial u_i''}{\partial x_i}}$$

$$\phi = \overline{\tau_{ik}'\frac{\partial u_i''}{\partial x_k}}$$

$$D = \frac{\partial}{\partial x_k}(\overline{\tau_{ik}'' u_i''})$$

$$ST = \overline{u_i''}(\frac{\partial \overline{\tau}_{ik}}{\partial x_k} - \frac{\partial \overline{p}}{\partial x_i}) - \overline{\rho}\widetilde{k}\frac{\partial \widetilde{u}_k}{\partial x_k}$$

(6)

where P is the production term, TT is the turbulent transport term, Π is the pressure term (pressure diffusion and pressure dilatation), $-\phi$ is viscous dissipation per unit volume, D is viscous diffusion, and ST represents additional terms that arise when density is not constant. Figure 18 plots the terms in the TKE budget, normalized by the conventional inner scaling (Figure 18a) and the 'semilocal' scaling (Figure 18b). Variables in wall units are normalized by $\bar{\rho}_w u_\tau^3/z_\tau$, and variables in semilocal units are normalized by $\bar{\rho}u^{*3}/z_\tau^*$. Solid lines: M2p5; Dashed lines: M6Tw025; Dash-Dot lines: M6Tw076; Long Dash lines: M8Tw048; Dash-Dot-Dot lines: M14Tw018. The additional terms arising due to density variation (ST) have a negligible variation compared to the other terms and are thus excluded from the Figure. Overall, the semilocal scaling yields a significantly better collapse of the budget terms among the different Mach number cases in comparison with the inner scaling. Such a finding is consistent with the previous study by Duan et al. (Duan *et al.*, 2010, 2011) based on temporal DNS of turbulent boundary layers up to Mach 12. Figures 19 and 20 further shows that the semilocal scaling largely collapses the terms associated with turbulence production, turbulence transport, pressure terms, and viscous diffusion and dissipation. Notable differences among the different cases are confined to the inner region with $z^* \lessapprox 5$. The production term shows a near-wall peak in the buffer layer at $z^* \approx 12$ with a slight
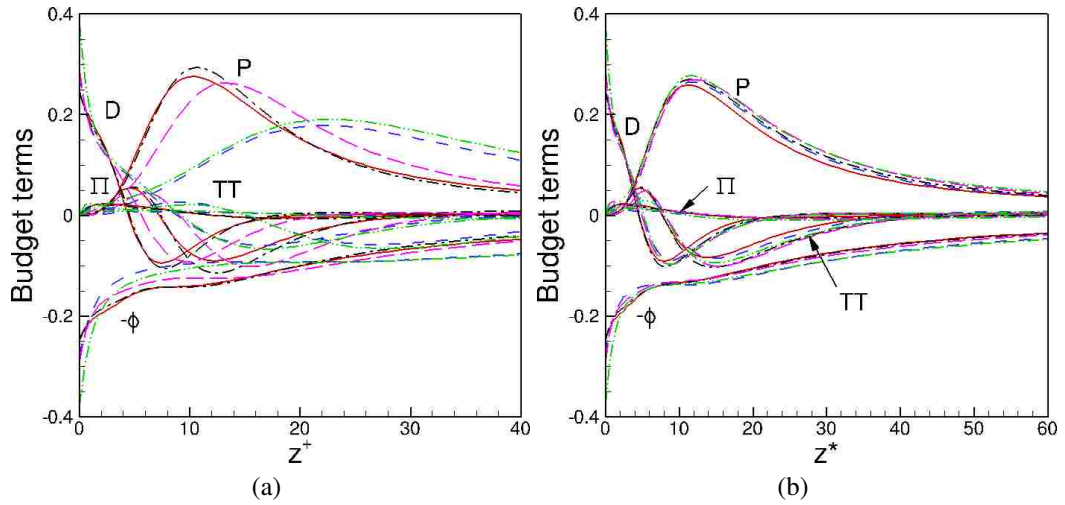
Figure 18. TKE budget for different cases nondimensionalized by (a) wall units and (b) semilocal units, respectively.

increase in the peak value as the Mach number increases. The collapse of the near-wall peak in the buffer layer and the increase in the peak value with Mach number are consistent with those of the Morkovin-transformed streamwise turbulence intensity u'_{rms}/u^*.

The effects of compressibility on the dissipation have been of interest in the context of compressible turbulence models (Sarkar *et al.*, 1991; Wilcox, 2006; Zeman, 1990). The dissipation can be expanded into solenoidal dissipation ϕ_s and dilatational dissipation ϕ_d, after neglecting terms that involve viscosity fluctuations and the term due to inhomogeneity (Guarini *et al.*, 2000; Huang *et al.*, 1995). Figure 21 plots the wall-normal variation in solenoidal and dilatational components of the dissipation rate. The solenoidal dissipation ϕ_s normalized with semilocal units is insensitive to Mach number and wall temperature conditions, except in the near-wall region of $z^* \lesssim 10$ (Figure 21a), while the dilatational dissipation increases significantly with increasing freestream Mach number or wall-cooling rate (Figure 21b). At $M_\infty = 13.64$, the dilatational dissipation ϕ_d becomes non-negligible compared with the solenoidal dissipation ϕ_s, with a maximal ratio of $\phi_d/\phi_s \approx 11\%$ in regions near the wall and close to the boundary-layer edge (Figure 21c). Both the dilatational dissipation and the solenoidal dissipation become insignificant near the boundary-
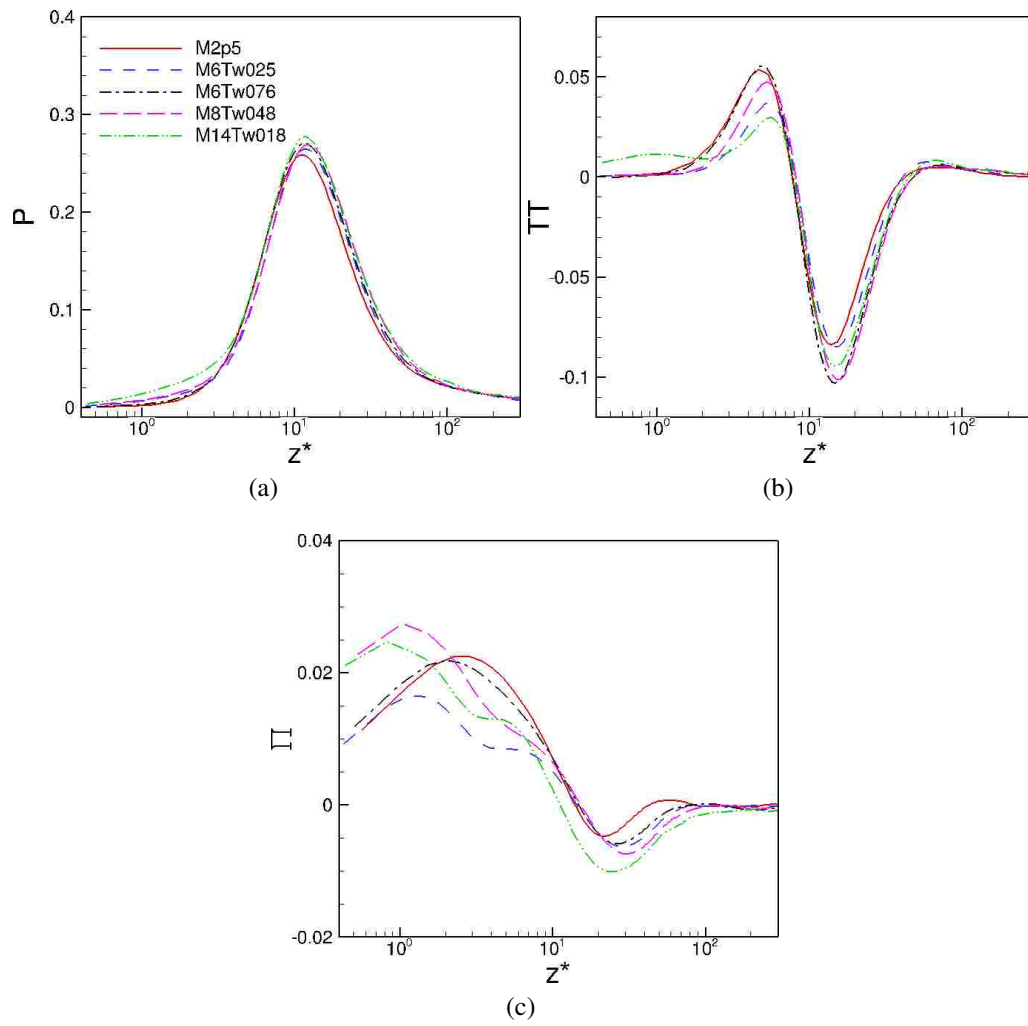
Figure 19. TKE budget terms for different cases normalized by $\bar{\rho}u^{*3}/z_\tau^*$. Part 1.
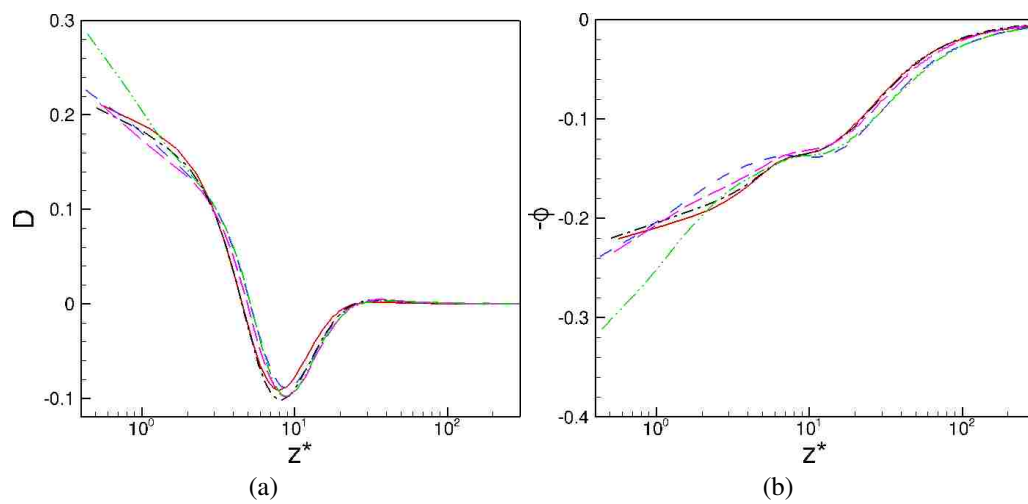
Figure 20. TKE budget terms for different cases normalized by $\bar{\rho}u^{*3}/z_\tau^*$. Part 2.

layer edge; the increase in the ratio of ϕ_d/ϕ_s toward the boundary layer edge is largely caused by a faster decay of the solenoidal dissipation compared to that of the dilatational dissipation. The small values of dilatational dissipation near the boundary-layer edge may suggest that the formation of shocklets, as indicated by strong localized density gradient in instantaneous flow visualizations (Figure 15) and the supersonic fluctuating Mach number (Figure 13a), is infrequent enough for the shocklets to have any appreciable influence on the dilatational dissipation, at least for the cases studied.

Finally, the effect of compressibility on the pressure terms is considered. The pressure terms for a compressible flow include pressure diffusion (Π^t), pressure dilatation (Π^d), and compressibility (Π^c), defined as

$$\Pi^t = -\frac{\partial}{\partial x_i}(\overline{p'u_i''}), \qquad \Pi^d = \overline{p'\frac{\partial u_i''}{\partial x_i}}, \qquad \Pi^c = -\overline{u_i''}\frac{\partial \overline{p}}{\partial x_i}. \tag{7}$$

Figures 22a and 22b show comparisons of pressure diffusion and pressure dilatation, respectively, among the various DNS cases. The pressure diffusion and pressure dilatation terms show a large Mach number and wall temperature dependence, especially in the near wall region ($z^* \lesssim 10$). The pressure dilatation Π^d increases with Mach number; and at Mach 13.64, the pressure dilatation term has significant contribution to the sum of the pressure terms in the wall region with $z^* \lesssim 10$ (Figure 22c). All the terms are normalized by $\bar{\rho}u^{*3}/z_\tau^*$. For comparison, the Zeman's compressibility correction (Zeman, Jan. 1993), defined as $\Pi^d = 0.02\gamma[1-\exp(-M_t^2/0.2)]\bar{\rho}\overline{u_i''}(\partial\bar{\rho}/\partial x_i)/\bar{\rho}$, is also plotted in Figure 22cc. The Zeman compressibility correction is insufficient for correcting Π^d for $z^* \lesssim 10$. However, it conforms well with the DNS farther away from the wall. Although not shown here, the traditional Sarkar-Zeman-Wilcox correction for free-shear flows (Sarkar *et al.*, 1991; Wilcox, 2006; Zeman, 1990) significantly overcorrects throughout the boundary layer when applied to the current DNS cases. The better match of Zeman's model with the DNS is consistent with the observation by Rumsey (Rumsey, 2010), who showed that Zeman's compressibil-
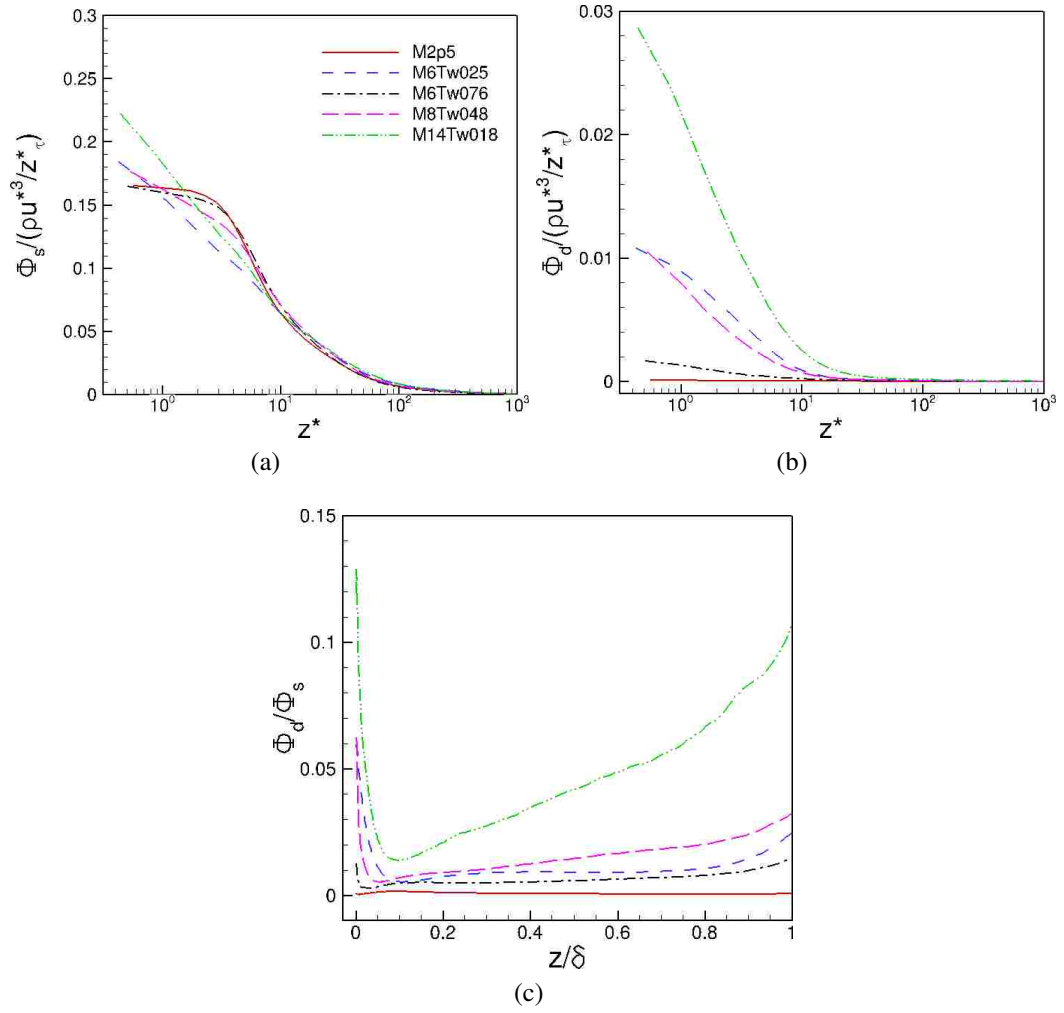
Figure 21. Plot of solenoidal dissipation $\phi_s = \bar{\mu}\overline{\omega_i'\omega_i'}$ and dilatational dissipation $\phi_d = \frac{4}{3}\bar{\mu}\overline{\frac{\partial u_i'}{\partial x_i}\frac{\partial u_k'}{\partial x_k}}$ as a function of wall-normal distance.

ity correction exhibits a less dramatic influence than the free-shear type of correction when applied to boundary-layer flows, and that the correction works reasonably well in predicting wall skin friction for cold-wall cases. As also indicated by Figure 22c, Π^c is negligibly small in comparison with Π^t and Π^d throughout the boundary layer.
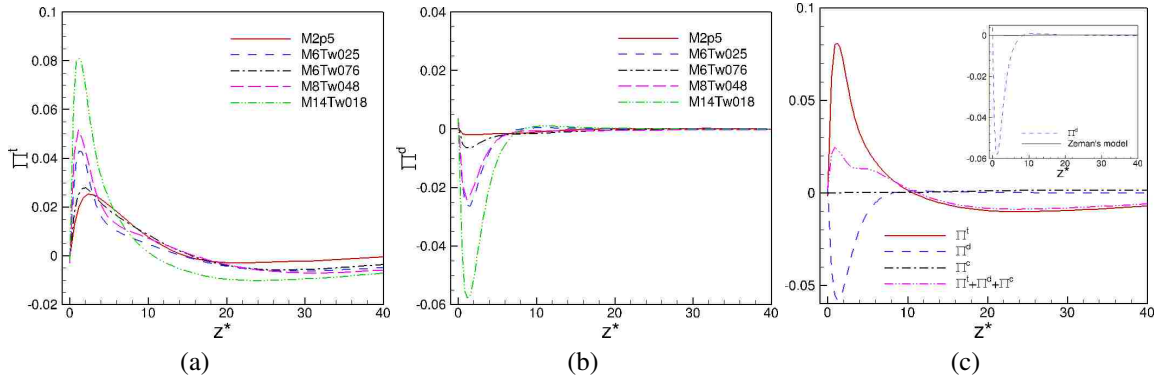
Figure 22. Wall-normal variation of (a) pressure diffusion and (b) pressure dilatation for the various DNS cases; (c) comparison of pressure terms for Case M14Tw018.

4. CONCLUSIONS

A DNS database of high-speed, zero-pressure-gradient turbulent boundary layers developing spatially over a flat plate is presented. Complementary to the limited datasets in the literature under high Mach number, cold-wall conditions, the database covers a wide range of freestream Mach numbers (M_∞ = 2.5 – 14) and wall-to-recovery temperature ratios (T_w/T_r = 0.18 – 1.0) and simulates the operational conditions of hypervelocity wind tunnels. The DNS is based on a high-order scheme with a large domain size and sufficiently long sampling size ($L_x/\delta_i > 50$, $L_y/\delta_i > 8$, $T_f u_\tau/\delta_i > 5$) to minimize any artificial effects due to inflow turbulence generation and to ensure the convergence of some of the high-order turbulence statistics. The physical realism and accuracy of the computed flow fields have been established by comparing with existing experimental results at similar flow conditions and with other high-quality simulations at lower Mach numbers.

The DNS database has been used to gauge the performance of compressibility transformations in the high-Mach-number, cold-wall regime, including the recently developed velocity and temperature scalings that explicitly account for the effect of wall cooling, with the main observations and conclusions summarized as follows:

(i) The mean velocity transformation of Trettel and Larsson (Trettel and Larsson, 2016) yields much improved collapse of the hypersonic data in the viscous sublayer when there is a strong heat transfer at the surface.

(ii) Zhang's generalized relation (Zhang *et al.*, 2014) between the mean velocity and the mean temperature yields better comparison with the DNS than that of Walz under cold wall conditions.

(iii) The semilocal scaling successfully collapses the Reynolds stresses, vorticity fluctuations, and the TKE budgets in most of the boundary layer at different Mach number and wall-cooling conditions, with notable differences largely limited to the near-wall region ($z^* \lessapprox 10$).

The apparent success of the various compressibility transformations in most of the boundary layer indicates that, within the relatively broad range of Mach number and wall cooling considered in this study, the effects of those two parameters can be largely taken into account with local mean flow conditions, in terms of density and viscosity, and that the turbulence dynamics of hypersonic turbulent boundary layers exhibits strong similarity to that of incompressible flows at comparable Reynolds numbers. Additional insights into the effects of intrinsic compressibility and wall-cooling are gained from the inspection of Reynolds stress anisotropy, the thermodynamic fluctuations, and the dissipation and pressure terms in TKE budgets. The main observations may be summarized as follows:

(i) There is an increase in the streamwise component of the Reynolds stress anisotropy and a decrease in the spanwise component as the Mach number and wall cooling increase, and such a change in Reynolds stress anisotropy may be indicative of modifications to intercomponent energy transfer in the high-Mach-number, cold-wall regime.

(ii) The fluctuating Mach number increases dramatically with the freestream Mach number; and at Mach 7.87 and 13.64, turbulent fluctuations become locally supersonic relative to the surrounding flow near the edge of the boundary layer.

(iii) As a result of the locally supersonic turbulent bulges and the likely creation of local shocklets that are a source of significant entropy production and dilatational dissipation, the fluctuating density and temperature develop a strong peak with large entropy fluctuations toward the edge of the boundary layer.

(iv) A sharp gradient in density and temperature is seen at the instantaneous interface between turbulent and nonturbulent flow regions or the edge of the turbulent bulges for the high-Mach-number cases.

(v) The dilatational dissipation and the pressure dilatation increase dramatically with increasing Mach number and wall-cooling rate. At Mach 13.64, the dilatational dissipation becomes non-negligible compared with the solenoidal dissipation in the near-wall region and close to the boundary-layer edge; pressure dilatation has a significant contribution to the sum of the pressure terms in the near-wall region ($z^* \lessapprox 10$) but the contribution diminishes farther away from the wall.

The DNS database under hypervelocity (but ideal gas) conditions complements the limited experimental datasets and the existing DNS databases that simulate either temporal boundary layers (Duan *et al.*, 2010, 2011; Martín, June 2004) or spatial boundary layers over an adiabatic wall (Lagha *et al.*, 2011). The database therefore represents a reliable resource for studying turbulence physics under high Mach number, cold-wall conditions and for validating compressibility transformations and RANS models. Precomputed flow statistics including Reynolds stresses and their budgets will be available at the website of the NASA Langley Turbulence Modeling Resource, allowing other investigators to query any property of interest.

ACKNOWLEDGEMENTS

REFERENCES

Bernardini, M. and Pirozzoli, S., 'Wall pressure fluctuations beneath supersonic turbulent boundary layers,' Physics of Fluids, 2011, **23**, p. 085102, doi:10.1063/1.3622773.

Coleman, G. N., Kim, J., and Moser, R. D., 'A numerical study of turbulent supersonic isothermal-wall channel flow,' Journal of Fluid Mechanics, 1995, **305**, pp. 159–183, doi:10.1017/S0022112095004587.

Degraaff, D. B. and Eaton, J. K., 'Reynolds-number scaling of the flat-plate turbulent boundary layer,' Journal of Fluid Mechanics, 2000, **422**, pp. 319–346, doi:10.1017/S0022112000001713.

Duan, L., Beekman, I., and Martín, M. P., 'Direct numerical simulation of hypersonic turbulent boundary layers. part 2: Effect of wall temperature,' Journal of Fluid Mechanics, 2010, **655**, pp. 419–445, doi:10.1017/S0022112010000959.

Duan, L., Beekman, I., and Martín, M. P., 'Direct numerical simulation of hypersonic turbulent boundary layers. part 3: Effect of mach number,' Journal of Fluid Mechanics, 2011, **672**, pp. 245–267, doi:10.1017/S0022112010005902.

Duan, L. and Choudhari, M. M., 'Analysis of numerical simulation database for pressure fluctuations induced by high-speed turbulent boundary layers,' 20th AIAA/CEAS Aeroacoustics Conference, AIAA AVIATION Forum, AIAA Paper 2014-2912, 2014, doi:10.2514/6.2014-2912.

Duan, L., Choudhari, M. M., Chou, A., Munoz, F., Ali, S. R. C., Radespiel, R., Schilden, T., Schröder, W., Marineau, E. C., Casper, K. M., Chaudhry, R. S., Candler, G. V., Gray, K. A., Sweeney, C. J., and Schneider, S. P., 'Characterization of freestream disturbances in conventional hypersonic wind tunnels,' 2018 AIAA Aerospace Sciences Meeting, AIAA SciTech Forum, AIAA Paper 2018-0347, Jan. 2018, doi:10.2514/6.2018-0347.

Duan, L., Choudhari, M. M., and Wu, M., 'Numerical study of pressure fluctuations due to a supersonic turbulent boundary layer,' Journal of Fluid Mechanics, 2014, **746**, pp. 165–192, doi:10.1017/jfm.2014.116.

Duan, L., Choudhari, M. M., and Zhang, C., 'Pressure fluctuations induced by a hypersonic turbulent boundary layer,' Journal of Fluid Mechanics, 2016, **804**, pp. 578–607, doi: 10.1017/jfm.2016.548.

Duan, L. and Martín, M. P., 'Direct numerical simulation of hypersonic turbulent boundary layers. part 4: Effect of high enthalpy,' Journal of Fluid Mechanics, 2011, **684**, pp. 25–59, doi:10.1017/jfm.2011.252.

Ekoto, I. W., Bowersox, R. D. W., Brutner, T., and Goss, L., 'Supersonic boundary layers with periodic surface roughness,' AIAA Journal, 2008, **46**(2), pp. 486–497, doi: 10.2514/1.31729.

Foysi, H., Sarkar, S., and Friedrich, R., 'Compressibility effects and turbulence scalings in supersonic channel flow,' Journal of Fluid Mechanics, 2004, **509**, pp. 207–216, doi:10.1017/S0022112004009371.

Gaviglio, J., 'Reynolds analogies and experimental study of heat transfer in the supersonic boundary layer,' International journal of heat and mass transfer, 1987, **30**(5), pp. 911–926, doi:10.1016/0017-9310(87)90010-X.

Guarini, S. E., Moser, R. D., Shariff, K., and Wray, A., 'Direct numerical simulation of a supersonic turbulent boundary layer at mach 2.5,' Journal of Fluid Mechanics, 2000, **414**, pp. 1–33, doi:10.1017/S0022112000008466.

Hadjadj, A., Ben-Nasr, O., Shadloo, M., and Chaudhuri, A., 'Effect of wall temperature in supersonic turbulent boundary layers: A numerical study,' International Journal of Heat and Mass Transfer, 2015, **81**, pp. 426–438, doi:10.1016/j.ijheatmasstransfer.2014.10.025.

Huang, P. G., Coleman, G., and Bradshaw, P., 'Compressible Turbulent Channel Flows: DNS Results and Modelling,' Journal of Fluid Mechanics, 1995, **305**, pp. 185–218, doi:10.1017/S0022112095004599.

Jiménez, J., Hoyas, S., Simens, M. P., and Mizuno, Y., 'Turbulent boundary layers and channels at moderate reynolds numbers,' Journal of Fluid Mechanics, 2010, **657**, p. 335, doi:10.1017/S0022112010001370.

Keyes, F. G., 'A summary of viscosity and heat-conduction data for He, A, H_2, O_2, CO, CO_2, H_2O, and air,' Transactions of the American Society of Mechanical Engineers, 1951, **73**, pp. 589–596.

Kovasznay, L. S., 'Turbulence in supersonic flow,' Journal of the Aeronautical Sciences, 1953, **20**(10), pp. 657–674, doi:10.2514/8.2793.

Lagha, M., Kim, J., Eldredge, J., and Zhong, X., 'A numerical study of compressible turbulent boundary layers,' Physics of fluids, 2011, **23**(1), p. 015106, doi: 10.1063/1.3541841.

Laufer, J., 'Some statistical properties of the pressure field radiated by a turbulent boundary layer,' Physics of Fluids, 1964, **7**(8), pp. 1191–1197, doi:10.1063/1.1711360.

Lele, S. K., 'Compressibility effects on turbulence,' Annual Review of Fluid Mechanics, 1994, **26**, pp. 211–254, doi:10.1146/annurev.fl.26.010194.001235.

Maeder, T., *Numerical Investigation of Supersonic Turbulent Boundary Layers*, Ph.D. thesis, ETH, Zürich, 2000.

Martín, M., 'DNS of hypersonic turbulent boundary layers. part I: Initialization and comparison with experiments,' Journal of Fluid Mechanics, 2007, **570**, pp. 347–364, doi:10.1017/S0022112006003107.

Martín, M. P., 'Dns of hypersonic turbulent boundary layers,' 34th AIAA Fluid Dynamics Conference and Exhibit, AIAA Paper 2004-2337, June 2004, doi:10.2514/6.2004-2337.

Martín, M. P., Taylor, E. M., Wu, M., and Weirs, V. G., 'A bandwidth-optimized weno scheme for the direct numerical simulation of compressible turbulence,' Journal of Computational Physics, 2006, **220**(1), pp. 270–289, doi:10.1016/j.jcp.2006.05.009.

Modesti, D. and Pirozzoli, S., 'Reynolds and mach number effects in compressible turbulent channel flow,' International Journal of Heat and Fluid Flow, 2016, **59**, pp. 33–49, doi:10.1016/j.ijheatfluidflow.2016.01.007.

Morkovin, M. V., 'Effects of compressibility on turbulent flows,' In Mécanique de la Turbulence (ed. A. J. Favre), CNRS, 1962, pp. 367–380.

Patel, A., Boersma, B. J., and Pecnik, R., 'The influence of near-wall density and viscosity gradients on turbulence in channel flows,' Journal of Fluid Mechanics, 2016, **809**, pp. 793–820, doi:10.1017/jfm.2016.689.

Patel, A., Peeters, J. W., Boersma, B. J., and Pecnik, R., 'Semi-local scaling and turbulence modulation in variable property turbulent channel flows,' Physics of Fluids, 2015, **27**(9), p. 095101, doi:10.1063/1.4929813.

Peltier, S., Humble, R., and Bowersox, R., 'Crosshatch roughness distortions on a hypersonic turbulent boundary layer,' Physics of Fluids, 2016, **28**(4), p. 045105, doi: 10.1063/1.4944657.

Pirozzoli, S. and Bernardini, M., 'Turbulence in supersonic boundary layers at moderate Reynolds numbers,' Journal of Fluid Mechanics, 2011, **688**, pp. 120–168, doi:10.1017/jfm.2011.368.

Poggie, J., Bisek, N. J., and Gosse, R., 'Resolution effects in compressible, turbulent boundary layer simulations,' Computers and Fluids, 2015, **120**, pp. 57–69, doi: 10.1016/j.compfluid.2015.07.015.

Priebe, S. and Martín, M. P., 'Direct numerical simulation of a hypersonic turbulent boundary layer on a large domain,' 41st AIAA Fluid Dynamics Conference and Exhibit AIAA Paper 2011-3432, June 2011, doi:10.2514/6.2011-3432.

Roy, C. J. and Blottner, F. G., 'Review and assessment of turbulence models for hypersonic flows,' Progress in Aerospace Sciences, 2006, **42**(7-8), pp. 469–530, doi:10.1016/j.paerosci.2006.12.002.

Rumsey, C. L., 'Compressibility considerations for $k - \omega$ turbulence models in hypersonic boundary-layer applications,' Journal of Spacecraft and Rockets, 2010, **47**(1), pp. 11–20, doi:10.2514/1.45350.

Sarkar, S., Erlebacher, G., Hussaini, M. Y., and Kreiss, H. O., 'The analysis and modeling of dilatational terms in compressible turbulence,' Journal of Fluid Mechanics, 1991, **227**, pp. 473–493, doi:10.1017/S0022112091000204.

Shadloo, M., Hadjadj, A., and Hussain, F., 'Statistical behavior of supersonic turbulent boundary layers with heat transfer at $M_{\infty}=$ 2,' International Journal of Heat and Fluid Flow, 2015, **53**, pp. 113–134, doi:10.1016/j.ijheatfluidflow.2015.02.004.

Shahab, M. F., Lehnasch, G., Gatski, T. B., and Comte, P., 'Statistical characteristics of an isothermal, supersonic developing boundary layer flow from dns data,' Flow, Turbulence and Combustion, 2011, **86**(3-4), pp. 369–397, doi:10.1007/s10494-011-9329-0.

Sillero, J. A., Jiménez, J., and Moser, R. D., 'One-point statistics for turbulent wall-bounded flows at reynolds numbers up to $\delta^+ \approx$ 2000,' Physics of Fluids, 2013, **25**(10), p. 105102, doi:10.1063/1.4823831.

Smits, A. J. and Dussauge, J. P., *Turbulent Shear Layers in Supersonic Flow*, Springer-Verlag New York, 2 edition, 2006, doi:10.1007/b137383.

Smits, A. J. and Martín, M. P., 'Turbulence in supersonic and hypersonic boundary layers,' in 'IUTAM Symposium on One Hundred Years of Boundary Layer Research,' DLR Göttingen, Germany, Aug. 2004 pp. 221–230.

Taylor, E. M., Wu, M., and Martín, M. P., 'Optimization of nonlinear error sources for weighted non-oscillatory methods in direct numerical simulations of compressible turbulence,' Journal of Computational Physics, 2006, **223**, pp. 384–397, doi:10.1016/j.jcp.2006.09.010.

Tichenor, N. R., Humble, R. A., and Bowersox, R. D. W., 'Response of a hypersonic turbulent boundary layer to favourable pressure gradients,' Journal of Fluid Mechanics, 2013, **722**, pp. 187–213, doi:10.1017/jfm.2013.89.

Trettel, A. and Larsson, J., 'Mean velocity scaling for compressible wall turbulence with heat transfer,' Physics of Fluids, 2016, **28**(026102), doi:10.1063/1.4942022.

van Driest, E. R., 'The problem of aerodynamic heating,' Aeronautical Engineering Review, 1956, **15**(10), pp. 26–41.

Walz, A., *Boundary Layers of Flow and Temperature*, MIT Press, Cambridge, MA, 1969.

Wilcox, D. C., *Turbulence Modeling for CFD*, DCW Industries, 3 edition, 2006.

Williams, O. J. H., Sahoo, D., Baumgartner, M. L., and Smits, A. J., 'Experiments on the structure and scaling of hypersonic turbulent boundary layers,' Journal of Fluid Mechanics, 2018, **834**, pp. 237–270, doi:10.1017/jfm.2017.712.

Williamson, J., 'Low-storage Runge-Kutta schemes,' Journal of Computational Physics, 1980, **35**(1), pp. 48–56, doi:10.1016/0021-9991(80)90033-9.

Wu, B., Bi, W., Hussain, F., and She, Z.-S., 'On the invariant mean velocity profile for compressible turbulent boundary layers,' Journal of Turbulence, 2016, pp. 1–17, doi:10.1080/14685248.2016.1269911.

Zeman, O., 'Dilatation dissipation: The concept and application in modeling compressible mixing layers,' Physics of Fluids A, 1990, **2**, pp. 178–188, doi:10.1063/1.857767.

Zeman, O., 'A new model for supersonic/hypersonic turbulent boundary layers,' 31st Aerospace Sciences Meeting, AIAA Paper 1993-0897, Jan. 1993, doi:10.2514/6.1993-897.

Zhang, C., Duan, L., and Choudhari, M. M., 'Effect of wall cooling on boundary layer induced pressure fluctuations at mach 6,' Journal of Fluid Mechanics, 2017, **822**, pp. 5–30, doi:10.1017/jfm.2017.212.

Zhang, C., Duan, L., and Choudhari, M. M., 'Acoustic radiation from a Mach 14 turbulent boundary layers,' 54th AIAA Aerospace Sciences Meeting, AIAA Paper 2016-0048, Jan. 2016, doi:10.2514/6.2016-0048.

Zhang, Y., Bi, W., Hussain, F., and She, Z., 'A generalized reynolds analogy for compressible wall-bounded turbulent flows,' Journal of Fluid Mechanics, 2014, **739**, pp. 392–420, doi:10.1017/jfm.2013.620.

SECTION

2. SUMMARY AND CONCLUSIONS

A DNS database of high-speed, zero-pressure-gradient turbulent boundary layers developing spatially over a flat plate is presented. Complementary to the limited datasets in the literature under high Mach number, cold-wall conditions, the database covers a wide range of freestream Mach numbers (M_∞ = 2.5 – 14) and wall-to-recovery temperature ratios (T_w/T_r = 0.18 – 1.0) and simulates the operational conditions of hypervelocity wind tunnels. The DNS is based on a high-order scheme with a large domain size and sufficiently long sampling size ($L_x/\delta_i > 50$, $L_y/\delta_i > 8$, $T_f u_\tau/\delta_i > 5$) to minimize any artificial effects due to inflow turbulence generation and to ensure the convergence of some of the high-order turbulence statistics. The physical realism and accuracy of the computed flow fields have been established by comparing with existing experimental results at similar flow conditions and with other high-quality simulations at lower Mach numbers.

The DNS database has been used to gauge the performance of compressibility transformations in the high-Mach-number, cold-wall regime, including the recently developed velocity and temperature scalings that explicitly account for the effect of wall cooling, with the main observations and conclusions summarized as follows:

(i) The mean velocity transformation of Trettel and Larsson (Trettel and Larsson, 2016) yields much improved collapse of the hypersonic data in the viscous sublayer when there is a strong heat transfer at the surface.

(ii) Zhang's generalized relation (Zhang *et al.*, 2014) between the mean velocity and the mean temperature yields better comparison with the DNS than that of Walz under cold wall conditions.

(iii) The semilocal scaling successfully collapses the Reynolds stresses, vorticity fluctuations, and the TKE budgets in most of the boundary layer at different Mach number and wall-cooling conditions, with notable differences largely limited to the near-wall region ($z^* \lessapprox 10$).

The apparent success of the various compressibility transformations in most of the boundary layer indicates that, within the relatively broad range of Mach number and wall cooling considered in this study, the effects of those two parameters can be largely taken into account with local mean flow conditions, in terms of density and viscosity, and that the turbulence dynamics of hypersonic turbulent boundary layers exhibits strong similarity to that of incompressible flows at comparable Reynolds numbers.

The wall-normal variation of the fluctuating pressure field is investigated and the differences between the primarily vortical pressure signal within the boundary layer and the acoustic pressure signal in the free stream is highlighted. The main observations and conclusions are summarized as follows:

(i) The spectrum peak of pressure signals shifts to lower frequencies as the location of interest moves away from the wall.

(ii) Compared with the pressure signal within the boundary layer, the freestream acoustic pressure fluctuations exhibit a significantly lower dominant frequency, a greater spatial extent, a smaller structure angle, and a smaller bulk propagation speed.

(iii) Within the boundary layer (except in the immediate vicinity of the wall), Taylor's hypothesis approximately holds with pressure waves propagating with the local mean velocity. In the free stream, however, the propagation speed of pressure fluctuations is significantly smaller than the freestream velocity, even though the 'frozen-eddy' assumption approximately holds as indicated by the value of $\gamma_p \approx 1$.

(iv) There is an apparent match in the Lagrangian time and spatial scales between the freestream pressure structures and the structures near the wall. Given that the free-stream acoustic radiation is generated by turbulent fluctuations within the boundary layer, the apparent match in Lagrangian scales indicates that the acoustic sources are located near the wall.

The effect of wall cooling on the pressure fluctuations generated by hypersonic turbulent boundary layers is investigated using Mach 5.86 turbulent boundary layers with two wall temperatures (T_w/T_r =0.25, 0.76). The main conclusions are summarized as follows:

(i) Simulations show that wall cooling significantly modifies the pressure-fluctuation intensities near the wall, with $p'_{w,rms}/\tau_w$ varying from 2.8 for $T_w/T_r = 0.76$ to 3.5 for $T_w/T_r = 0.25$.

(ii) The frequency spectra of wall-pressure fluctuations for the two cases show considerable differences when plotted in terms of either outer-layer or inner-layer variables. The peak of the pre-multiplied spectrum shifts to a higher value as the wall temperature decreases.

(iii) Wall cooling slows down the evolution of pressure wavepackets at the wall, resulting in a larger decorrelation length of pressure structures, but has little influence on the bulk propagation speeds of wall-pressure structures.

(iv) Regarding the freestream pressure fluctuations, although the intensity shows a strong wall-temperature dependence when normalized by the mean freestream pressure, it compares well between the two cases when normalized by the local wall shear stress.

(v) Similar to pressure structures at the wall, the freestream pressure structures evolve less rapidly as the wall temperature decreases. The propagation speed of freestream pressure structures is found to be insensitive to wall temperature and is significantly smaller than the freestream velocity for both cases.

(vi) An analysis of acoustic sources using the acoustic analogy of Phillips shows that wall cooling influences sound generation largely by enhancing dilatational motions in the viscous sublayer while damping streamwise vortical structures in the buffer layer.

Additional insights into the effects of intrinsic compressibility and wall-cooling are gained from the inspection of Reynolds stress anisotropy, the thermodynamic fluctuations, and the dissipation and pressure terms in TKE budgets. The main observations may be summarized as follows:

(i) There is an increase in the streamwise component of the Reynolds stress anisotropy and a decrease in the spanwise component as the Mach number and wall cooling increase, and such a change in Reynolds stress anisotropy may be indicative of modifications to intercomponent energy transfer in the high-Mach-number, cold-wall regime.

(ii) The fluctuating Mach number increases dramatically with the freestream Mach number; and at Mach 7.87 and 13.64, turbulent fluctuations become locally supersonic relative to the surrounding flow near the edge of the boundary layer.

(iii) As a result of the locally supersonic turbulent bulges and the likely creation of local shocklets that are a source of significant entropy production and dilatational dissipation, the fluctuating density and temperature develop a strong peak with large entropy fluctuations toward the edge of the boundary layer.

(iv) A sharp gradient in density and temperature is seen at the instantaneous interface between turbulent and nonturbulent flow regions or the edge of the turbulent bulges for the high-Mach-number cases.

(v) The dilatational dissipation and the pressure dilatation increase dramatically with increasing Mach number and wall-cooling rate. At Mach 13.64, the dilatational dissipation becomes non-negligible compared with the solenoidal dissipation in the near-wall region and close to the boundary-layer edge; pressure dilatation has a significant contribution to the sum of the pressure terms in the near-wall region ($z^* \lesssim 10$) but the contribution diminishes farther away from the wall.

The DNS database under hypervelocity (but ideal gas) conditions complements the limited experimental datasets and the existing DNS databases that simulate either temporal boundary layers (Duan *et al.*, 2010, 2011; Martin, 2004) or spatial boundary layers over an adiabatic wall (Lagha *et al.*, 2011). The database therefore represents a reliable resource for studying turbulence physics under high Mach number, cold-wall conditions and for validating compressibility transformations and RANS models. Precomputed flow statistics including Reynolds stresses and their budgets will be available at the website of the NASA Langley Turbulence Modeling Resource, allowing other investigators to query any property of interest.

REFERENCES

Beresh, S. J., Henfling, J. F., Spillers, R. W., and Pruett, B. O. M., 'Fluctuating wall pressures measured beneath a supersonic turbulent boundary layer,' Physics of Fluids, 2011, **23**(075110).

Bernardini, M. and Pirozzoli, S., 'Wall pressure fluctuations beneath supersonic turbulent boundary layers,' Physics of Fluids, 2011, **23**, p. 085102, doi:10.1063/1.3622773.

Bernardini, M., Pirozzoli, S., and Grasso, F., 'The wall pressure signature of transonic shock/boundary layer interaction,' Journal of Fluid Mechanics, 2011, **671**, pp. 288–312.

Bies, D. W., 'A review of flight and wind tunnel measurements of boundary layer pressure fluctuations and induced structure reponse,' Technical report, NASA CR-626, 1966.

Blake, W. K., *Mechanics of Flow-Induced Sound and Vibration*, Academic Press, Orlando, Florida, 1986.

Bookey, P., Wyckham, C., Smits, A. J., and Martin, M. P., 'New experimental data of stbli at dns/les accessible reynolds numbers,' AIAA Paper 2005-309, 2005.

Bounitch, A., Lewis, D. R., and Lafety, J. F., 'Experimental study of second-mode instabilities on a 7-degree cone at Mach 6,' in 'AIAA Paper 2011-1200,' 2011 .

Bowersox, R. D. W., 'Extension of equilibrium turbulent heat flux models to high-speed shear flows,' J. Fluid Mech., 2009, **633**, pp. 61–70.

Bradshaw, P., 'Inactive motion and pressure fluctuations in turbulent boundary layers,' Journal of Fluid Mechanics, 1967, **30**, pp. 241–258.

Bull, M. K., 'Wall-pressure fluctuations beneath turbulent boundary layers: Some reflection on forty years of research,' Journal of Sound and Vibration, 1996, **190**(3), pp. 299–315.

Cadot, O., Douady, S., and Couder, Y., 'Characterization of the low-pressure filaments in a three-dimensional turbulent shear flow,' Physics of Fluids, 1995, **7**, pp. 630–646.

Casper, K. M., 'Turbulent pressure fluctuations in a hypersonic boundary layer,' 2011, aAE 626 Final Project Report, Purdue University, West Lafayette, IN, USA, 2011.

Choi, H. and Moin, P., 'On the space-time characteristics of wall-pressure fluctuations,' Physics of Fluids, 1990, **2**(8), pp. 1450–1460.

Chu, Y. B., Zhang, Y. Q., and Lu, X. Y., 'Effect of wall temperature on hypersonic turbulent boundary layer,' J. Turbul., 2013, **14**(12), pp. 37–57.

Coleman, G. N., Kim, J., and Moser, R. D., 'A numerical study of turbulent supersonic isothermal-wall channel flow,' Journal of Fluid Mechanics, 1995, **305**, pp. 159–183.

Degraaff, D. B. and Eaton, J. K., 'Reynolds-number scaling of the flat-plate turbulent boundary layer,' Journal of Fluid Mechanics, 2000, **422**, pp. 319–346, cited By (since 1996): 131.

Del Alamo, J. C. and Jimenez, J., 'Estimation of turbulent convection velocities and corrections to taylor's approximation,' Journal of Fluid Mechanics, 2009, **640**, pp. 5–26.

Dolling, D. S. and Dussauge, J. P., 'A survey of measurements and measuring techniques in rapidly distorted compressible turbulent boundary layers,' AGARDograph, 1989, **315**, pp. 1–18.

Donaldson, J. and Coulter, S., 'A review of free-stream flow fluctuation and steady-state flow quality measurements in the AEDC/VKF supersonic tunnel A and hypersonic tunnel B,' AIAA Paper 95-6137, 1995.

Duan, L., Beekman, I., and Martín, M. P., 'Direct numerical simulation of hypersonic turbulent boundary layers. part 2: Effect of wall temperature,' Journal of Fluid Mechanics, 2010, **655**, pp. 419–445.

Duan, L., Beekman, I., and Martín, M. P., 'Direct numerical simulation of hypersonic turbulent boundary layers. part 3: Effect of Mach number,' Journal of Fluid Mechanics, 2011, **672**, pp. 245–267.

Duan, L. and Choudhari, M. M., 'Analysis of numerical simulation database for pressure fluctuations induced by high-speed turbulent boundary layers,' 20th AIAA/CEAS Aeroacoustics Conference, AIAA AVIATION Forum, AIAA Paper 2014-2912, 2014, doi:10.2514/6.2014-2912.

Duan, L., Choudhari, M. M., and Wu, M., 'Numerical study of pressure fluctuations due to a supersonic turbulent boundary layer,' Journal of Fluid Mechanics, 2014, **746**, pp. 165–192.

Duan, L., Choudhari, M. M., and Zhang, C., 'Pressure fluctuations induced by a hypersonic turbulent boundary layer,' J. Fluid Mech., 2016, **804**, pp. 578–607.

Duan, L. and Martín, M. P., 'Direct numerical simulation of hypersonic turbulent boundary layers. part 4: Effect of high enthalpy,' Journal of Fluid Mechanics, 2011, **684**, pp. 25–59.

Ekoto, I. W., Bowersox, R. D. W., Brutner, T., and Goss, L., 'Supersonic boundary layers with periodic surface roughness,' AIAA Journal, 2008, **46**(2), pp. 486–497, doi: 10.2514/1.31729.

Eléna, M. and Lacharme, J. P., 'Experimental study of a supersonic turbulent boundary layer using a laser doppler anemometer,' Journal de Mécanique Théorique et Appliquée, 1988, **7**, pp. 175–190.

Fernholz, H. H. and Finley, P. J., 'A critical commentary on mean flow data for two-dimensional compressible turbulent boundary layers.' AGARDograph, 1980, **253**.

Ffowcs-Williams, J. E. and Maidanik, G., 'The Mach wave field radiated by supersonic turbulent shear flows,' Journal of Fluid Mechanics, 1965, **21**, pp. 641–657.

Ganapathisubramani, B., Clemens, N., Hambleton, W. T., Longmire, E. K., and Marusic, I., 'Investigation of large-scale coherence in a turbulent boundary layer uisng two-point correlations,' Journal of Fluid Mechanics, 2005, **524**, pp. 57–80.

Ganapathisubramani, B., Clemens, N. T., and Dolling, D. S., 'Large-scale motions in a supersonic turbulent boundary layer,' Journal of Fluid Mechanics, 2006, **556**, pp. 271–282.

Gaviglio, J., 'Reynolds analogies and experimental study of heat transfer in the supersonic boundary layer,' International journal of heat and mass transfer, 1987, **30**(5), pp. 911–926, doi:10.1016/0017-9310(87)90010-X.

Gloerfelt, X. and Berland, J., 'Turbulent boundary-layer noise: Direct radiation at mach number 0.5,' Journal of Fluid Mechanics, 2013, **723**, pp. 318–351.

Guarini, S. E., Moser, R. D., Shariff, K., and Wray, A., 'Direct numerical simulation of a supersonic turbulent boundary layer at Mach 2.5,' Journal of Fluid Mechanics, 2000, **414**, pp. 1–33.

Hadjadj, A., Ben-Nasr, O., Shadloo, M. S., and Chaudhuri, A., 'Effect of wall temperature in supersonic turbulent boundary layers: A numerical study,' Int. J. Heat Mass Transfer, 2015, **81**, pp. 426–438.

Harris, J. and Blanchard, D., 'Computer program for solving laminar, transitional, or turbulent compressible boundary-layer equations for two-dimensional and axisymmetric flow,' NASA-TM-83207, 1982.

Huang, P. G., Coleman, G., and Bradshaw, P., 'Compressible turbulent channel flows: DNS results and modelling,' J. Fluid Mech., 1995, **305**, pp. 185–218.

Jiang, G. S. and Shu, C. W., 'Efficient implementation of weighted ENO schemes,' Journal of Computational Physics, 1996, **126**(1), pp. 202–228.

Jiménez, J., Hoyas, S., Simens, M. P., and Mizuno, Y., 'Turbulent boundary layers and channels at moderate reynolds numbers,' Journal of Fluid Mechanics, 2010, **657**, p. 335, doi:10.1017/S0022112010001370.

Kat, R. D. and Oudheusden, B. W. V., 'Instantaneous planar pressure determination from PIV in turbulent flows,' Experiments in Fluids, 2012, **52**(5), pp. 1089–1106.

Kendall, J. M., 'Supersonic boundary layer transition studies,' Space Program Summary, 1970, **3**, pp. 43–47.

Kida, S. and Miura, H., 'Identification and analysis of vortical structures,' European Journal of Mechanics - B/Fluids, 1998, **17**(4), pp. 471–488.

Kim, J., 'On the structure of pressure fluctuations in simulated turbulent channel flow,' Journal of Fluid Mechanics, 1989, **205**, pp. 421–451.

Kim, J. and Hussain, F., 'Propagation velocity of perturbations in turbulent channel flow,' Physics of Fluids, 1993, **5**(3), pp. 695–706.

Kim, K. C. and Adrian, R. J., 'Very large-scale motion in the outer layer,' Physics of Fluids, 1999, **11**, pp. 417–422.

Kistler, A. L. and Chen, W. S., 'The fluctuating pressure field in a supersonic turbulent boundary layer,' Journal of Fluid Mechanics, 1963, **16**, pp. 41–64.

Kovasznay, L. S. G., 'Turbulence in supersonic flow,' Journal of Aeronautical Sciences, 1953, **20**, pp. 657–674.

Lagha, M., Kim, J., Eldredge, J. D., and Zhong, X., 'A numerical study of compressible turbulent boundary layers,' Phys. Fluids, 2011, **23**(1), p. 015106.

Laufer, J., 'Some statistical properties of the pressure field radiated by a turbulent boundary layer,' Physics of Fluids, 1964, **7**(8), pp. 1191–1197.

Lele, S. K., 'Compressibility Effects on Turbulence,' Annu. Rev. Fluid Mech, 1994, **26**, pp. 211–254.

Liepmann, H. W. and Roshko, A., *Elements of Gasdynamics*, John Wiley & Sons, Inc. New York, 1957.

Maeder, T., *Numerical investigation of supersonic turbulent boundary layers*, Ph.D. thesis, ETH, Zürich, 2000.

Maestrello, L., 'Radiation from and panel response to a supersonic turbulent boundary layer,' Journal of Sound Vibration, 1969, **10**(2), pp. 261–262.

Marco, A. D., Camussi, R., Bernardini, M., and Pirozzoli, S., 'Wall pressure coherence in supersonic turbulent boundary layers,' Journal of Fluid Mechanics, 2013, **732**, pp. 445–456.

Martin, M., 'DNS of hypersonic turbulent boundary layers,' 34th AIAA Fluid Dynamics Conference, 2004.

Martín, M., 'DNS of hypersonic turbulent boundary layers. part i: Initialization and comparison with experiments,' Journal of Fluid Mechanics, 2007, **570**, pp. 347–364.

Martín, M. P., Taylor, E. M., Wu, M., and Weirs, V. G., 'A bandwidth-optimized weno scheme for the direct numerical simulation of compressible turbulence,' Journal of Computational Physics, 2006, **220**(1), pp. 270–289.

Masutti, M., Chazot, E., and Carbonaro, M., 'Disturbance level characterization of a hypersonic blowdown facility,' AIAA Journal, 2012, **50**(12).

Modesti, D. and Pirozzoli, S., 'Reynolds and mach number effects in compressible turbulent channel flow,' International Journal of Heat and Fluid Flow, 2016a, **59**, pp. 33–49, doi:10.1016/j.ijheatfluidflow.2016.01.007.

Modesti, D. and Pirozzoli, S., 'Reynolds and Mach number effects in compressible turbulent channel flow,' Int. J. Heat Fluid Flow, 2016b, **59**, pp. 33–49.

Morgan, B., Larsson, J., Kawai, S., and Lele, S. K., 'Improving low-frequency characteristics of recycling/rescaling inflow turbulence generation,' AIAA Journal, 2011, **49**(3), pp. 582–597.

Morkovin, M. V., 'Effects of compressibility on turbulent flows,' in A. J. Favre, editor, 'Mécanique de la Turbulence,' CNRS, 1962 pp. 367–380.

Naka, Y., Stanislas, M., Foucaut, J. M., Coudert, S., Laval, J. P., and Obi, S., 'Space-time pressure-velocity correlations in a turbulent boundary layer,' Journal of Fluid Mechanics, 2015, **771**, pp. 624–675.

Pate, S. R., 'Dominance of radiated aerodynamic noise on boundary-layer transition in supersonic-hypersonic wind tunnels,' Technical Report AEDC-TR-77-107, Arnold Engineering Development Center, 1978.

Patel, A., Boersma, B. J., and Pecnik, R., 'The influence of near-wall density and viscosity gradients on turbulence in channel flows,' Journal of Fluid Mechanics, 2016, **809**, pp. 793–820, doi:10.1017/jfm.2016.689.

Patel, A., Peeters, J. W., Boersma, B. J., and Pecnik, R., 'Semi-local scaling and turbulence modulation in variable property turbulent channel flows,' Physics of Fluids, 2015, **27**(9), p. 095101, doi:10.1063/1.4929813.

Peltier, S., Humble, R., and Bowersox, R., 'Crosshatch roughness distortions on a hypersonic turbulent boundary layer,' Physics of Fluids, 2016a, **28**(4), p. 045105, doi: 10.1063/1.4944657.

Peltier, S. J., Humble, R. A., and Bowersox, R. D. W., 'PIV of a mach 5 turbulent boundary layer over diamond roughness elements,' AIAA Paper 2012-3061, 2012.

Peltier, S. J., Humble, R. A., and Bowersox, R. D. W., 'Crosshatch roughness distortions on a hypersonic turbulent boundary layer,' Phys. Fluids, 2016b, **28**(4), p. 045105.

Phillips, O. M., 'On the generation of sound by supersonic turbulent shear layers,' Journal of Fluid Mechanics, 1960, **9**, pp. 1–28.

Piponniau, S., Dussauge, J. P., Debieve, J. F., and Dupont, P., 'A simple model for low-frequency unsteadiness in shock-induced separation,' Journal of Fluid Mechanics, 2009, **629**, pp. 87–108.

Pirozzoli, S. and Bernardini, M., 'Turbulence in supersonic boundary layers at moderate Reynolds numbers,' Journal of Fluid Mechanics, 2011, **688**, pp. 120–168.

Poggie, J., 'Compressible turbulent boundary layer simulations: Resolution effects and turbulence modeling,' AIAA Paper 2015-1983, 2015.

Priebe, S. and Martín, M. P., 'Low-frequency unsteadiness in shock wave-turbulent boundary layer interaction,' Journal of Fluid Mechanics, 2012, **699**, pp. 1–49.

Priebe, S. and Martín, M. P., 'Direct numerical simulation of a hypersonic turbulent boundary layer on a large domain,' 41st AIAA Fluid Dynamics Conference and Exhibit AIAA Paper 2011-3432, June 2011, doi:10.2514/6.2011-3432.

Roy, C. J. and Blottner, F. G., 'Review and assessment of turbulence models for hypersonic flows,' Progress in Aerospace Sciences, 2006, **42**(7-8), pp. 469–530, doi:10.1016/j.paerosci.2006.12.002.

Rumsey, C. L., 'Compressibility considerations for $k - \omega$ turbulence models in hypersonic boundary-layer applications,' Journal of Spacecraft and Rockets, 2010, **47**(1), pp. 11–20, doi:10.2514/1.45350.

Schlatter, P. and Örlü, R., 'Assessment of direct numerical simulation data of turbulent boundary layers,' Journal of Fluid Mechanics, 2010, **659**, pp. 116–126.

Schneider, S. P., 'Effects of high-speed tunnel noise on laminar-turbulent transition,' Journal of Spacecraft and Rockets, 2001, **38**(3), pp. 323–333.

Schneider, S. P., 'Development of hypersonic quiet tunnels,' Journal of Spacecraft and Rockets, 2008, **45**(4), pp. 641–664.

Shadloo, M. S., Hadjadj, A., and Hussain, F., 'Statistical behavior of supersonic turbulent boundary layers with heat transfer at $M_\infty = 2$,' Int. J. Heat Fluid Flow, 2015, **53**, pp. 113–134.

Shahab, M. F., Lehnasch, G., GatskiEmail, T. B., and Comte, P., 'Statistical characteristics of an isothermal, supersonic developing boundary layer flow from DNS data,' Flow Turbul. Combust, 2011, **86**(3), pp. 369–397.

Sillero, J. A., Jiménez, J., and Moser, R. D., 'One-point statistics for turbulent wall-bounded flows at reynolds numbers up to $\delta^+ \approx 2000$,' Physics of Fluids, 2013, **25**(10), p. 105102, doi:10.1063/1.4823831.

Simens, M. P., Jimenez, J., Hoyas, S., and Mizuno, Y., 'A high-resolution code for turbulent boundary layers,' Journal of Computational Physics, 2009, **228**(11), pp. 4218–4231.

Smits, A. J., 'Turbulent boundary layer structure in supersonic flow,' Phil. Trans. R. Soc. London Ser. A, 1991, **336**(1641), pp. 81–93.

Smits, A. J. and Dussauge, J. P., *Turbulent Shear Layers in Supersonic Flow*, Springer-Verlag New York, 2 edition, 2006a, doi:10.1007/b137383.

Smits, A. J. and Dussauge, J. P., *Turbulent Shear Layers in Supersonic Flow*, American Institute of Physics, 2 edition, 2006b.

Spalart, P. R., 'Direct simulation of a turbulent boundary layer up to $re_\theta = 1410$,' Journal of Fluid Mechanics, 1988, **187**, pp. 61–98.

Stainback, P. C., 'Hypersonic boundary-layer transition in the presence of wind tunnel noise,' AIAA Journal, 1971, **9**(12), pp. 2475–2476.

Steen, L. E., *Characterization and Development of Nozzles for a Hypersonic Quiet Wind Tunnel*, Master's thesis, Purdue University, West Lafayette, IN, USA, 2010.

Stegen, G. R. and Van Atta, C. W., 'A technique for phase speed measurements in turbulent flows,' J. Fluid Mech., 1970, **42**, pp. 689–699.

Taylor, E. M., Wu, M., and Martín, M. P., 'Optimization of nonlinear error sources for weighted non-oscillatory methods in direct numerical simulations of compressible turbulence,' Journal of Computational Physics, 2006, **223**(1), pp. 384–397.

Thompson, K. W., 'Time dependent boundary conditions for hyperbolic systems,' Journal of Computational Physics, 1987, **68**(1), pp. 1–24.

Tichenor, N. R., Humble, R. A., and Bowersox, R. D. W., 'Response of a hypersonic turbulent boundary layer to favourable pressure gradients,' Journal of Fluid Mechanics, 2013, **722**, pp. 187–213, doi:10.1017/jfm.2013.89.

Tomkins, C. D. and Adrian, R. J., 'Spanwise structure and scale growth in turbulent boundary layers,' Journal of Fluid Mechanics, 2003, **490**, pp. 37–74.

Trettel, A. and Larsson, J., 'Mean velocity scaling for compressible wall turbulence with heat transfer,' Phys. Fluids, 2016, **28**(2), p. 026102.

Tsuji, Y., Fransson, J. H. M., Alferdsson, P. H., and Johansson, A. V., 'Pressure statistics and their scaling in high-reynolds-number turbulent boundary layers,' Journal of Fluid Mechanics, 2007, **585**, pp. 1–40.

Tsuji, Y., Imayama, S., Schlatter, P., Alfredsson, P. H., Johansson, A. V., Marusic, I., Hutchins, N., and Monty, J., 'Pressure fluctuation in high-reynolds-number turbulent boundary layer: Results from experiments and dns,' Journal of Turbulence, 2012, **13**(50), pp. 1–19.

van Driest, E. R., 'The problem of aerodynamic heating,' Aeronautical Engineering Review, 1956, **15**(10), pp. 26–41.

Walz, A., *Boundary Layers of Flow and Temperature*, MIT Press, 1969.

Welch, P. D., 'The use of fast fourier transform for the estimation of power spectra: A method based on time averaging over short, modified periodograms,' IEEE Trans. Audio Electroacoustics, 1967, **AU-15**, pp. 70–73.

Williams, O. J. H., Sahoo, D., Baumgartner, M. L., and Smits, A. J., 'Experiments on the structure and scaling of hypersonic turbulent boundary layers,' Journal of Fluid Mechanics, 2018, **834**, pp. 237–270, doi:10.1017/jfm.2017.712.

Williamson, J., 'Low-storage runge-kutta schemes,' Journal of Computational Physics, 1980, **35**(1), pp. 48–56.

Willmarth, W. W., 'Wall pressure fluctuations beneath turbulent boundary layers,' Annual Review of Fluid Mechanics, 1975, **7**, pp. 13–36.

Wu, B., Bi, W., Hussain, F., and She, Z. S., 'On the invariant mean velocity profile for compressible turbulent boundary layers,' J. Turbul., 2016a, pp. 1–17.

Wu, B., Bi, W., Hussain, F., and She, Z.-S., 'On the invariant mean velocity profile for compressible turbulent boundary layers,' Journal of Turbulence, 2016b, pp. 1–17, doi:10.1080/14685248.2016.1269911.

Wu, M. and Martín, M. P., 'Direct numerical simulation of supersonic boundary layer over a compression ramp,' AIAA Journal, 2007, **45**(4), pp. 879–889.

Wu, M. and Martín, M. P., 'Analysis of shock motion in shockwave and turbulent boundary layer interaction using direct numerical simulation data,' Journal of Fluid Mechanics, 2008, **594**, pp. 71–83.

Xu, S. and Martín, M. P., 'Assessment of inflow boundary conditions for compressible turbulent boundary layers,' Physics of Fluids, 2004, **16**(7), pp. 2623–2639.

Zeman, O., 'A new model for supersonic/hypersonic turbulent boundary layers,' 31st Aerospace Sciences Meeting, AIAA Paper 1993-0897, Jan. 1993, doi:10.2514/6.1993-897.

Zhang, C., Choudhari, M. M., and Duan, L., 'Acoustic radiation from high-speed turbulent boundary layers in a tunnel-like environment,' in '53rd AIAA Aerospace Sciences Meeting,' 2015 p. 0836, doi:10.2514/6.2015-0836.

Zhang, C. and Duan, L., 'Multivariate statistics analysis of the pressure field induced by high-speed turbulent boundary layers,' in '46th AIAA Fluid Dynamics Conference,' 2016 p. 3190, doi:10.2514/6.2016-3190.

Zhang, C., Duan, L., and Choudhari, M. M., 'Effect of wall cooling on boundary layer induced pressure fluctuations at mach 6,' Journal of Fluid Mechanics, 2017, **822**, pp. 5–30, doi:10.1017/jfm.2017.212.

Zhang, C., Duan, L., and Choudhari, M. M., 'Direct numerical simulation database for supersonic and hypersonic turbulent boundary layers,' AIAA Journal, 2018, **56**(11), pp. 4297–4311, doi:10.2514/1.J057296.

Zhang, C., Duan, L., and Choudhari, M. M., 'Acoustic radiation from a Mach 14 turbulent boundary layers,' 54th AIAA Aerospace Sciences Meeting, AIAA Paper 2016-0048, Jan. 2016, doi:10.2514/6.2016-0048.

Zhang, Y., Bi, W., Hussain, F., and She, Z., 'A generalized Reynolds analogy for compressible wall-bounded turbulent flows,' J. Fluid Mech., 2014, **739**, pp. 392–420.

VITA

Chao Zhang was born in Xiuwu conty, Jiaozuo City, Henan province, China. He received his Bachelor of Science degree in Mechanical Engineering in June 2008 from Nanjing University of Aeronautics and Astronautics, Nanjing City, Jiangsu province, China. In December 2018, he received his Doctor of Philosophy in Aerospace Engineering from Missouri University of Science and Technology, Rolla, Missouri, USA. His research interests included Computational fluid dynamics, Turbulent flow simulation and modeling, High-performance computing, Flow-generated sound, Combustion, Shock/Acoustic interaction, Numerical methods, Scalable CFD solver development